Toward Efficient and Stable Quantum Dot Solar Cells: Design and Characterization

by

Chia-Hao Marcus Chuang

B.S. Materials Science and Engineering, National Taiwan University (2007)
M.S. Materials Science and Engineering, National Taiwan University (2009)

Submitted to the Department of Materials Science and Engineering
in partial fulfillment of the requirements for the degree of

Doctor of Philosophy

at the

MASSACHUSETTS INSTITUTE OF TECHNOLOGY

June 2016

Author:.....
Department of Materials Science and Engineering
April 14, 2016

Certified by: .....
Moungi G. Bawendi
Lester Wolfe Professor of Chemistry
Thesis Supervisor

Certified by: .....
Jeffrey C. Grossman
Professor of Materials Science and Engineering
Thesis Reader

Accepted by:.....
Donald R. Sadoway
Chair, Departmental Committee on Graduate Studies

Toward Efficient and Stable Quantum Dot Solar Cells: Design and Characterization

by

Chia-Hao Marcus Chuang

Submitted to the Department of Materials Science and Engineering
on April 14, 2016, in partial fulfillment of the
requirements for the degree of
Doctor of Philosophy

Abstract

This thesis focuses on the optical and electronic properties of lead sulfide (PbS) quantum dots (QDs) for the development of QD solar cells. Near-infrared active PbS QDs composed of earth-abundant elements have emerged as promising candidates for photovoltaic applications because of the solution-processability and a tunable energy bandgap that covers the optimal bandgap range for single and multi-junction solar cells. However, despite rapid progress, previous QD solar cells still show unsatisfactory efficiency and stability. In this thesis work, room-temperature solution-processed ZnO/PbS solar cells with high efficiencies and unprecedented air-stability have been successfully demonstrated. The major limiting factors in present QD solar cells and potential routes to further improving the device performance have also been elucidated.

Owing to the versatile surface chemistry and high surface-to-volume ratio of QDs, the surface ligands play crucial roles in determining the optoelectronic properties. In this work, taking advantage of tunable electronic energy levels in QDs with different ligands, a new device architecture for solar cells has been designed. The architecture employs layers of QDs serving complementary functions, one as the main light absorbing layer and another as an electron-blocking/hole extraction layer. The device shows improved performance as a result of the relative band alignment between these QD layers, as confirmed by ultraviolet photoelectron spectroscopy. A device with this architecture reached a certified efficiency of 8.55 %, breaking previous record efficiencies of QD solar cells.

The device stability has been significantly improved in this work by identifying two key factors that limit the device stability. One key factor is the choice of ligands. It was found that iodide-passivated QDs are stable in air, while organic ligand passivated QDs are prone to oxidation. Another important factor is the removal of the commonly used MoO_3 interfacial layer, which gradually develops an unfavorable band alignment in the device with air exposure time. Understanding these degradation mechanisms leads to a successful demonstration of air-stable QD solar cells. The devices not only show high efficiency but also exhibit excellent long-term stability in air for more than 150 days without any encapsulation.

The origins of the large open-circuit voltage (V_{OC}) deficit, a primary limiting factor in present QD solar cells, have also been investigated through a combination of device physics and spectroscopic studies. Radiative sub-bandgap states with emission peak ~0.23 eV lower than the band-edge emission are found in QD solar cells. This energy difference is consistent with the below-bandgap activation energy for diode current generation obtained from current-voltage characteristics at different temperatures. It is concluded that the V_{OC} of present QD solar cells is mainly limited by the sub-bandgap states rather than the interfaces between QDs and other materials. The origin of sub-bandgap states was further found to be most likely from undercharged Pb atoms on the QD surface (off-stoichiometry).

Lastly, based on the findings in this thesis work, possible future directions that could further improve the efficiency of QD solar cells are discussed.

Thesis Supervisor: Moungi G. Bawendi
Title: Lester Wolfe Professor of Chemistry

Acknowledgements

This thesis was made possible with a tremendous amount of help from many people—either intellectually or mentally. Going to graduate school in a foreign city with different cultures and climates from where I grew up is a great life experience (I still remember how excited I was when I saw snow for the first time in my life in Boston!), and it wouldn't have been so great without my colleagues, collaborators, and friends. I would like to express my appreciation to all of you.

First, I would like to thank my advisor Moungi Bawendi. His commitment to scientific rigor has shaped the way we (at least I) view science. I have learned a lot not only from his guidance on research projects but also from his critical thinking and perspectives on science and technology. Moungi is an intelligent and kind advisor, a role model scientist. He provides an incredible environment with many talented people, abundant resources, and freedom for doing research. It was my privilege to have Moungi as my advisor and I couldn't have asked for more.

I would also like to thank all the members in the Bawendi Lab (and thank Moungi again for bringing these "Bawendians" together). David Strasfeld was my mentor when I joined this group. He taught me many characterization tools and how to prepare QD samples for various studies. The discussions with the device subgroup, Liang-Yi Chang, Darcy Grinolds, Whitney Hess, Gyuweon Hwang, Dong-Kyun Ko, and Jennifer Scherer, and other subgroups, Jessica Carr, Justin Caram, Ou Chen, Jose Cordero, Igor Coropceanu, Daniel Franke, Daniel Montana, Lea Nienhaus, and Mark Wilson are always helpful. We work on our own projects in a collaborative way and share our knowledge and results with others. Liang-Yi taught me most of the device fabrication and characterization methods. He was also the one I could always turn to for advice and chatting. Jenn makes working in LLB pleasurable because of the songs she played (and thank you for sharing music and playlists with me!) and the silly faces we made to each other. Darcy always kindly answered my questions and she passed on the "PbS scale-up party" organizer job to me so I learned more about the synthesis. Gyuweon showed me electrical characterization techniques that contributed significantly to this thesis work. Igor, Whitney, and I joined the Bawendi group together. They pretty much read every manuscript and proposal I wrote (including this thesis) and gave me helpful feedback. The interactions and conversation with them are truly enjoyable—be it about science or not.

Much of this thesis work is in collaboration with or inspired by other researchers at MIT. The QDPV-team meeting, which includes members from Vladimir Bulović group, Jeffrey Grossman group, and the Bawendi group, is a great platform for discussing science and initiating collaborations with people in different fields. In particular, I am grateful to have worked with Patrick Brown (UPS), Joel Jean (ellipsometry), Donghun Kim (DFT), and Andrea Maurano (carrier recombination) on many experiments through different approaches. I would like to thank my collaborators Sehoon Chang, Jayce Cheng, and Paul Rekemeyer from Silvija Gradečak group for providing nanowire samples and taking electron microscopy images. Jayce also carefully read my thesis and gave me valuable feedback. Mark Weidman is a fun guy who is also good at synthesizing high-quality PbS QDs. I have been using the awesome spectra of his QDs for most of my presentations. It was my pleasure to work with Riley Brandt. He kindly helped me with testing the device that later became a record-breaking solar cell. The fruitful discussions and experiments done with Riley was the precursor and a core part of the V_{OC} deficit project. Tzhow Huang and Chern Chuang helped me with writing some MATLAB codes that made data processing (and my life) easier. This also inspired me to explore more and led to my Python projects for data analysis and optical modeling. Chun-Teh Chen is an excellent photographer and he took the wonderful picture of my solar cell featured on the MIT homepage and several news outlets.

Chun-Wei Chen was my research advisor during my studies at NTU. His classes introduced me to the fields of the optical and electronic properties of materials. He also encouraged me to apply for graduate school. Without his guidance and the experience gained in his research group, I wouldn't have been admitted to MIT.

I wouldn't have survived graduate school without my friends outside of the lab. Those good times I had with all my friends are invaluable. I thank Chern Chuang for the late night beers, impromptu biking trips, and conversations on various topics ranging from science to social justice. Yu-Ting Lin, Pan-Yu Chen and Felix Ye are great friends, my best dinner buddies, and the ones I can always turn to for anything. I thank Sasha Huang for providing me information about many things, and for always listening to whatever random stuff I say. Jo Lu significantly enriched my graduate school life—we went to many concerts and music festivals and did the amazing road trip from Boston to LA together. Those board game nights with Steven Chang, Tony Wu, Kevin Chen, Shu-Heng Shao,

and Yu Wang were really fun. I'm thankful to Sam Peng and Syuan-Ming Guo who helped me with everything when I arrived in Boston, from getting furniture to advice on finding a research group. The times hanging out with Bryan Beaudoin, Madoka Morr, Audrey Battista, Rebecca Gross, and Renana Farbstein has made the last year of my graduate school life more colorful.

I have special thanks to many awesome bands that made great music—The National, Beach House, The Antlers, Arcade Fire, Blur, Arctic Monkeys, Explosion in the Sky, Sigur Ros and Travis... (the list could go on and on!). There are a lot of ups and downs in life (especially while getting a PhD in a foreign country). In addition to the friends I mentioned above, it is music that not only brought me joy, comfort, and peace, but also helped me make it through rough times. I'm also glad that I saw many of my favorite bands perform live during graduate school with my concert buddies: Jo Lu, Yu-Ting Ln, Rachel Wu, TC Chen, Yu Wang, Raphaël Schroeter, and Yorgos Efthymiadis, all of who also introduced me to some good music.

Lastly, I would like to thank my family for their support.

Contents

Figures

Tables

CHAPTER 1
Introduction

1.1 Quantum Confinement in Nanomaterials

Nanomaterials are materials which have at least one dimension in the nanometer range, typically between 1-100 nm. These materials often exhibit vastly different properties from their bulk counterparts and have attracted a great variety of research interests. For example, if any dimension of a nanomaterial is comparable to or smaller than the Bohr radius of an exciton a_B, which is the natural length scale of an exciton in a bulk semiconductor, then the electronic levels and optical properties show size dependence. This phenomenon is known as the quantum confinement effect.

$$a_B = \varepsilon_r \left(\frac{m_e}{\mu^*}\right) a_0 \tag{1-1}$$

where ε_r is the dielectric constant, m_e is the mass of a free electron, μ^* is the effective reduced mass of an exciton, and $a_0 = 0.053$ nm is the Bohr radius of hydrogen atoms (an exciton is an electron-hole pair bound by Coulomb force, which can be approximated by the *hydrogen atom model*).

The quantum confinement effect originates from the size-dependent electronic structure of materials. In bulk semiconductor crystals, the electrons and holes can move in 3 dimensions and have 3 degrees of freedom. The electronic structures can be solved by treating the semiconductor as an infinite crystal with a periodic lattice

potential. For a small crystal, the boundary conditions for solving the Schrödinger equations have to be modified since the electron and hole wavefunctions are "confined" by the physical size of the crystal, which deviates from the infinite crystal assumption. It can be shown that, using the simplified *particle in a box* model, the ground state energy in a small crystal is higher than that in the bulk. This energy difference is called the confinement energy $E_{confinement}$ and is inversely proportional to the square of the size L:

$$E_{confinement} = \frac{\hbar^2 \pi^2}{2\mu^* L^2} \tag{1-2}$$

In addition, the density of states (DOS) in quantum confined systems takes different functional forms depending on the number of confined dimensions (Figure 1.1). The DOS in bulk materials is proportional to $E^{1/2}$. In 2-D *quantum well* structures, electrons and holes have two degrees of freedom (1-D confinement) and the DOS is independent of energy. Materials with 2-D confinement are called *quantum wires* and their DOS is proportional to $E^{-1/2}$, whereas materials with 3-D confinement are called *quantum dots* whose DOS are delta functions. In reality, the DOS of quantum confined materials are further modified by the homogeneity, lattice potential, and the shape of the nanocrystal.

Overall, the observed bandgap or the band-edge absorption energy in a quantum confined system can be described by Equation (1-3):

$$E_{band\ edge} \approx E_{g,bulk} + \frac{\hbar^2 \pi^2}{2\mu^* L^2} - E_X \tag{1-3}$$

where $E_{g,bulk}$ is bandgap energy of the bulk material, and E_X is the exciton binding energy (E_X is also a function of the size and the size-dependent dielectric constant). In order for a material to show significant quantum confinement effect, the size has to be comparable to the exciton Bohr radius, which depends on material-specific properties as indicated by Equation (1-1) and is on the order of 10 nm. For example, the exciton Bohr radii are approximately 1 nm for CuCl, 6 nm for CdSe,

20 nm for PbS, and 54 nm for InSb [1]. Within this quantum confinement regime, the observed bandgap of a semiconductor increases with decreasing size. It is also clear that not all nanomaterials are quantum confined materials. For example, a 10 nm (in diameter) PbS crystal is considered a quantum dot, while a 10 nm CuCl crystal is not (and it should be termed as a nanocrystal or nanoparticle).

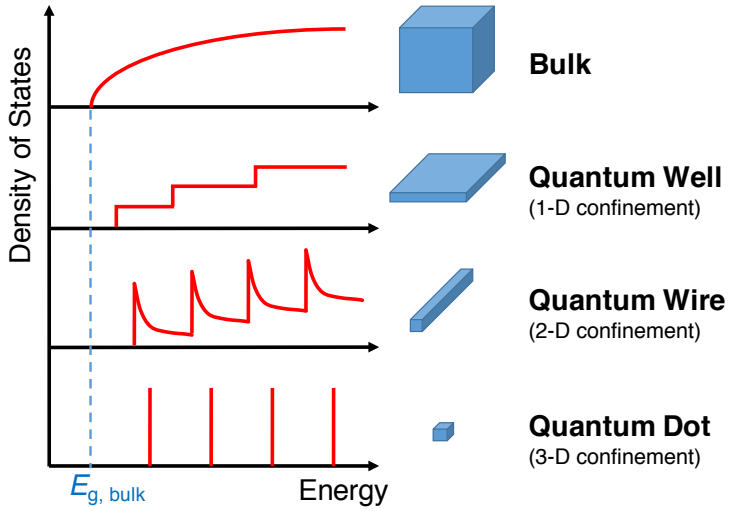

Figure 1.1 Schematic of the density of states in the bulk and ideal quantum confined systems predicted by the simplified particle in a box model.

1.2 Colloidal Quantum Dots

1.2.1 Basics of Quantum Dots

Colloidal quantum dots (QDs) are chemically synthesized semiconductor nanocrystals whose sizes are within the quantum confinement regime. The surface of as-synthesized QDs are capped with organic molecules, known as *ligands* (Figure 1.2). These ligands not only play an important role during the growth of QDs but also provide colloidal stability of the QDs. Typical ligands for the synthesis of QDs include oleic acid (OA), oleylamine, and trioctylphosphine oxide, all of which contain a functional group that binds to the surface of QDs and a long aliphatic chain. Therefore, QDs can be easily dispersed in common organic solvents such as

hexane, chloroform, and toluene. The ligands on the as-synthesized QDs can also be replaced with other molecules through *ligand exchange* to tailor their properties for different applications or make them water soluble.

Most QDs consist of binary compounds such as II-VI materials (CdS, CdSe, CdTe), III-V materials (InAs, InP), and IV-VI materials (PbS, PbSe, PbTe). In some cases, an inorganic shell is added to the QDs to either modify the electronic structures or protect the core from the environment. This structure is called core-shell QDs. Typical examples include the CdSe/CdS and CdSe/ZnS core/shell QDs.

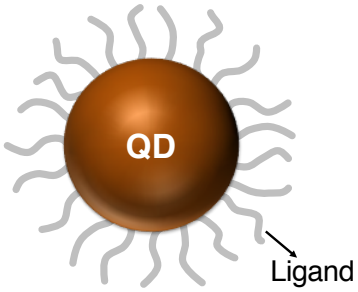

Figure 1.2 Schematic of an inorganic colloidal quantum dot and the organic ligands on the surface.

1.2.2 Optical Properties of QDs

Figure 1.3 shows the absorption and photoluminescence (PL) spectra of QDs with different sizes [2, 3]. The absorption spectra clearly show the size dependence of the bandgap, or band-edge energy, in CdSe QDs as a result of the quantum confinement effect (Figure 1.3a). As the bandgap of the QDs is sensitive to the physical size, a high polydispersity (size inhomogeneity) of QDs broadens the spectral linewidths of the absorption and emission spectra. To date, researchers are able to synthesize certain QDs with a polydispersity as low as 4–5 % (standard deviation of the diameter), PL linewidths of an ensemble QD sample approaching the linewidth of a single QD (50–70 meV; Figure 1.3b) , and PL quantum yields approaching unity [3, 4]. These interesting optical properties and the tunability demonstrate the potential of QDs in many optical and optoelectronic applications.

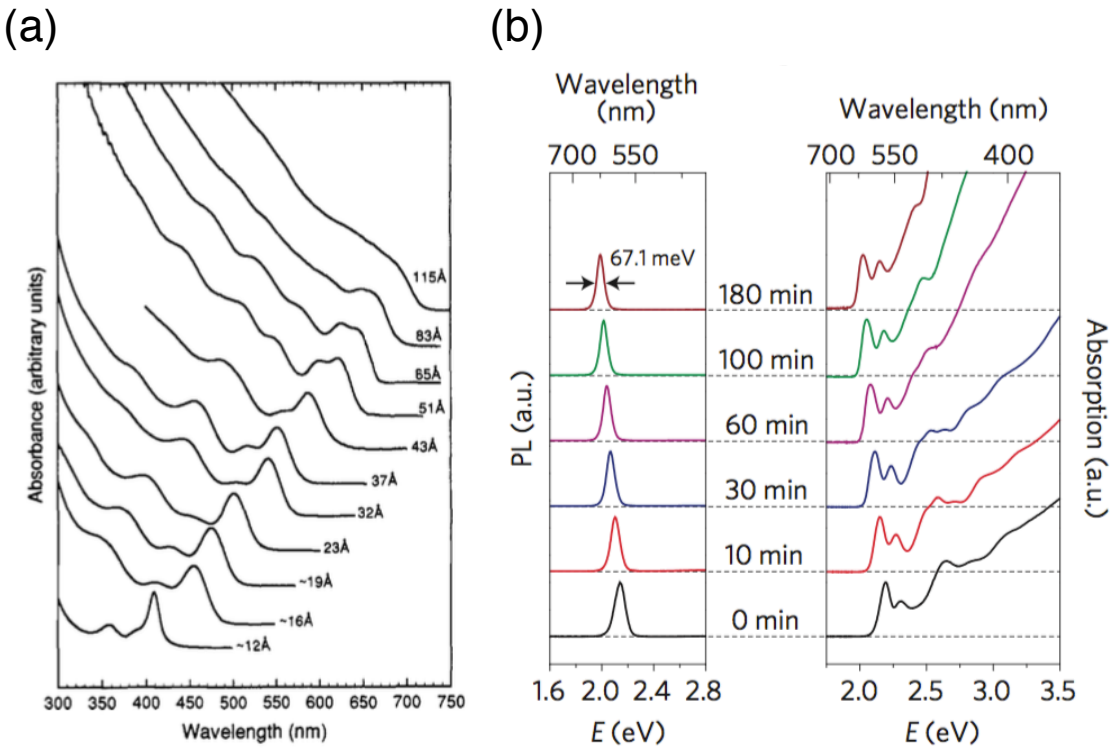

Figure 1.3 Absorption and PL spectra of QDs with different sizes. (a) Absorption spectra of CdSe QDs; (b) PL (left) and absorption (right) spectra of CdSe-CdS core-shell QDs.
(a) Reprinted with permission from Ref. [2]. Copyright (1993) American Chemical Society; (b) Adapted with permission from Ref. [3]. Copyright (2013) Macmillan Publishers Ltd.

1.2.3 Applications of QDs

The unique optical properties and the solution processability of QDs make them ideal for a variety of applications. The color tunability, narrow emission linewidths, and high emission quantum yields are particularly attractive for light-emitting technologies, such as laser [5, 6] and light-emitting diodes (LEDs) [7–10]. In addition, QDs show a broad absorption range and high absorption coefficients. Applications such as photon down conversion, in which the QDs absorb a short-wavelength (high energy) photon and emit a photon at a desired, longer wavelength, are very appealing. This concept has been widely used in display

technologies. Recently, QDs have been incorporated into commercial displays (quantum dot TVs) to replace the traditional organic phosphors [11]. The quantum dot TVs, owning to the high purity of the color (narrow emission linewidths), offer higher color saturation and could be more energy-efficient. The down conversion technique can also be used to achieve dual-band photodetection by converting ultraviolet and visible photons into near-infrared (NIR) photons for detection by a NIR camera [12].

In addition to light-emitting technologies, QDs have been applied to bio-imaging and other optoelectronic devices. The ligands on the surface of QDs can be functionalized for biological targets such as proteins and antibodies, enabling cell-labeling and *in vivo* imaging [13]. Taking advantage of the distinct, sharp, and tunable absorption features, a QD spectrometer has also been realized [14]. Other applications include solution-processed thin-film transistors [15–21] and photodetectors [22–24]. This thesis will focus on the photovoltaic applications *i.e*, QD solar cells, which can convert incident light into electricity. The physics of solar cells is provided in the next section. The basic working principles and progress of QD solar cells will be discussed in Chapter 2.

1.3 Solar Cells

1.3.1 Basic Principles of Solar Cells

A solar cell is a semiconductor optoelectronic device that can absorb light and convert the energy of the light into electricity. When a semiconductor absorbs photons with energy greater than the bandgap, electrons in the valence band (VB) are excited into the conduction band (CB), leaving holes in the VB. If a solar cell is not connected to an external circuit, these excess electrons and holes redistribute and accumulate at the opposite sides of the device, creating a voltage difference between the two electrodes. If the electrodes are connected *via* an external circuit, this voltage difference drives current flow. This effect is called the *photovoltaic*

effect. Therefore, solar cells are also known as photovoltaic (PV) cells, solar photovoltaics, or simply photovoltaics.

The working principles of solar cells can be understood by the device physics of *p*–*n* homojunction diodes, the most studied and well-established solar cells. A *p*–*n* junction is a semiconductor junction between a *p*-doped semiconductor (whose majority carriers are holes) and an *n*-doped semiconductor (whose majority carriers are electrons). A homojunction is a semiconductor junction in which the materials on the two sides of the junction are the same (same bandgap, electron affinity, and ionization potential) but with different doping levels, whereas a heterojunction is formed by two different materials.

Figure 1.4 shows a *p*–*n* homojunction diode and its equilibrium band energy diagram in the dark. When the *p*-type and *n*-type semiconductors are in contact, electrons diffuse from the *n*-type material to the *p*-type material, resulting in a positively charged region on the *n*-side. Similarly, a negatively charged region forms on the *p*-side due to the diffusion of holes. The charged region is called the *depletion region* or *space charge region*, whereas the region outside of the depletion region is called the *quasi-neutral region*. The depletion region creates a built-in electric field and thus a built-in potential qV_{bi} across the junction, which prevents further diffusion. It is this built-in field that enables the rectifying characteristics of the device. Under forward bias (applied voltage $V > 0$), the number of carriers that can overcome the energy barrier $q(V_{bi} - V)$ increases exponentially with V (diffusion current). Under reverse bias ($V < 0$), the current flow is dominated by the drift current, which depends on the amount of minority carriers drifting due to the built-in field to another side of the junction, and is thus very small. The overall current–voltage characteristics of a diode can be described by the Shockley ideal diode equation [25, 26]

$$J = J_0 \left[\exp\left(\frac{qV}{nkT}\right) - 1 \right] \tag{1-4}$$

where J is the current density, J_0 is the reverse saturation current density, n is the diode ideality factor, k is the Boltzmann constant, and T is the temperature.

When a solar cell is under illumination, an equal amount of electrons and holes are formed in the semiconductor as a result of photoexcitation. The built-in potential can drive the photogenerated electrons on the *p*-side to the *n*-side, and the photogenerated holes on the *n*-side to the *p*-side (see section 1.3.3). The flow of these excess carriers produce photocurrent J_{ph} in an opposite direction to the diode current. Therefore, the current-voltage characteristics can be expressed as

$$J = -J_{ph} + J_0 \left[\exp\left(\frac{qV}{nkT}\right) - 1 \right] \tag{1-5}$$

While Equation (1-4) and (1-5) are derived from *p*–*n* homojunction solar cells, they are the general forms for most types of solar cells. The current-voltage characteristics for heterojunction solar cells [27] and Schottky junction solar cells [25, 26] both follow these forms, although the mechanisms contributing to the J_0 and thus the functional forms of the J_0 are different from *p*–*n* homojunction diodes.

More generally, by considering the series resistance (R_s, in series with the diode) and the shunt resistance (R_p, in parallel to the diode, a leakage path), a realistic solar cell with a device area A can be modeled using the equivalent circuit model

$$J = -J_{ph} + J_0 \left\{ \exp\left[\frac{q(V + Jr_s)}{nkT}\right] - 1 \right\} + \frac{V + Jr_s}{r_p} \tag{1-6}$$

where r_s=AR_s and r_p=AR_p are the specific series resistance and specific shunt resistance, respectively.

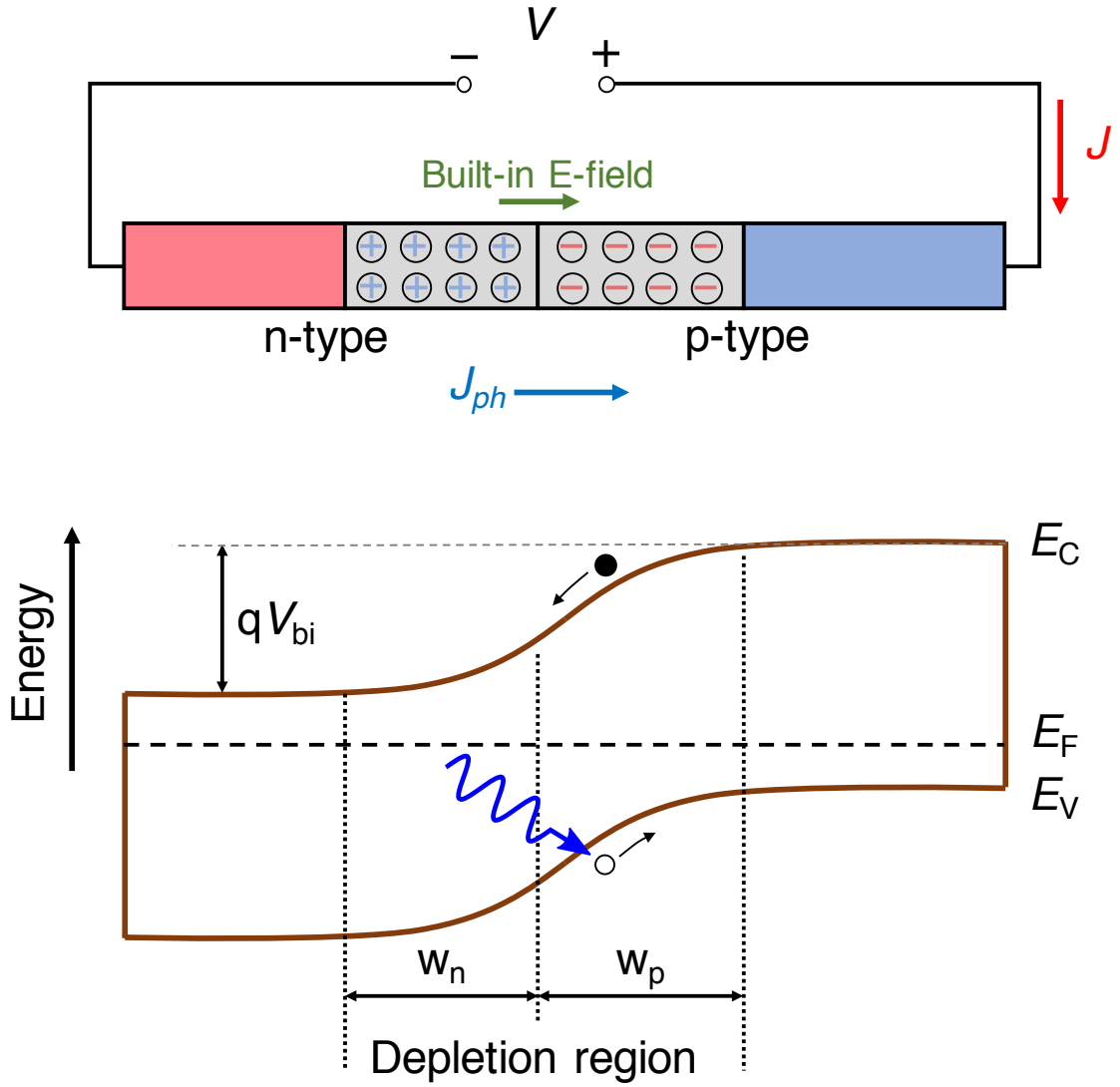

Figure 1.4 A p–n homojunction solar cell and the corresponding band energy diagram.
E_C: conduction band minimum; E_V: valance band maximum; E_F: Fermi level; V_{bi}: buil-in potential; w_p and w_n: depletion width on the p-side and n-side, respectively.

1.3.2 Characteristics of Solar Cells

A typical J–V curve of a solar cell under illumination is shown in Figure 1.5. As described above, the direction of the photocurrent is in the opposite direction of the applied voltage (Equation (1-5)). Therefore, part of the J–V curve falls into

the fourth quadrant. In this region, a positive applied voltage input results in a negative current output or a "negative power consumption", which demonstrates the power generating effect in solar cells. In some reports, the sign of the current is manually inverted to represent the power generating region in the first quadrant. However, in real measurements, this region is always in the fourth quadrant.

Three important solar cell parameters can be deduced from a *J*–*V* curve: the short-circuit current density (J_{SC}), the open-circuit voltage (V_{OC}), and the fill factor (*FF*). The J_{SC} is the output photocurrent when no bias is applied (note: J_{SC} is non-negative). The V_{OC} is the voltage at which the current is zero. These two parameters represent the limiting cases of current and voltage output when an external load is connected to the solar cell, respectively. The *FF* is related to the extraction loss and is defined as the ratio of the maximum output power to the product of J_{SC} and V_{OC}, which is the ratio of the area of the two shaded region in Figure 1.5.

$$FF = \frac{|J\ V|_{max}}{J_{SC}V_{OC}} \tag{1-7}$$

The power conversion efficiency (*PCE*) of a solar cell is the maximum power output divided by the power of the incident light

$$PCE = \frac{P_{out}}{P_{in}} = \frac{|J\ V|_{max}}{P_{in}} = \frac{J_{SC}V_{OC}FF}{P_{in}} \tag{1-8}$$

For standard solar cell testing, the air mass 1.5 (AM 1.5) solar spectrum with an incident power density of 100 mW/cm^2 is used. This power density is also called 1-sun.

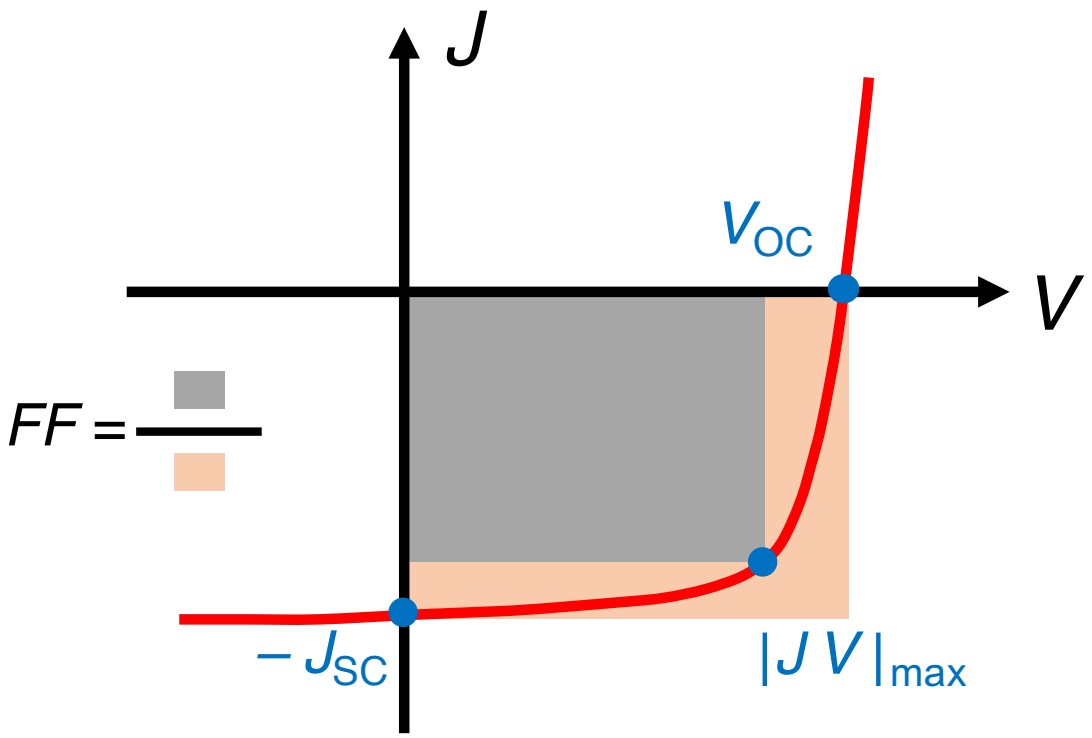

Figure 1.5 Current-voltage characteristics of a solar cell under illumination.

1.3.3 Carrier Collection

While the semiconductor layer in a solar cell can absorb photons to create charge carriers, in order to produce photocurrent, these photogenerated carriers need to be collected. The collection probability depends on the position where carriers are generated. Based on the dominant mechanism, we can discuss the collection probability of carriers generated in two different regions: (i) inside the depletion region (dominated by drift), and (ii) in the quasi-neutral region (dominated by diffusion).

If the carriers are generated inside the depletion region, the built-in field can sweep photogenerated electrons to the *n*-side and holes to the *p*-side efficiently. The collection probability for carriers generated in the depletion region is near

unity. Therefore, a wide depletion region is beneficial for carrier collection. For a *p*–*n* homojunction formed by a *p*-type semiconductor with a doping concentration N_a (hole concentration) and an *n*-type semiconductor with a doping concentration N_d (electron concentration) the depletion width on the *n*-side (w_n) and *p*-side (w_p) are given by Equation (1-9) and (1-10), respectively [25, 26]. The overall depletion width w is the sum of w_n and w_p (Equation (1-11)).

$$w_n = \left[\frac{2\varepsilon_r}{q} \frac{N_a}{N_d(N_a + N_d)} (V_{bi} - V) \right]^{1/2} \tag{1-9}$$

$$w_p = \left[\frac{2\varepsilon_r}{q} \frac{N_d}{N_a(N_a + N_d)} (V_{bi} - V) \right]^{1/2} \tag{1-10}$$

$$w = w_n + w_p = \left[\frac{2\varepsilon_r}{q} \frac{N_a + N_d}{N_a N_d} (V_{bi} - V) \right]^{1/2} \tag{1-11}$$

The charge neutrality condition sets the relation between the depletion widths on the two sides: $w_n N_d = w_p N_a$. It follows that the lower the doping concentration N_a on the *p*-side, the wider the depletion width w_p on the *p*-side, and *vice versa*.

For carriers generated in the quasi-neutral region, the collection probability depends on the distance to the edge of the depletion region and the minority carrier diffusion length L_D. Figure 1.6 shows the collection probability of photogenerated carriers on the *p*-side of the device as an example. On this side of device, electrons are the minority carriers and holes are the majority carriers. Although photoexcitation generates equal amounts of excess electrons and holes ($\delta n = \delta p$), the photogenerated hole concentration is usually smaller than or comparable to the hole concentration in the dark. Therefore, the overall collection probability is determined by the collection probability of the minority carriers, which in this case are electrons. Since there is no built-in field to drive the minority carriers in the quasi-neutral region, the movement of the photogenerated electrons is dominated by diffusion. If an electron diffuses to the edge of the depletion region, it can be swept into the *n*-side by the built-in field, making a collection event. Otherwise the

electron would recombine with a hole and lose the energy as heat or radiation. As a result, the excess minority carrier concentration δn near the edge of the depletion region is approaching zero but increases with the distance to the edge. This concentration gradient provides a driving force for diffusion. The collection probability for carriers generated in this region is thus the probability of the minority carrier successfully diffusing to the edge of the depletion region within its lifetime. It can be solved by the 1-D diffusion equation and the solution is approximately an exponential function.

$$P(x) \approx e^{-x/L_D} \tag{1-12}$$

$$L_D = \sqrt{D\tau} \tag{1-13}$$

where x is the distance to the edge of the depletion region ($x \geq 0$), D is the diffusion coefficient of the minority carrier, and τ is the minority carrier lifetime. A high collection probability requires a long minority carrier diffusion length and thus a high diffusion coefficient (which is proportional to the carrier mobility) and a long minority carrier lifetime.

The back surface of the device also affects the collection probability (Figure 1.7). If the recombination rate at the back surface is very high, which might be due to poor surface passivation, the collection probability at the back surface approaches zero (boundary condition for the diffusion equation: $\delta n(x,t)|_{x=d} = 0$ where d is the distance of the back surface to the edge of the depletion region). On the other hand, if the surface recombination rate is very low, the back surface would act as a perfect mirror which reflects back the minority carrier.

If a bias V is applied to the device, the effective built-in voltage becomes $V_{bi} - V$. Under reverse bias $V<0$, the depletion region widens, which improves the overall collection efficiency. However, under forward bias, the depletion region shrinks and the carrier collection efficiency decreases. This voltage dependence has a more significant effect on devices with a shorter diffusion length because the majority of the collected carriers are generated inside the depletion region. A

typical result of this field-dependent carrier collection is a smaller *FF*. For devices with very long carrier diffusion lengths, a reduction in the depletion width has negligible effect because carriers generated outside of the depletion region can still diffuse to the depletion region to be collected.

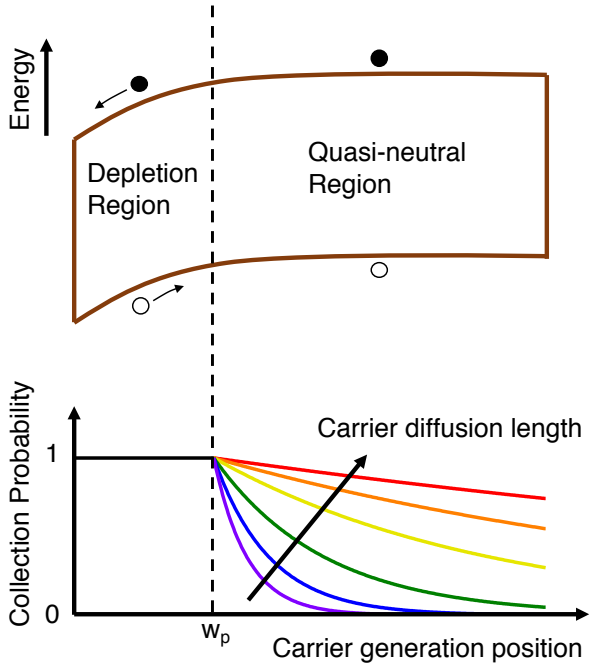

Figure 1.6 Collection probability of photogenerated minority carriers at different positions in the device.

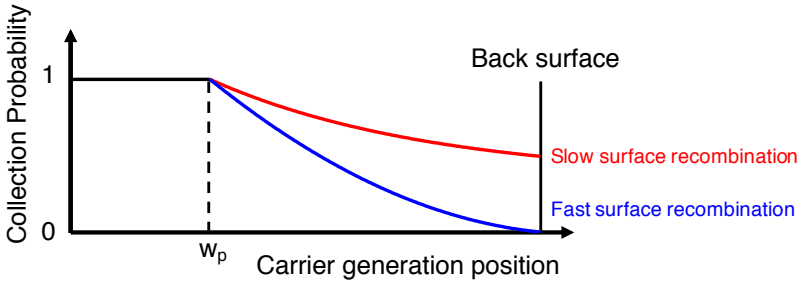

Figure 1.7 Collection probability of photogenerated minority carriers in devices with slow and fast surface recombination.

1.3.4 Efficiency Limit

Even a perfect solar cell cannot convert 100 % of the energy from sunlight into electricity. The theoretical maximum efficiencies of solar cells were first calculated by W. Shockley and H. Queisser in 1961, later known as the Shockley–Queisser limit [28]. The calculation assumes an ideal *p*–*n* junction solar cell that can absorb 100 % of the photons with energy above the bandgap and collect them as photocurrent; the incident solar spectrum is approximated by the black body radiation at 6000 K; the *J*–*V* characteristics are modeled using Equation (1-5), in which the dark saturation current J_0 is the radiative recombination of thermally generated electrons and holes (or, equivalently, the solar cell equilibrates with the environment and emits black body radiation at 300 K). Using the AM 1.5 solar spectrum (instead of the black body radiation at 6000 K) at 1-sun intensity, the maximum theoretical efficiency is found to be 33.7 % for a *p*–*n* junction solar cell with a bandgap of 1.337 eV (Figure 1.8).

For an "ideal" solar cell, one part of the energy loss is the transmission loss because a semiconductor cannot absorb photons with energy lower than its bandgap E_g. Another significant part of the energy loss is due to carrier thermalization (Figure 1.9a). When a semiconductor absorbs photons with energy E_{photon} higher than E_g, carriers are excited to higher energy states. These carriers rapidly relax to the band edge and release the excess energy as heat. While a solar cell made of a low bandgap material would have a lower transmission loss and thus a higher J_{SC} (Figure 1.9b), the thermalization loss would increase and the V_{OC} would reduce (Figure 1.9c). There is also extraction loss because the *FF* is below 1 and the V_{OC} is lower than E_g/q. Taking the bandgap dependence of these loss mechanisms into account, the theoretical maximum efficiency peaks at 33.7 % for solar cells made of a semiconductor with a bandgap of 1.337 eV. The breakdown of the energy loss for the solar cell with maximum efficiency is shown in Figure 1.10.

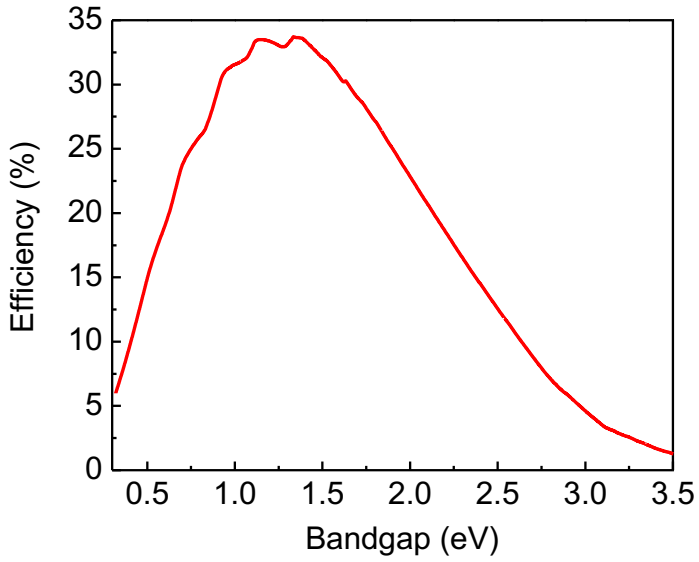

Figure 1.8 Theoretical maximum efficiencies for solar cells with different bandgaps under AM 1.5 1-sun illumination at 300 K.

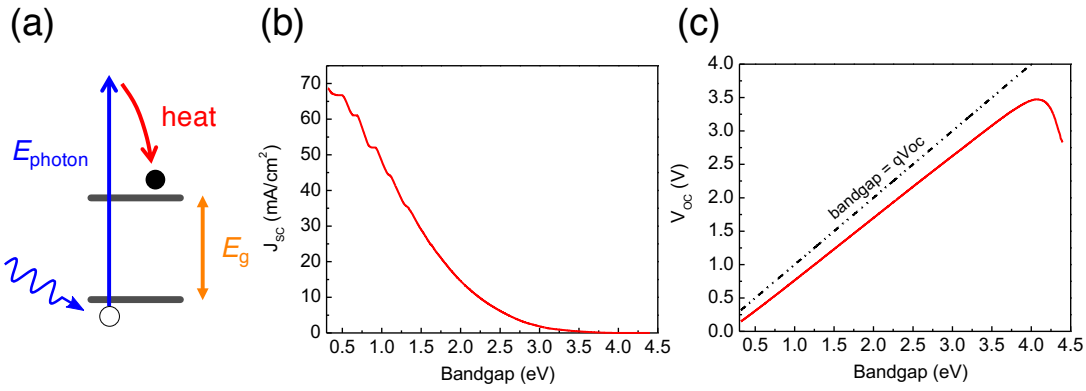

Figure 1.9 (a) Thermalization loss in solar cells. (b) Theoretical maximum J_{SC} and (c) theoretical maximum V_{OC} for solar cells with different bandgaps under AM 1.5 1-sun illumination at 300 K.

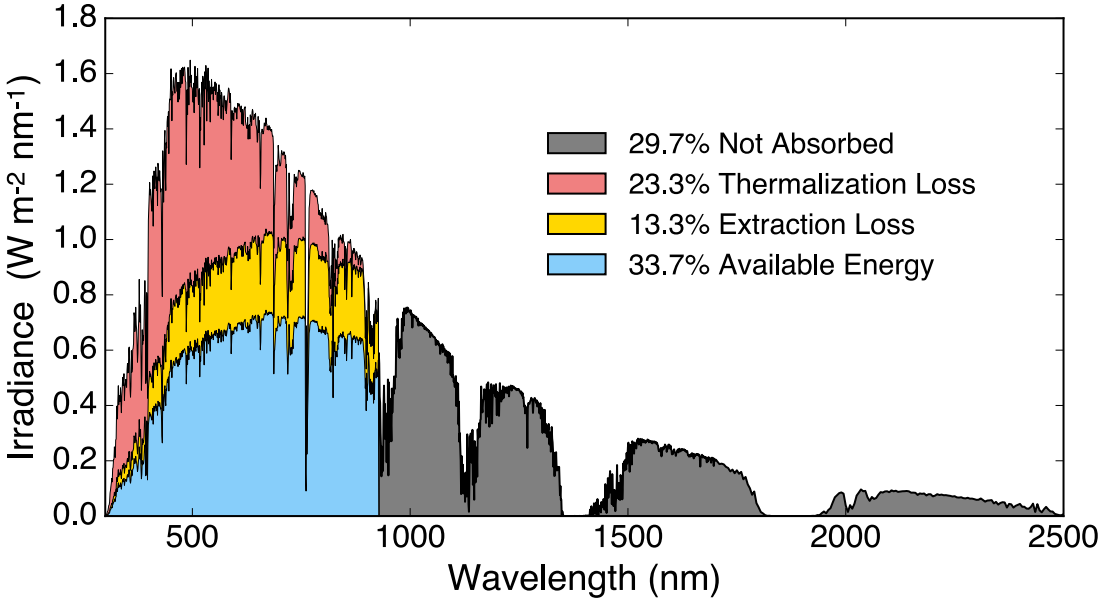

Figure 1.10 Breakdown of the energy loss and available energy for an ideal solar cell with a bandgap of 1.337 eV (absorption edge at 927 nm) under AM 1.5 1-sun illumination at 300 K.

It is possible for some solar cells to exceed the Shockley–Queisser limit through different approaches. In principle, a material that shows the multi-exciton generation or carrier multiplication effect, in which an incident photon can create more than one electron–hole pair, can raise the theoretical efficiency limit. Concentrator solar cells, which operate at higher illumination intensities, also show a higher efficiency limit. Another popular approach is the multi-junction or tandem solar cells, which consist of several sub-cells with different bandgaps to absorb different portion of sun light. For example, the theoretical limit of a triple-junction solar cell can be above 50 % (Figure 1.11). To date, concentrator solar cells and multi-junction solar cells with efficiencies higher than 33.7 % have been successfully demonstrated [29], yet the manufacturing processes are complicated, limiting practical applications.

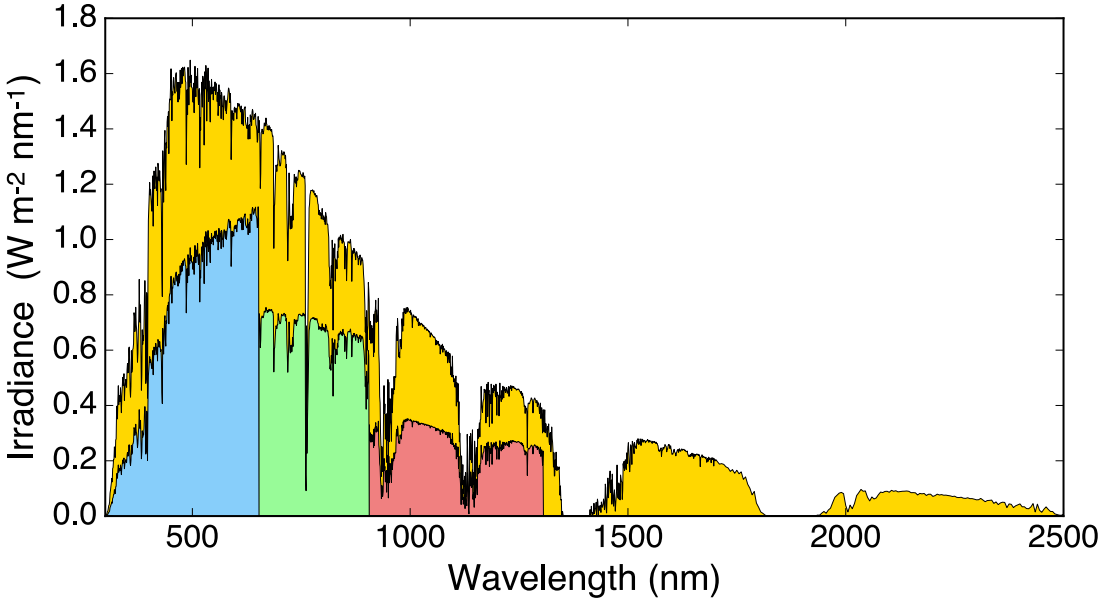

Figure 1.11 Theoretical available energy for a triple-junction solar cell consisting of subcells with bandgaps of 1.9 eV (light blue), 1.37 eV (light green), and 0.95 eV (light red) under AM 1.5 1-sun illumination at 300 K. The overall theoretical efficiency is 51.4 %.

1.4 Thesis Overview

This thesis focuses on the development of efficient air-stable QD solar cells based on PbS QDs from two approaches: design of novel device architectures and understanding of present limitations for future improvement.

Chapter 2 provides an overview of the field of QD solar cells. The progress, milestones, and challenges are briefly discussed. Chapter 3 describes a band alignment engineering strategy used in a new device architecture. The new architecture utilizes the tunable electronic energy levels in QDs to achieve improved photocurrent extraction, leading to QD solar cells with high efficiencies and unprecedented air stability.

Chapter 4 shows evidence for the presence of radiative sub-bandgap states and the filling of these states in working devices under different operating conditions. Chapter 5 presents various analyses that provide a deeper understanding of the working mechanisms of QD solar cells. Combining the results from Chapter 4, the present limitations in PbS QD solar cells, particularly the origins of the high V_{OC} deficit, are discussed. The possible future directions based on these results are suggested as well.

Appendix A demonstrates further improvement in photocurrent extraction by using ZnO nanowires. Appendix B and C show studies of band alignment engineering strategies and the operational stability of devices. Appendix D explores some post-deposition treatments for performance enhancement. Appendix E introduces an alternative source of ligand with similar effectiveness. Appendix F examines the feasibility of QD tandem cells with sub-cells adopting the architecture introduced in Chapter 3. Finally, the reports of the independently certified solar cell performance are included in Appendix G.

CHAPTER 2

Quantum Dot Solar Cells

2.1 Quantum Dots for Solution-Processed Photovoltaics

Solar energy is one of the most promising renewable energy sources that could lead to energy sustainability. An ideal solar cell should not only have a high power conversion efficiency but also have a low manufacturing cost and long-term stability to ensure short energy payback time. In addition, for a variety of applications ranging from portable solar cells, to consumer electronics with different form factors, to rooftop solar panels, flexible and lightweight devices are preferred.

Nowadays, the solar cell market is dominated by single-junction Si solar cells. Si solar cells are made of Earth-abundant materials and they show high efficiencies and good long-term stability. The manufacturing complexity is high due to the requirement of high-purity materials and high-temperature processing conditions. The manufacturing costs—owing to the increase in the scale of manufacturing—have significantly declined in recent years, making them more cost-effective for utility-scale deployment. However, the rigidity and bulkiness of Si solar panels limit the range of applications, and the high temperature processing is not compatible with flexible substrates. Solution-processed solar cells, on the other hand, have the potential to meet all of these criteria. For years, researchers have been actively working on solution-processed solar cells that aim for flexible and lightweight devices with low-cost and high specific power [30].

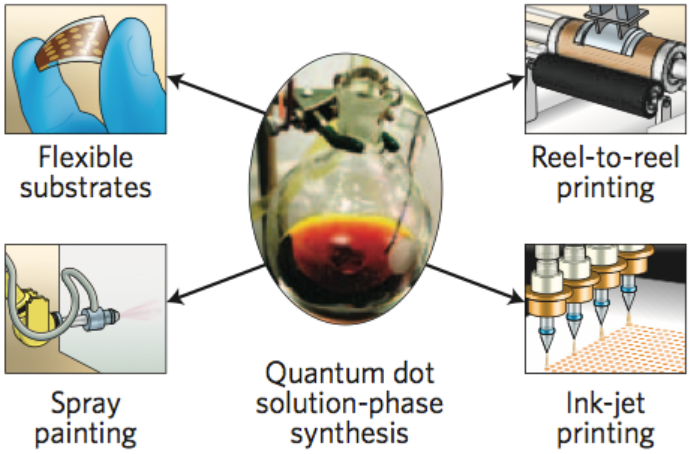

Figure 2.1 Techniques for low-temperature solution-processed QD solar cells. Adapted with permission from Ref [31]. Copyright (2012) Macmillan Publishers Ltd.

In the past decade, colloidal quantum dots (QDs), particularly lead sulfide (PbS) QDs, have emerged as a promising class of materials for solar energy harvesting [22, 29, 32–36]. Chemically synthesized QDs can be dispersed in solvents and then deposited onto a variety of substrates at low temperature (Figure 2.1). These cost-effective deposition techniques such as spin-coating, ink-jet printing, spray-coating, and roll-to-roll processing are compatible with large and flexible substrates. Advances in synthesis protocols have made it possible to perform large-scale synthesis (Figure 2.2a) as well as synthesize QDs with narrow size-distributions at desired bandgaps [2, 37, 38]. One can tune the bandgap of QDs by changing their size to absorb different part of the solar spectrum. As the optimal bandgap range for single junction solar cells is 1.1 – 1.5 eV (Figure 1.8), QDs made of materials with low bulk bandgaps, such as lead chalcogenides PbX (X=S, Se, Te), are among the top choices.

Bulk PbS has a direct bandgap of ~0.4 eV. Owing to the quantum confinement effect and the large Bohr radius, the bandgap of PbS QDs can be easily tuned from approximately 0.6 eV to 1.6 eV by changing the size (Figure

2.2b). This range covers the optimal bandgaps for single junction solar cells, enabling visible and near-infrared light harvesting. In addition to their low bandgap and broad bandgap tunability, PbS QDs are solution-processable and relatively stable. Furthermore, they are composed of inexpensive Earth-abundant elements [39, 40].

These properties are appealing not only for single junction but also for tandem (multi-junction) solar cells. Tandem solar cells require materials with different bandgaps. The choice of light-absorbing materials is thus crucial. Typical materials used for tandem solar cells are InGaP, GaAs, $In_xGa_{1-x}As$, and Ge. However, fabrication of devices consisting of these materials is a challenging task because the lattice constants have to be closely matched to grow one layer on top of another layer. These devices are usually fabricated with techniques such as molecular beam epitaxy (MBE) or metal organic chemical vapor deposition (MOCVD). The devices also require multiple interlayers to fine-tune the optoelectronic properties and lattice constants. As a result, although high efficiencies have been achieved, the fabrication is very expensive and is thus not cost competitive to single junction solar cells. The applications of these tandem cells are limited—they are primarily used in environments where power-to-weight ratio is more important than cost, such as aerospace. Solution-processed QDs, in principle, could achieve similar performance with a much lower cost because of simpler processing conditions. It is this unique combination of low bandgaps, bandgap tunability, material abundance, and solution-processability that makes PbS QDs ideal candidates for solar cell applications.

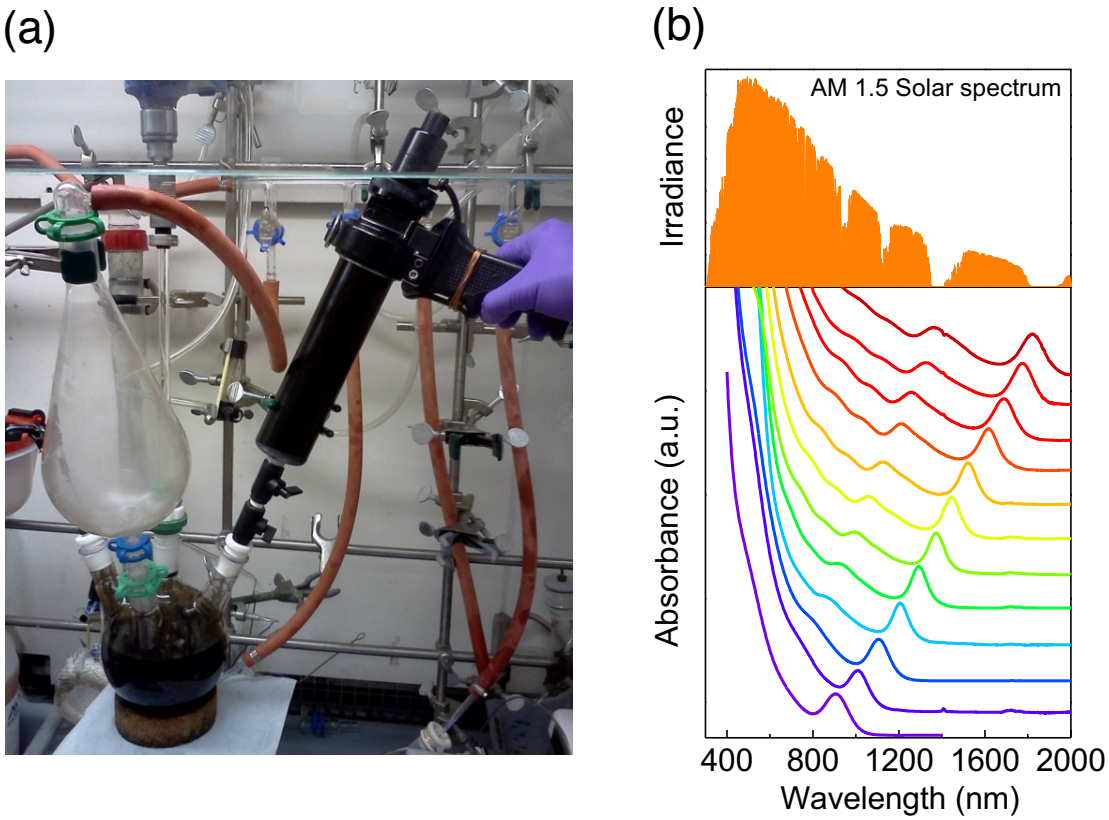

Figure 2.2 (a) A photograph of the setup for large-scale (~10 g) synthesis of PbS QDs. (b) Absorption spectra of PbS QDs with different bandgaps. The top panel shows the AM 1.5 solar spectra (spectral irradiance).
(b) data courtesy of Mark C. Weidman.

2.2 Ligand Exchange for Quantum Dot Solar Cells

QD solar cells are mostly fabricated *via* layer-by-layer deposition (Figure 2.3). As-synthesized QDs are capped with ligands with long aliphatic chains such as oleic acid ($CH_3(CH_2)_7CH{=}CH(CH_2)_7COOH$). While the long alkyl chains provide colloidal stability of QDs in solution, they impede charge transport between adjacent QDs in thin films. Therefore, for fabrication of QD solar cells, solid-state ligand exchange is performed to replace these long-chain ligands with short-chain ligands. In a layer-by-layer deposition step (Figure 2.3b), QDs with native long-

chain ligands are deposited onto a substrate. A solution containing short chain ligands is then applied to the film. These short-chain ligands replace the native long-chain ligands and reduce the interparticle distance, facilitating interactions between QDs. Furthermore, the ligand-exchanged QDs become insoluble in the original solvent, allowing subsequent deposition of the next layer. These processes are repeated until the desired thickness of QD films is reached. Typical techniques used for layer-by-layer deposition include spin-coating and dip-coating.

QD films are usually fabricated by the layer-by-layer deposition instead of single-step deposition because of the following reasons: (i) In order to fabricate a QD film with a desired thickness for solar cells (>150 nm) in single step, a QD solution with a high concentration is required, but this concentration might not be available. (ii) Solid-state ligand exchange might be incomplete for a thicker film because the solution containing the ligands is applied only to the surface of the film. (iii) Solid-state ligand exchange results in a volume contraction (Figure 2.3b). For a thicker film, the severe volume contraction may cause film cracking after ligand exchange. Some QD solar cells have been fabricated by single-step deposition method [41, 42]. In these studies, QDs are first ligand-exchanged with short-chain ligands in solution and dispersed in another solvent as "QD inks". The QD inks are then deposited onto a substrate followed by thermal annealing to remove residual solvent. However, QD solar cells fabricated in this method still underperform their counterparts fabricated by the layer-by-layer deposition method.

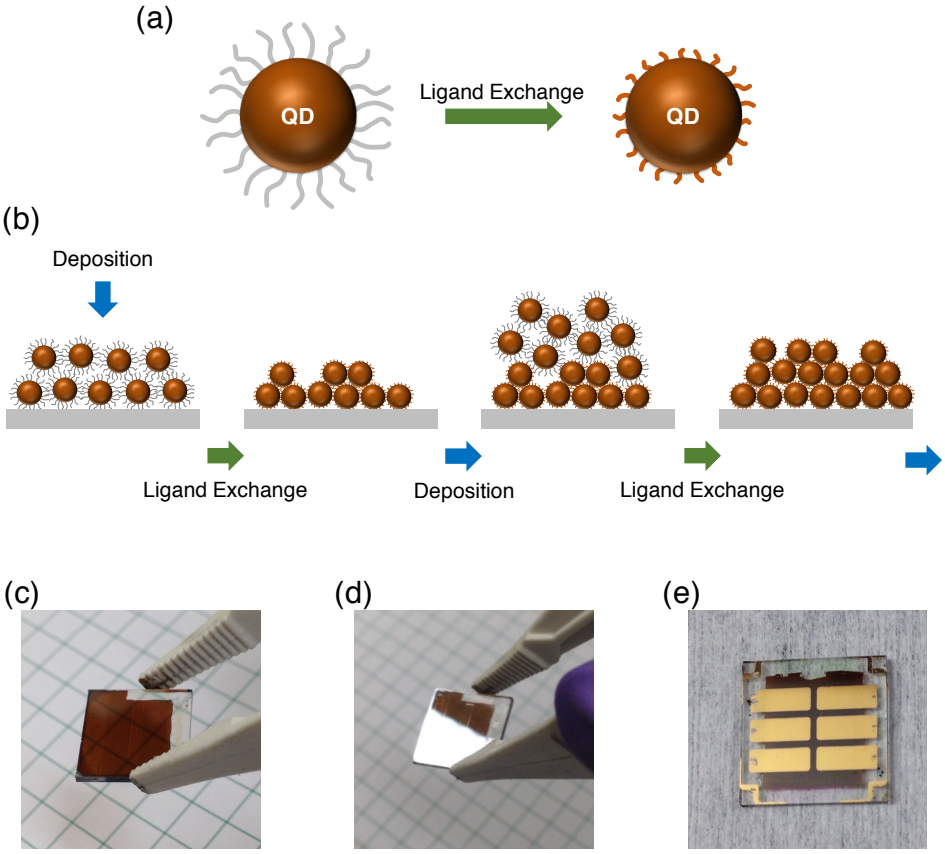

Figure 2.3 Fabrication of QD solar cells. (a) Ligand exchange. (b) Layer-by-layer deposition of QD films. (c)(d) Photographs of QD solar cells before the deposition of metal electrodes. The substrate size is 1.27 cm (0.5 inch) by 1.27 cm (e) A photograph of a complete device.

Various ligands can be used for ligand-exchange to "passivate" the surface of QDs (Figure 2.4). Organic molecules containing amine, carboxylate acid, or thiol functional groups to bind to the surface of QDs are mostly used as ligands for photovoltaic-grade QD films. Since the ligands are on the surface of QDs, they play important roles in determining the electronic properties of QD thin films [18, 33–35, 43–47]. QD films passivated with short-chain ligands generally show higher carrier mobilities as a result of a lower tunneling barrier for carrier transport from one dot to adjacent dots [45, 46]. This is not surprising because the interaction

(electronic coupling) between dots increases with decreasing interparticle distance. For a similar reason, bidentate ligands, in which one molecule contains two functional groups that *may* bind to two adjacent QDs, are preferred for solar cells. The most popular organic ligands used in QD solar cells are 1,2-ethanedithiol (EDT), 1,3-benzenedithiol (BDT), and 3-mercaptopropionic acid (MPA) [32, 48–51]. Halide anions (Cl^-, Br^-, I^-) as inorganic ligands or atomic ligands [33] have also been introduced and widely used since. In addition to carrier transport properties, the electronic energy levels of QD films can also be affected by the ligands (Figure 2.4). The shift of energy levels can be explained by the different intrinsic dipole moments of the ligands *and* the QD-ligand interface dipole [47]. The work described in Chapter 3 of this thesis takes advantage of the tunable energy levels to design a device architecture with improved performance.

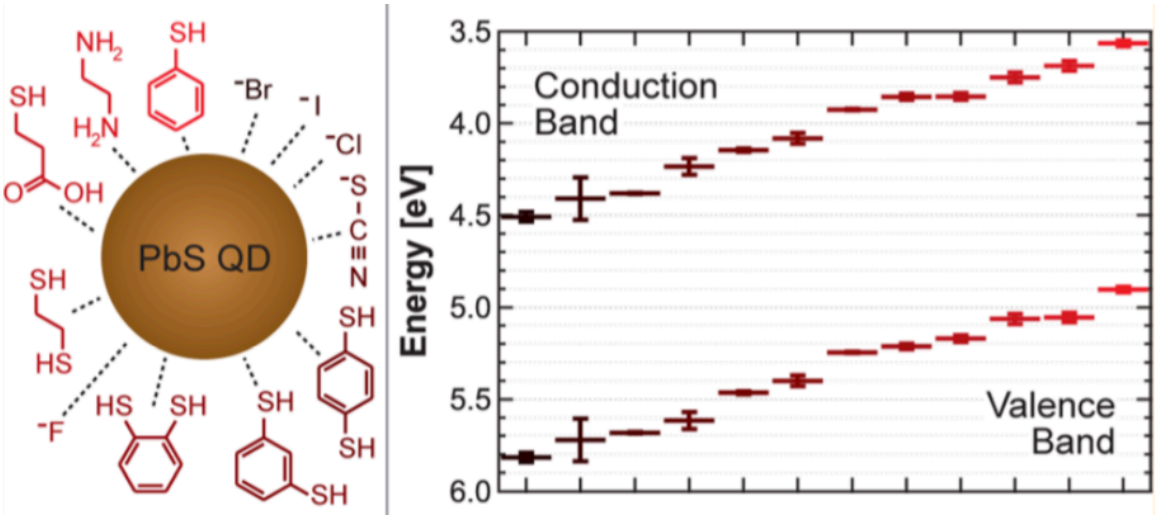

Figure 2.4 Various ligands used for fabricating QD films (left) and the corresponding energy levels with respect to vacuum (right).
Reprinted with permission from Ref. [47]. Copyright (2014) American Chemical Society

2.3 Progress in Quantum Dot Solar Cells

In earlier works, QDs have been incorporated in polymer-QD hybrid solar cells, where both the conjugated polymers and QDs contribute to light absorption [22, 52]. An all-inorganic solution-processed solar cell from CdSe and CdTe QDs also has been demonstrated [53], but the post-deposition sintering process converts the QDs into bulk thin films. Although these solar cells contain or are processed from QDs, they may not be termed as QD solar cells. QD solar cells, in which QDs with preserved quantum confinement effects serve as the main light absorbing layer, were demonstrated a few years later [48, 54, 55].

It has been shown that in strongly-coupled lead chalcogenide QD thin films, *i.e.* QDs with short ligands, free charge carriers can form upon photoexcitation without the need of an exciton dissociation interface [43, 56]. This process appears to have a high photon-to-carrier quantum yield [56]. In this regard, PbX QD thin films act like conventional semiconductors. Therefore, PbX QD solar cells can adopt planar thin-film device architectures such as Schottky junctions and *p*–*n* junctions (and their variants), unlike organic photovoltaics.

PbX QDs are found to behave like *p*-type semiconductors [18, 48], similar to many other chalcogenides. Early QD solar cells employed the simple Schottky junction device architecture (Figure 2.5a), in which QDs are sandwiched between a transparent conducting oxide (TCO) such as indium tin oxide (ITO) or fluorine-doped tin oxide (FTO) and a low work function metal such as aluminum (Al) [48, 54]. In this device architecture, the rectifying characteristics are a result of a Schottky junction between the *p*-type QDs and the low work function metal, and the TCO is a transparent electrode that forms an ohmic contact to QDs and allows the transmission of light. Despite the simple device architecture, fundamentally, Schottky junction solar cells would underperform *p*–*n* junction solar cells due to their high dark current. In addition, in QD Schottky junction solar cells, light is incident from the quasi-neutral region side with a lower carrier collection

probability. Therefore, the development of QD solar cells are mainly focused on *p*–*n* junction architectures.

For *p*–*n* junction QD solar cells (Figure 2.5b), QDs are often paired with an *n*-type inorganic material such as ZnO, TiO_2, and CdS [32, 49, 51, 57], or fullerene derivative PCBM (phenyl-C_{61}-butyric acid methyl ester) [58]. In this *p*–*n* heterojunction architecture, a high work function metal electrode such as gold (Au) is required to form an ohmic contact to the QDs; the light is incident from the depletion region side with high collection probability. The first certified record efficiency for QD solar cells on the *Best Research-Cell Efficiencies* chart published by the National Renewable Energy Laboratory (NREL) [29] was reported in 2010. This planar *p*–*n* heterojunction device, which showed a 2.94 % efficiency, is based on ZnO and PbS QDs, where the PbS QDs with a first exciton absorption peak at 950 nm (1.3 eV) are passivated by EDT [32] (QD solar cells mostly use QDs with absorption peaks around 850 – 950 nm since this is within the optimal bandgap range for single junction solar cells as predicted by the Shockley–Queisser limit).

It was found that although Au has a high work function, sometimes an unfavorable back Schottky barrier may still form between Au and PbS QDs, leading to reduced current collection efficiencies and S-shape *J*–*V* characteristics [36, 50, 59]. The introduction of a MoO_3 interlayer between PbS QDs and Au was shown to successfully remove this unfavorable barrier and decouple the performance of QD solar cells from the work function of the electrode [36, 50]. This demonstration led to the second certified record efficiency of 4.4 % on the NREL chart in 2011 from a EDT passivated PbS QD solar cells with an ITO/ZnO/PbS/MoO_3/Al device architecture [36]. The MoO_3 interlayer has since been widely used in QD solar cells.

The next certified record efficiency of 5.1 % was also reported in 2011 with the development of "atomic" ligands [33]. The device with an architecture of FTO/TiO_2/PbS/MoO_3/Au/Ag employed bromide (Br^-) as the ligand for solid-state ligand exchange by treating the PbS QDs with cetyltrimethylammonium

bromide (CTAB). Prior to deposition, the PbS QDs underwent an additional treatment with $CdCl_2$ salts in solution, which left some Cd or Cl on the surface of PbS QDs. In the same work, other inorganic ligands such as Cl^-, I^-, and SCN^- were also explored with success. In 2012, before the beginning of this thesis work, the certified efficiency of QD solar cells reached 7.0 % from a device with the same device architecture but different ligand treatments. In this so-called "hybrid passivation" approach, the PbS QDs were first treated with inorganic salt $CdCl_2$ in solution. For the solid-state ligand exchange process, the organic ligand MPA was used [34]. It was claimed that through this approach, the Cl^- and MPA could passivate different types of defect states to improve the device performance.

Part of this thesis work detailed in Chapter 3 contributed to the next certified record efficiency of 8.6 % on the NREL chart in late 2013 (the work was published in 2014 [35]). At the time of the writing of this thesis, the certified record efficiency for QD solar cells has reached 10.6 %.

Other notable progresses in QD solar cells include QD tandem cells and the carrier multiplication (CM) effects, also known as multi-exciton generation (MEG), in operational QD solar cells. QD tandem cells consisting of a sub-cell with 1.6 eV PbS QDs and another with 1.0 eV PbS QDs demonstrated the feasibility of low-cost solution-processed QD multi-junction solar cells [60, 61]. The signatures of CM or MEG have been observed in PbX QDs through spectroscopic studies [62, 63]. The report of PbSe QD solar cells with the peak external quantum efficiency of photocurrent exceeding 100 % is the first direct evidence of the MEG effects in QD solar cells, indicating that one high energy photon can create more than one pair of photogenerated carriers [44]. These demonstrations highlight the potential of QDs for next-generation solar cells that could exceed the Shockley–Queisser limit. (Note: in theory, CM can raise the efficiency limit. However, the potential gain from CM may not be significant since it could only occur when a high energy photon ($>2E_g$) is absorbed and the CM yield in QDs might not be as efficient as originally suggested [62, 63].)

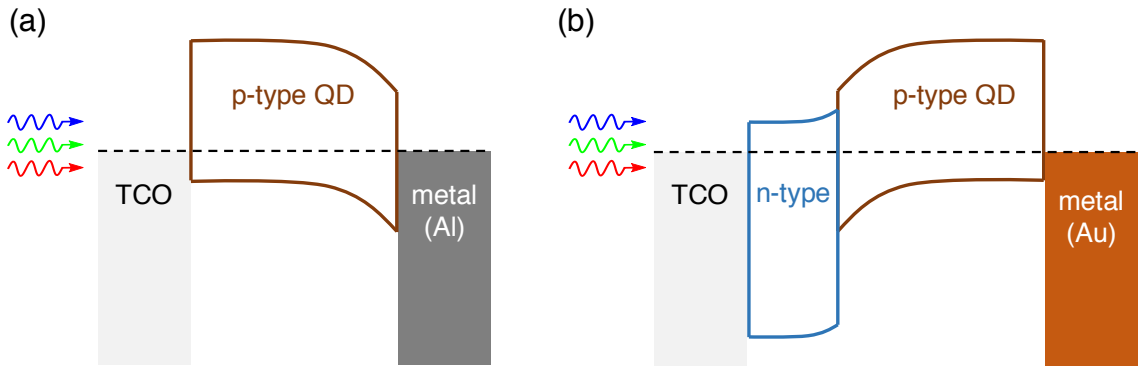

Figure 2.5 Band diagrams and device architectures for QD solar cells (a) Schottky junction. (b) p–n junction. TCO: transparent conducting oxide.

2.4 Challenges

Despite a rapid progress in the development of QD solar cells, many challenges exist in the improvement of device performance. The main issues present in QD solar cells include (1) processing conditions and device stability, (2) insufficient J_{SC} due to the trade-off between light absorption and carrier collection, and (3) relatively low V_{OC}.

Poor device stability has long been a common issue in various types of solution-processed solar cells, particularly in organic and organometallic halide perovskite solar cells. Most solution-processed solar cells are sensitive to air (oxygen and moisture). Their fabrication, testing, and storage require an inert atmosphere such as a nitrogen-filled glovebox. The device performance still degrades over time, even if it is encapsulated and stored in an air-free environment. This is also the case for PbSe QD solar cells, which lose diode characteristics within a few minutes of air exposure [48]. In terms of stability, PbS QD solar cells have an advantage over PbSe QDs and other solution-processed solar cells. In fact, all the record efficient PbS QD solar cells are fabricated in ambient air [32–36]. However, previously reported devices still show degradation when stored in air [33, 34]. Furthermore, the n-type ZnO or TiO_2 layer in these previously reported PbS QD

solar cells are processed at high temperature (260 °C for ZnO [32, 36] and 550 °C for TiO_2 [33, 34]), which is not compatible with flexible substrates. These issues will be addressed in Chapter 3.

The collection of photogenerated carriers in PbS QD solar cells mainly relies on the drift current originated from carriers generated inside the depletion region. This is because of the short carrier diffusion lengths (<100 nm [64]), which are much shorter than that in Si and other bulk chalcogenide solar cells (on the order of μm). The depletion region width in PbS QD solar cells is ~200 nm [50]. To absorb more sunlight, a device thicker than the depletion region width is required (Figure 2.6). However, in a device with a short carrier diffusion, increasing the thickness would not increase the overall collected photocurrent because the collection probability of carriers generated in the quasi-neutral region is low (Section 1.3.3). It is this trade-off between light absorption and carrier collection that limits the J_{SC} in present QD solar cells. The origin of the short carrier diffusion length is likely to be the same as that of the relatively low V_{OC} ($qV_{OC} < 0.5E_g$) in QD solar cells. These issues will be discussed in Chapter 4 and Chapter 5.

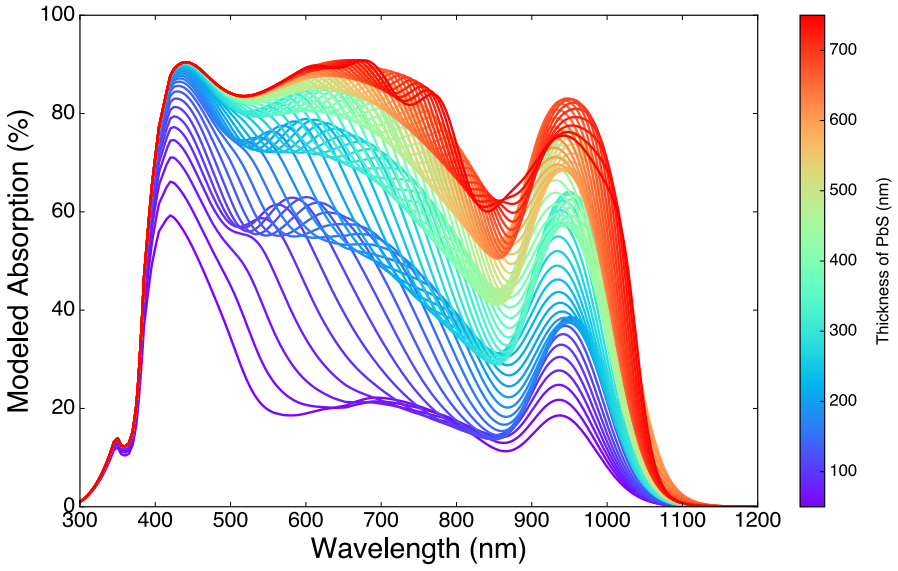

Figure 2.6 Modeled absorption in the PbS QDs layer in ITO/ZnO/PbS/Au solar cells with varying thickness of the PbS QDs layer.

CHAPTER 3

Improved Performance and Stability in Quantum Dot Solar Cells through Band Alignment Engineering

The majority of this chapter is adapted with permission from Ref [35]:
C.-H. M. Chuang, P. R. Brown, V. Bulović & M. G. Bawendi, *Nature Materials*, **13,** 796–801 (2014).

Abstract

Solution processing is a promising route for the realization of low-cost, large-area, flexible, and light-weight photovoltaic devices with short energy payback time and high specific power. However, solar cells based on solution-processed organic, inorganic, and hybrid materials reported thus far generally suffer from poor air stability, require an inert-atmosphere processing environment, or necessitate high temperature processing [30], all of which increase manufacturing complexities and costs. Simultaneously fulfilling the goals of high efficiency, low-temperature fabrication conditions, and good atmospheric stability remains a major technical challenge, which may be addressed, as we demonstrate here, with the development of room-temperature solution-processed ZnO/PbS quantum dot (QD) solar cells. By engineering the band alignment of the QD layers through the use of different ligand treatments, a certified efficiency of 8.55% has been reached. Furthermore, the performance of unencapsulated devices remains unchanged for over 150 days of storage in air. This material system introduces a new approach towards the goal of high-performance air-stable solar cells compatible with simple solution processes and deposition on flexible substrates.

3.1 Introduction

Near-infrared PbS QDs composed of earth-abundant elements [39] have emerged as promising candidates for photovoltaic applications because of a tunable energy bandgap that covers the optimal bandgap range for single and multi-junction solar cells [30]. The QD surface ligands [18, 33, 34, 43, 44] and the photovoltaic device architecture [32, 51, 54, 57, 58, 65–69] play crucial roles in determining the optoelectronic properties of QD solar cells. Advances in QD surface passivation, particularly through the use of halide ions as inorganic ligands [33], have led to rapid improvements in QD solar cell power conversion efficiencies to 7 % [34, 67, 68] as a result of a lower density of trapped carriers than in their organic ligands counterparts [33]. In addition, recent studies have demonstrated the ability to control the band edge energies of QD films through ligand exchange [70–72]. However, fabrication of these recent QD devices requires high-temperature annealing (>500 °C) of the TiO_2 window layer [34, 68] or two different processing atmospheres, including an inert gas environment [67]. Although good stability has been claimed, the devices still show performance degradation to ~85% of their original efficiencies within one week even under inert atmosphere [34, 68]. Here, we demonstrate ZnO/PbS solar cells in which the PbS QDs and ZnO nanocrystals are both solution-processed in air and at room temperature. We demonstrate a device architecture that employs layers of QDs treated with different ligands for different functions by utilizing their relative band alignment—a layer of inorganic-ligand-passivated QDs serves as the main light-absorbing layer and a layer of organic-ligand-passivated QDs serves as an electron-blocking/hole-extraction layer. The devices show significant improvements in power conversion efficiency and long-term air-stability, as compared to previously reported devices.

3.2 Device Structure

Figure 3.1 shows the schematics of the device structures employed in this work. Oleic-acid-capped PbS QDs with the first exciton absorption peak at λ =901

nm in solution (Figure 3.2) are used to fabricate the PbS QD thin films. Tetrabutylammonium iodide (TBAI) and 1, 2-ethanedithiol (EDT) are used as the inorganic and organic ligands for solid-state ligand exchange. After solid-state ligand exchange, the first exciton absorption peak shifts to $\lambda \approx 935$ nm, which corresponds to an optical bandgap $E_g = 1.33$ eV. The electron-selective layer is solution-processed ZnO nanocrystals (Figure 3.3). The anode material is MoO_3/Al, MoO_3/Au, or Au.

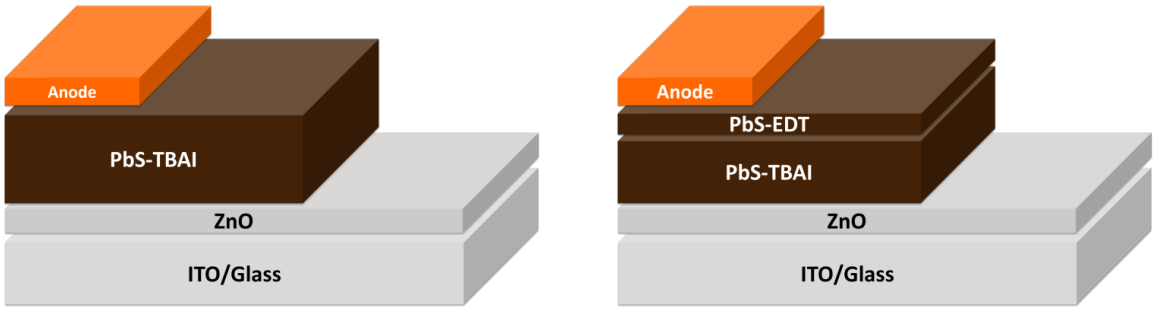

Figure 3.1 Photovoltaic device architectures.

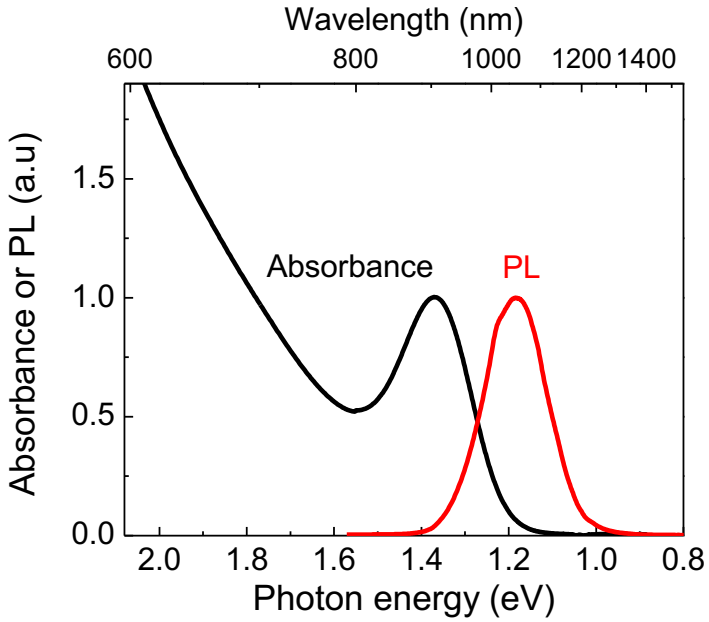

Figure 3.2 Absorption and photoluminescence spectra of PbS QDs in octane solution.

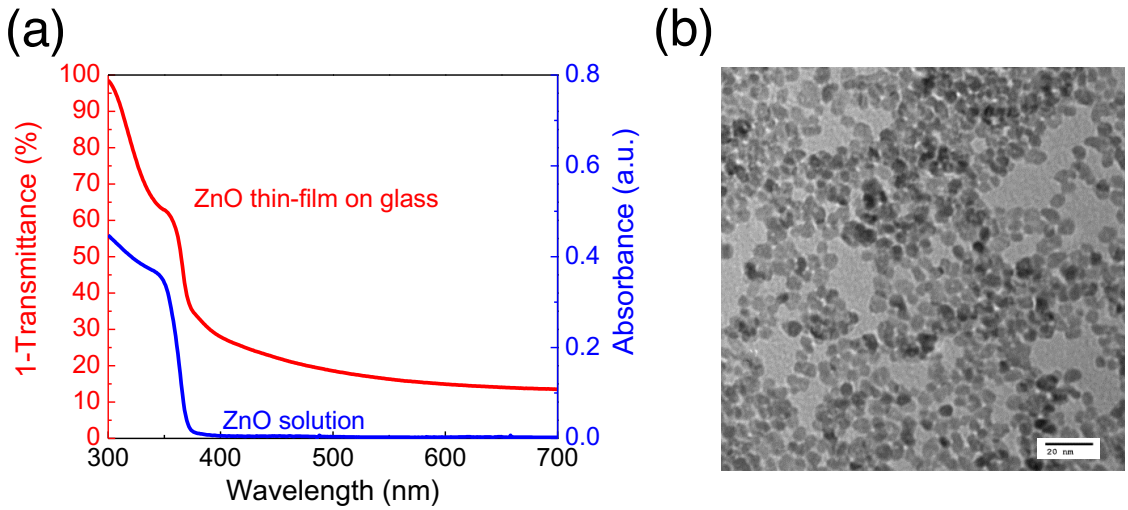

Figure 3.3 (a) Absorption spectra of ZnO nanocrystal solution and ZnO thin film on glass substrate. The absorption onset at wavelength λ~370 nm corresponds to a bandgap of ~3.35 eV. The background at longer wavelengths in the thin film absorption spectrum is due to light scattering and reflection. (b) Transmission electron microscopy (TEM) image of ZnO nanocrystals (scale bar: 20nm).

3.3 Current–Voltage Characteristics

3.3.1 Improved Performance

The J–V characteristics of photovoltaic devices with Au anodes are shown in Figure 3.4. The device consisting of 12 PbS-TBAI layers (corresponding to ~220 nm thick film) shows a power conversion efficiency of 6.0±0.4 %, which is higher than the previously reported TiO_2/PbS-TBAI devices consisting of PbS QDs with an additional solution phase $CdCl_2$ treatment and MoO_3/Au/Ag anode [33]. Although PbS-EDT-only devices show a lower J_{SC} than PbS-TBAI-only device (see section 3.3.2), replacing the top-most 2 PbS-TBAI layers with 2 PbS-EDT layers significantly improves the J_{SC}, V_{OC}, and fill factor (FF), resulting in a ~35% improvement in power conversion efficiency to 8.2±0.6% with a 9.2 % lab-champion device (Table 3-1).

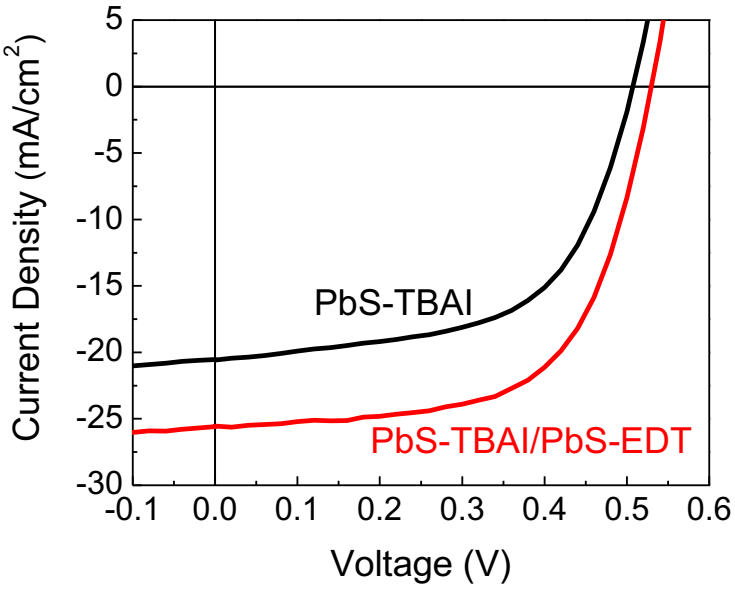

Figure 3.4 Representative J–V characteristics of photovoltaic devices with Au anodes under simulated AM 1.5 irradiation (100 mW/cm^2). The PbS-TBAI device consists of 12 layers of PbS-TBAI and the PbS-TBAI/PbS-EDT device consists of 10 layers of PbS-TBAI and 2 layers of PbS-EDT.

	V_{OC} (V)	J_{SC} (mA/cm^2)	*FF* (%)	*PCE* (%)
PbS-TBAI*	0.506±0.009 (0.519)	20.7±1.1 (22.8)	57.7±1.9 (59.6)	6.0±0.4 (7.0)
PbS-TBAI/PbS-EDT*	0.525±0.016 (0.544)	25.3±1.1 (26.5)	61.6±1.3 (63.8)	8.2±0.6 (9.2)
PbS-TBAI/PbS-EDT certified§	0.5546±0.0055	24.2±0.7	63.8±1.3	8.55±0.18

Table 3-1 Solar cell performance parameters. The numbers in parentheses represent the values obtained for the best-performing cell. *To account for experimental errors, the reported averages and deviations are for samples of between 6 and 9 devices on the same substrate from measurements performed in between 1 and 75 days of air-exposure. §Error bars: quoted uncertainties with an approximately 95% level of confidence.

3.3.2 PbS-TBAI as the Main Light-Absorbing Layer

To understand the properties and the functions of the PbS-TBAI and PbS-EDT layers in the photovoltaic devices, we fabricate devices with the same total numbers of PbS layers but different numbers of PbS-TBAI and PbS-EDT layers:

- Device A (TBAI*12): PbS-TBAI-only
- Device B (TBAI*10/EDT*2)
- Device C (TBAI*6/EDT*6)
- Device D (TBAI*2/EDT*10)
- Device E (EDT*12): PbS-EDT-only

The representative *J*–*V* curves of Device A to E are shown in Figure 3.5. We find that the PbS-TBAI-only device (Device A) shows a higher J_{SC} than the PbS-EDT-only device (Device E), even though their thickness and absorption are comparable. Device E also exhibits the lowest J_{SC} but the highest V_{OC} among all devices. By replacing the top 2 PbS-TBAI layers with PbS-EDT layers (Device B), the J_{SC}

significantly increases compared to the PbS-TBAI-only device (Device A). We conclude that in this PbS-TBAI/PbS-EDT device structure, the PbS-TBAI is the main layer to absorb light and generate photocurrent. The improvement in J_{SC} in the PbS-TBAI/PbS-EDT device shown in Figure 3.4 is not due to additional light absorption from the PbS-EDT layer. This can be further supported by the progressively decreasing J_{SC} with decreasing numbers of TBAI layers in Device B, C, and D.

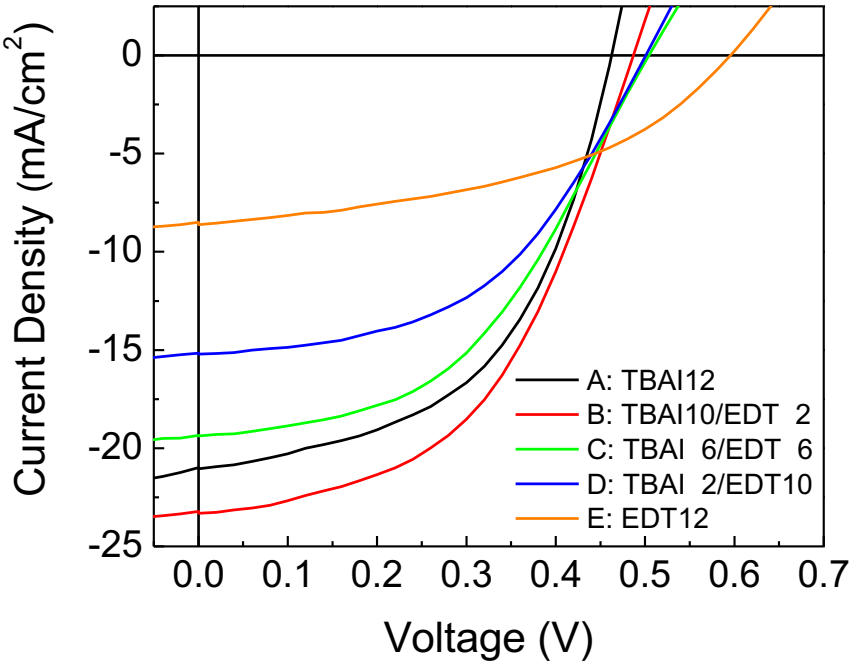

Figure 3.5 Comparison of devices with different numbers of PbS-TBAI and PbS-EDT layers. The device structure is ITO/ZnO/PbS-TBAI(x)/PbS-EDT(y)/ MoO_3/Al, where x and y denote the numbers of PbS-TBAI and PbS-EDT layers. The total number of PbS layers is 12 layers in all devices.

3.4 Measurements of Energy Levels

We attribute the improvement in efficiency to the band offsets between the two PbS QD layers which effectively block electron flow to the anode while facilitating hole extraction. We use ultraviolet photoelectron spectroscopy (UPS) to determine the band edge energies with respect to vacuum in PbS QD films.

3.4.1 Principles of Ultraviolet Photoelectron Spectroscopy

UPS is used to determine the Fermi level (E_F) and the valence band maximum (E_V) with respect to vacuum level (E_{VAC}) of the PbS thin films. The basic principles and an example spectrum are shown in Figure 3.6. For a photoelectron to escape the sample surface and to be collected, it has to have sufficient energy to overcome the sum of the binding energy (with respect to E_F) of its initial level and the work function (Φ), where $\Phi = E_{VAC} - E_F$. Therefore, for a fixed incident photon energy of 21.2 eV, the secondary electron cut-off (high binding energy edge) represents photoelectrons with zero kinetic energy (E_k) when they escape the sample surface and their initial level is shown as the grey dotted line inside the DOS in Figure 3.6a. The work function Φ is determined by the difference between the incident photon energy (21.2 eV) and the binding energy of the secondary electron cut-off. In the example spectrum (Figure 3.6b), the cut-off binding energy is 16.43 eV as determined by the intersection of the linear portion of the spectrum and the baseline. The work function of this sample is thus $\Phi = 21.2 - 6.43 = 4.77$ eV; that is, E_F is -4.77 eV with respect to E_{VAC}.The difference between E_F and E_V is determined by the intersection of the linear portion of the spectra near the Fermi edge (low binding energy region) with the baseline. The example spectrum has a $E_F - E_V = 0.82$ eV. Therefore, its valence band maximum E_V is -5.59 eV with respect to E_{VAC}.The conduction band minimum (E_C) is further calculated by adding the optical bandgap, as determined by the position of the lowest exciton absorption peak, to E_V.

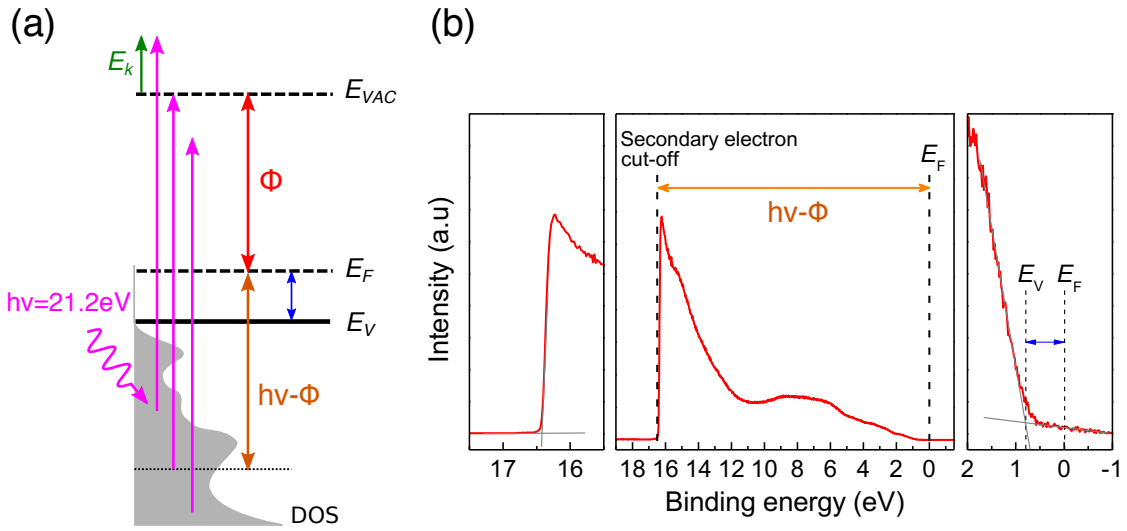

Figure 3.6 Basic principles of UPS measurements. (a) Schematic illustration of the energy diagram. DOS: density of states in the valence band. (b) An example UPS spectrum. The left panel shows the magnified view of the high binding energy region and the right panel shows the magnified view of the low binding energy region. Grey lines represent the linear fits.

3.4.2 Band Alignment between PbS-TBAI and PbS-EDT

Thickness-dependent UPS is used to determine the band alignment between PbS-TBAI and PbS-EDT. The thickness of the thickest PbS-EDT overlayer corresponds to the thickness generally used in devices and is determined to be ~45 nm by a profilometer. This thickest PbS-EDT layer was obtained in the same manner as for the device fabrication (2 layer-by-layer spin-coating steps from 50 mg/ml PbS solution followed by ligand exchange with EDT solution). The thinner PbS-EDT layers (4.5 nm, 9 nm, 13.5 nm) were obtained by spin-coating dilute PbS solution (10 mg/ml) on PbS-TBAI. The thicknesses of these thinner PbS-EDT layers were estimated by the solution concentration (10 mg/mL, 5 times less than for the thickest layer) and the numbers of layer-by-layer spin-coating steps (1, 2, and 3 steps, respectively).

As shown in Figure 3.7, two distinct peaks from PbS-EDT (~3.8 eV and ~5.8 eV) appear in the UPS spectra after we add PbS-EDT on PbS-TBAI. The secondary electron cut-off shifts to higher binding energy while the $E_F - E_V$ decreases with increasing thickness of PbS-EDT. These features indicate interfacial band bending at the PbS-TBAI/PbS-EDT interface. The fitted band positions are summarized in Table 3-2. We note that the saturation of the spectral shape and the band positions at ~13.5nm also confirms that the ~45nm of PbS-EDT layer used in our photovoltaic devices is thick enough to result in a continuous overlayer and its thickness may be beyond the width of the interfacial band bending region.

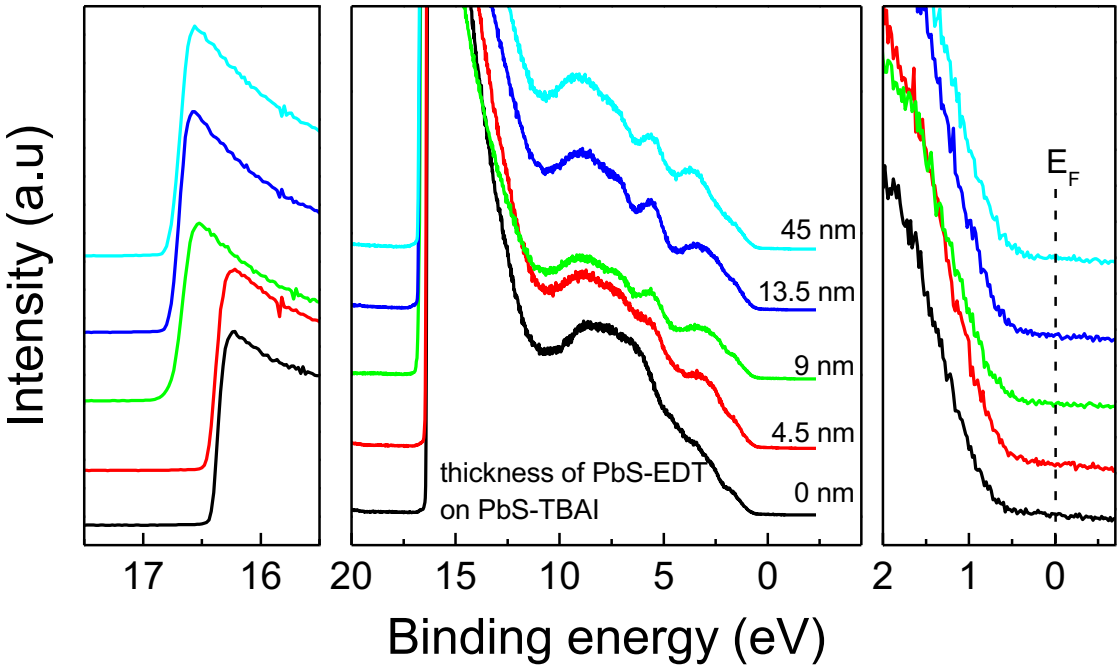

Figure 3.7 UPS spectra of PbS-TBAI films covered with different thicknesses of PbS-EDT. The left panel shows the secondary electron cut-off region and the right panel shows the magnified spectra near Fermi edge. Spectra are shifted for clarity.

Sample	E_C	E_F	E_V	$E_F - E_V$
TBAI (110nm)	-4.26	-4.77	-5.59	0.82±0.02
TBAI (110nm)/ EDT (4.5nm)	-4.10	-4.73	-5.46	0.70±0.02
TBAI (110nm)/ EDT (9.0nm)	-3.78	-4.41	-5.11	0.70±0.02
TBAI (110nm)/ EDT (13.5nm)	-3.68	-4.38	-5.01	0.63±0.02
TBAI (110nm)/ EDT (45.0nm)	-3.68	-4.38	-5.01	0.63±0.02

Table 3-2 Band positions with respect to vacuum as determined from the UPS spectra in Figure 3.7. The error bars in $E_F - E_V$ represent the error from fitting.

The thickness-dependent UPS data allow us to determine the relative energy level alignment at the PbS-TBAI/PbS-EDT interface. At equilibrium, the Fermi level in the whole sample must align. Therefore, the relative band alignment can be determined by matching the Fermi level and then placing the band edge energies with respect to the Fermi level. It can be better understood with the help of the schematic illustrations shown in Figure 3.8. The left figure shows the experimentally determined band positions with respect to vacuum level as a function of the thickness (d_n) of PbS-EDT on PbS-TBAI. The reduction of work function after adding the PbS-EDT layer implies a downward vacuum level shift, whereas the reduction of $E_F - E_V$ implies an upward band bending from the interface to PbS-EDT. Once the thickness of the PbS-EDT is greater than the width of the interfacial band bending region, the band positions and the UPS spectra reach saturation (d_2 and d_3). The right figure shows the band alignment deduced from the left figure.

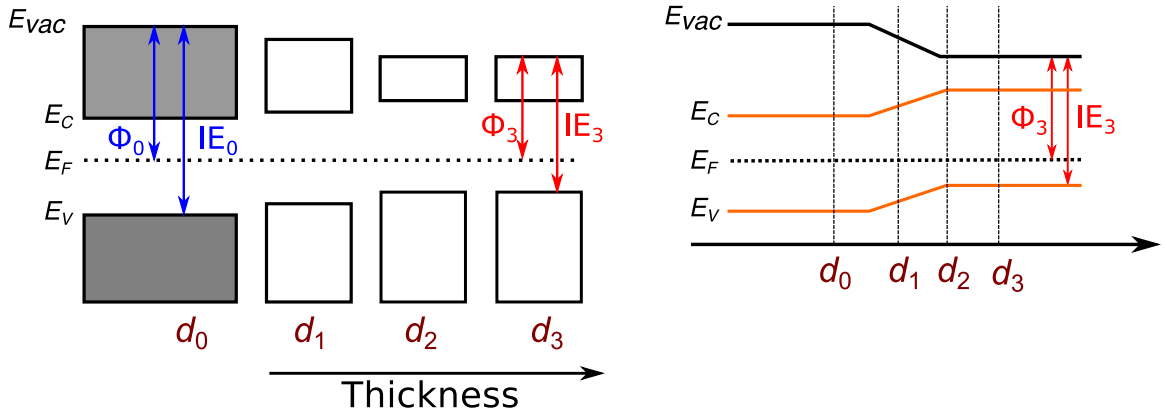

Figure 3.8 Schematic illustrations explaining how to determine the band alignment at the interface from the UPS spectra. Left: The band positions as a function of the overlayer thickness (d_n). Here, the conduction band edge (E_C), valence band edge (E_V) and vacuum levels (E_{VAC}) are referenced to the Fermi level (E_F). IE: ionization energy. Right: The corresponding band alignment. For simplicity, the conduction band and valence band are connected by straight lines.

3.5 Band Alignment for Performance Improvement

3.5.1 Relative Band Alignment

The energy levels of pure PbS-TBAI and PbS-EDT films deduced from UPS spectra are plotted on the left of Figure 3.9a. PbS-TBAI exhibits a deeper work function of 4.77 eV (i.e. E_F = -4.77 eV with respect to vacuum) than PbS-EDT. We attribute the difference in their work functions to the difference between the Pb-halide anion and the Pb-thiol-carbon interactions, which give rise to different surface dipole moments as is discussed elsewhere [72]. In addition, the difference between the Fermi level and valence band edge (E_V) in PbS-TBAI is greater ($E_F - E_V$ =0.82 eV) than that in PbS-EDT ($E_F - E_V$ =0.63 eV). According to the individually determined band positions, the large conduction band offset (0.68 eV) between PbS-TBAI and PbS-EDT should block electron flow from the PbS-TBAI layer to the PbS-EDT layer. However, since the interactions between the PbS-

TBAI and the PbS-EDT layers can affect the interfacial band bending, the actual band offsets in the device must be measured directly.

To determine the band alignment at the PbS-TBAI/PbS-EDT interface, we performed UPS measurements on PbS-TBAI films covered with different thicknesses of PbS-EDT. The fitted band positions from the UPS spectra (Figure 3.7 and Table 3-2) are plotted on the right side of Figure 3.9a. As the thickness of the PbS-EDT layer increases, the Fermi level with respect to vacuum shifts to shallower energy levels and reaches saturation when the thickness of the PbS-EDT layer exceeds 13.5nm. The shift indicates the formation of an interfacial dipole, which results in a reduction of the work function and a downward vacuum level shift at the interface. Moreover, the difference between the Fermi level and the valence band edge decreases with increasing PbS-EDT layer thickness. The energy level alignment at the PbS-TBAI/PbS-EDT interface deduced from the thickness-dependent UPS data is plotted in Figure 3.9b.

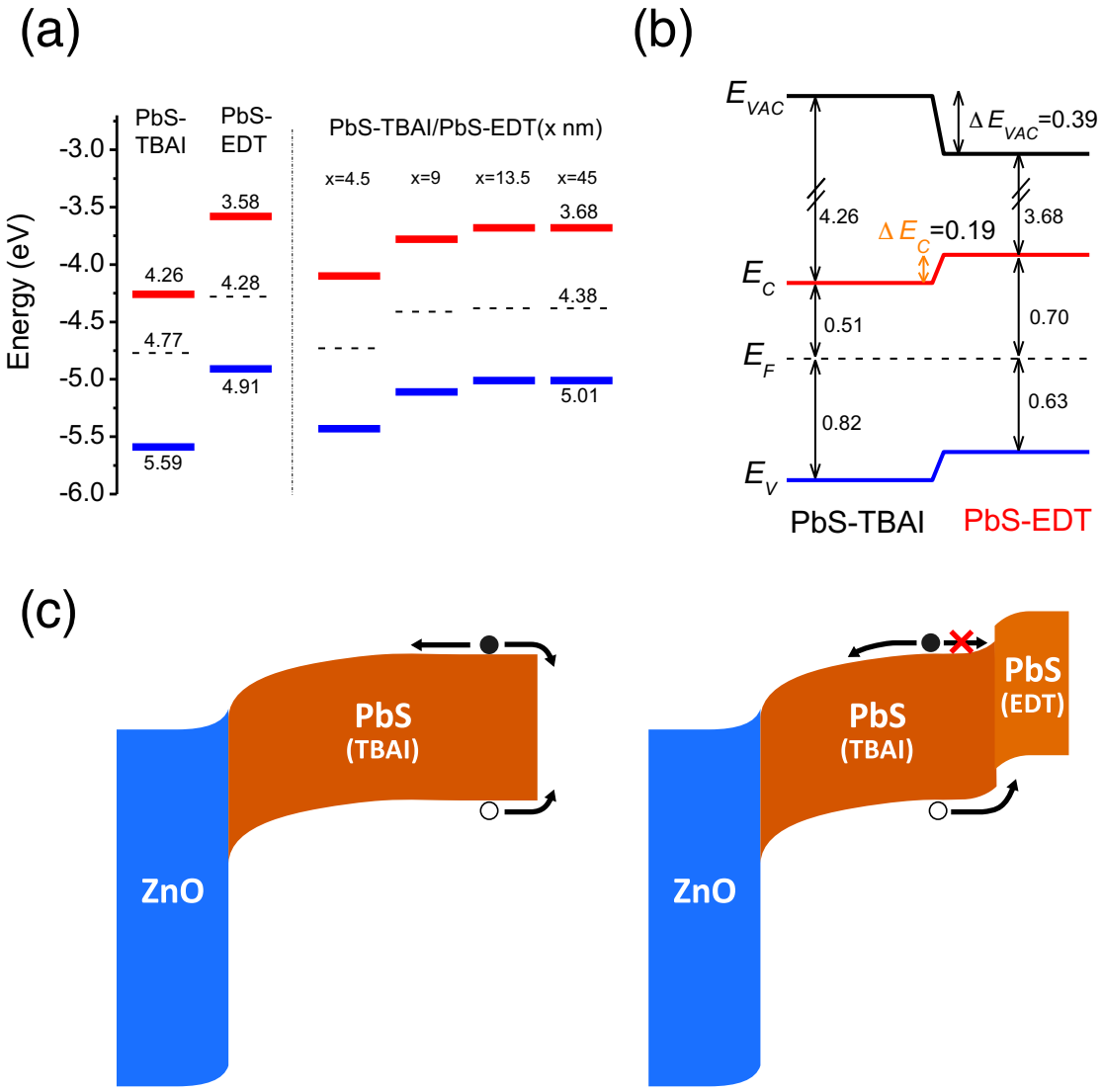

Figure 3.9 Energy level diagrams of PbS QDs and photovoltaic devices containing the QDs. (a) Energy levels with respect to vacuum for PbS-TBAI, PbS-EDT, and PbS-TBAI films covered with different thicknesses of PbS-EDT layers. The Fermi levels (E_F, dashed line) and valence band edges (E_V, blue lines) were determined by UPS. The conduction band edges (E_C, red lines) were calculated by adding the optical bandgap energy of 1.33 eV, as determined from the first exciton absorption peak in the QD thin films, to E_V. (b) Schematic energy level alignment at PbS-TBAI and PbS-EDT interfaces deduced from UPS. E_{VAC}: vacuum level. (c) Schematic illustration of band bending in ZnO/PbS-TBAI and ZnO/PbS-TBAI/PbS-EDT devices at short-circuit conditions.

3.5.2 Improved Photocurrent Collection

The band alignment demonstrates the role of the PbS-EDT layer as an electron-blocking/hole-extraction layer between the PbS-TBAI layer and the anode, which leads to an improved photocurrent collection efficiency and enhanced device performance in the PbS-TBAI/PbS-EDT devices. In the PbS-TBAI-only device, electron flow from PbS-TBAI to the anode, which is in the opposite direction to the photocurrent, and interfacial recombination at the PbS/anode interface are possible loss mechanisms (Figure 3.9c). In the PbS-TBAI/PbS-EDT device, the conduction band offset between the PbS-TBAI and PbS-EDT layers provides an energy barrier that prevents photogenerated electrons from flowing to the PbS-EDT layer, while the valence band offset provides an additional driving force for the flow of photogenerated holes to the PbS-EDT layer. The insertion of the PbS-EDT layer not only prevents electron flow from PbS-TBAI to the anode but may also reduce surface recombination of photogenerated electrons and holes at the PbS-TBAI/anode interface.

The interfacial band bending makes an additional minor contribution to the improved J_{SC}. The band bending at the PbS-TBAI/PbS-EDT interface implies the formation of a depletion region adjacent to this junction, which effectively extends the overall depletion width in the PbS-TBAI light-absorbing layer. This effect is similar to that in previously reported graded-doping devices [67, 68] where control of carrier concentrations through ligand exchange extends the depletion region, but there without altering the band edge positions of the PbS QD layers [68]. The extension of the depletion region in those graded-doping devices accounts for a marginal increase ($<5\%$) in J_{SC} compared to ungraded devices [67, 68].

In our study, the PbS-TBAI/PbS-EDT devices typically show ~20% improvements in J_{SC} compared to PbS-TBAI-only devices (Figure 3.10). As shown in Figure 3.11a, the PbS-TBAI/PbS-EDT device exhibits a higher external quantum efficiency (EQE) than that in the PbS-TBAI-only device at longer wavelengths. Long-wavelength photons have longer penetration depths due to the

smaller absorption coefficients. Therefore, a higher fraction of long-wavelength photons are absorbed deeper in the film relative to the short-wavelength photons whose absorption is predominantly close to the ZnO/PbS-TBAI interface. The EQE enhancement as a function of wavelength is shown in Figure 3.11b, which is calculated as $\Delta EQE/EQE_{PbS\text{-}TBAI}$, where $\Delta EQE = EQE_{PbS\text{-}TBAI/PbS\text{-}EDT} - EQE_{PbS\text{-}TBAI}$. It can be seen that the EQE enhancement is higher at longer wavelengths. The improvement in EQE at longer-wavelengths clearly indicates a better photocurrent collection efficiency especially in the region close to the PbS-TBAI/PbS-EDT interface, consistent with the proposed mechanisms. The J_{SC} calculated by integrating the EQE spectra with AM 1.5 solar spectrum for PbS-TBAI-only and PbS-TBAI/PbS-EDT devices are 21.0 and 23.7 mA/cm^2, respectively, which show good agreement with the measured J_{SC} (20.7±1.1 and 25.3±1.1 mA/cm^2).

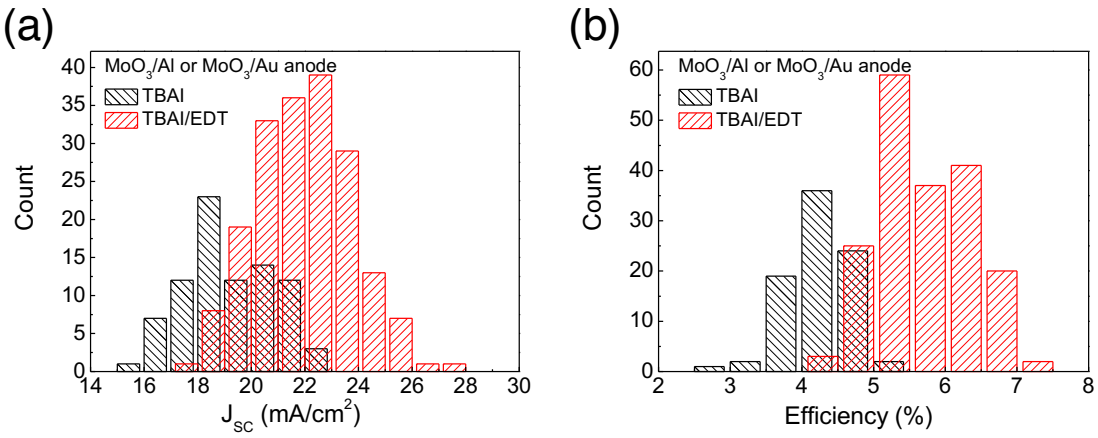

Figure 3.10 Histograms of J_{SC} and power conversion efficiency of devices with MoO_3 anodes. The histograms show the performance of devices on different substrates from different batches using the same size of PbS QDs. The PbS-TBAI/PbS-EDT devices consistently outperform the PbS-TBAI devices in every batch of devices we fabricated.

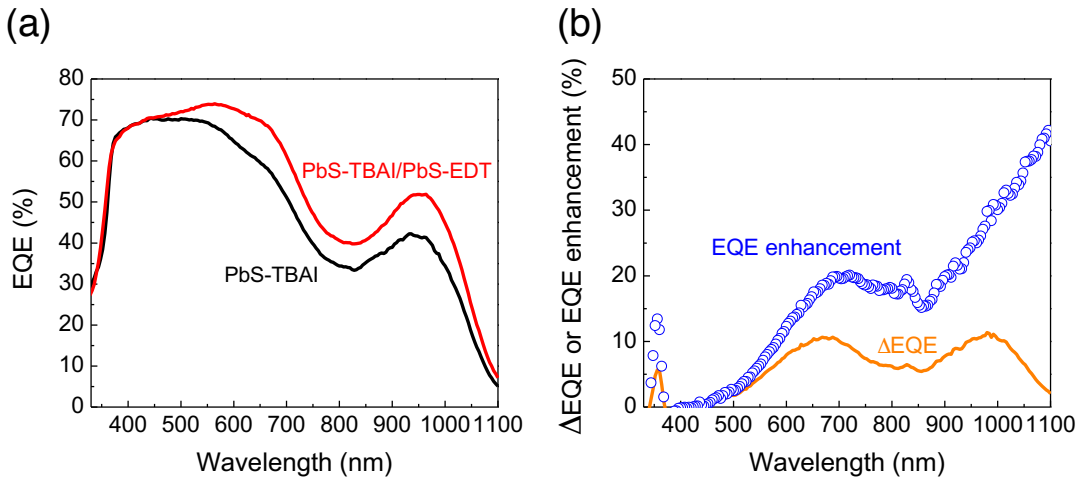

Figure 3.11 (a) EQE spectra of the PbS-TBAI and PbS-TBAI/PbS-EDT devices shown in Figure 3.4. (b) EQE enhancement.

We also performed optical modeling to further support the arguments regarding the longer-wavelength photons. The modeled photon absorption profiles (Figure 3.12) confirm that a significant portion of the longer wavelength photons (>500nm) is absorbed deeper in the film, i.e. close to the PbS-TBAI/PbS-EDT interface. Furthermore, the results show that the optical field is similar in PbS-TBAI-only and PbS-TBAI/PbS-EDT devices. No new optical modes have developed in the PbS-TBAI/PbS-EDT devices. Therefore, the ~20% improvement in EQE is unlikely to be due to any optical interference effects.

In summary, the improvement in device performance is mainly from band alignment effects as supported by the UPS data. The EQE spectra support the proposed mechanisms, which predict a better photocurrent collection efficiency *especially* in (but not limited to) the region close to the PbS-TBAI/PbS-EDT interface where the contribution from the longer wavelength photons is higher.

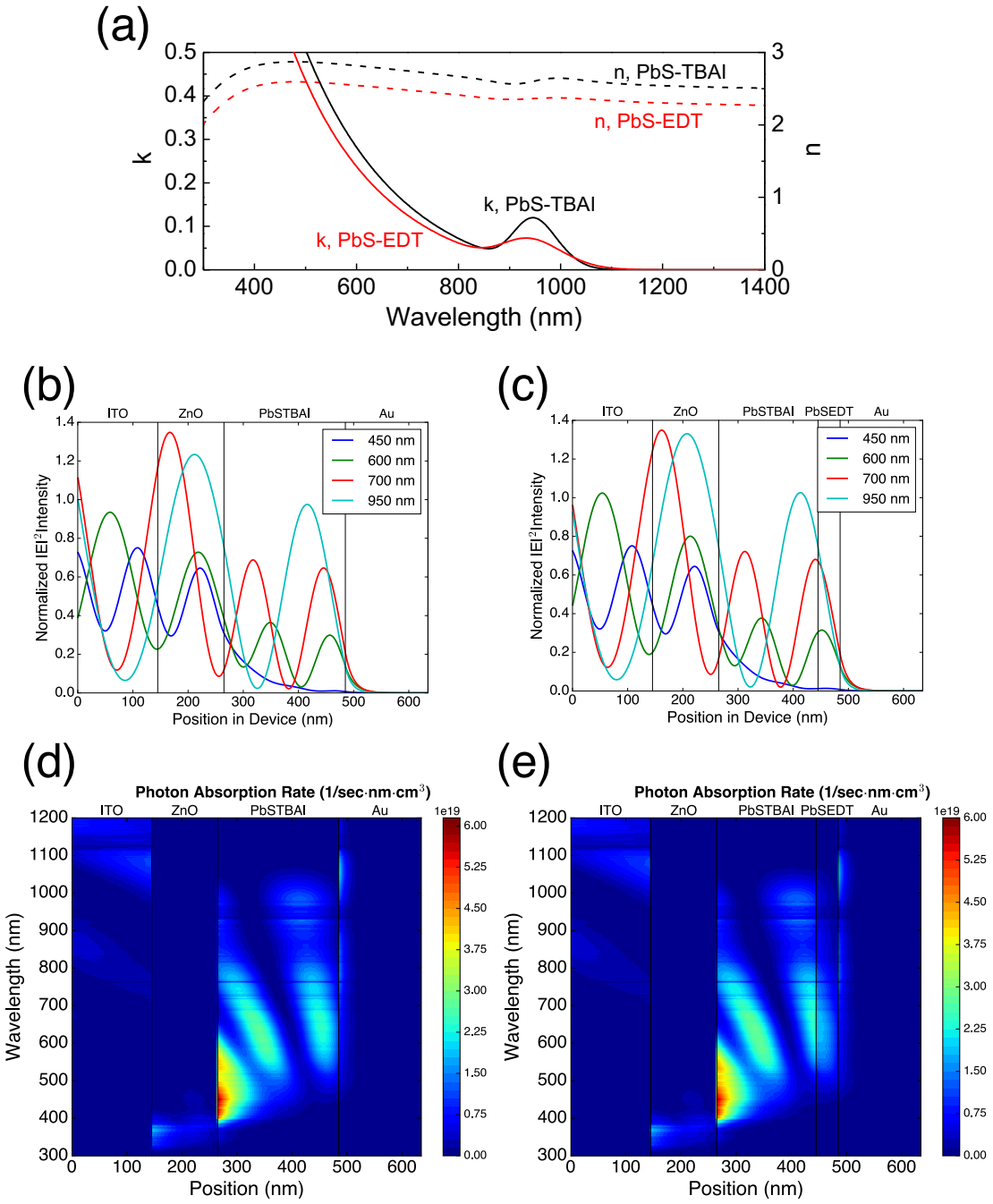

Figure 3.12 Optical modeling results. (a) The complex refractive indices of PbS-TBAI and PbS-EDT films as determined by ellipsometry. (b) and (c) Modeled electric filed intensity in the devices for four selected wavelengths. (d) and (e) Modeled photon absorption rate the under 1-sun AM1.5 illumination. (b) and (d) PbS-TBAI-only device; (c) and (e) PbS-TBAI/PbS-EDT device. The horizontal stripes are due to the dips in the AM1.5G solar spectrum (O_2 and H_2O absorption).

3.6 Verifying the Bi-Layer Structure

3.6.1 Valence Band Features

In section 3.4.2, we have shown that samples with PbS-EDT show two peaks in the UPS spectra (~3.8 eV and ~5.8 eV; Figure 3.7). These features distinguish PbS-EDT from PbS-TBAI. As another control experiment, we compare the UPS spectra of PbS-TBAI film and PbS-TBAI film soaked in EDT solution (Figure 3.13). Soaking the PbS-TBAI film in EDT solution without depositing a new PbS-EDT layer does not change the work function significantly but slightly decreases the valence band offset ($E_F - E_V$) from 0.82 eV to 0.75 eV. Therefore, simply soaking the PbS-TBAI film in EDT solution is not enough to give rise to a significant conduction band offset (valence band offset) that can block electron flow (facilitate hole extraction). Furthermore, the distinct peaks in the valence band of PbS-EDT (~3.8 eV and ~5.8 eV; Figure 3.7) do not appear in the EDT-soaked PbS-TBAI film, suggesting that soaking PbS-TBAI films in EDT solution cannot change it into PbS-EDT.

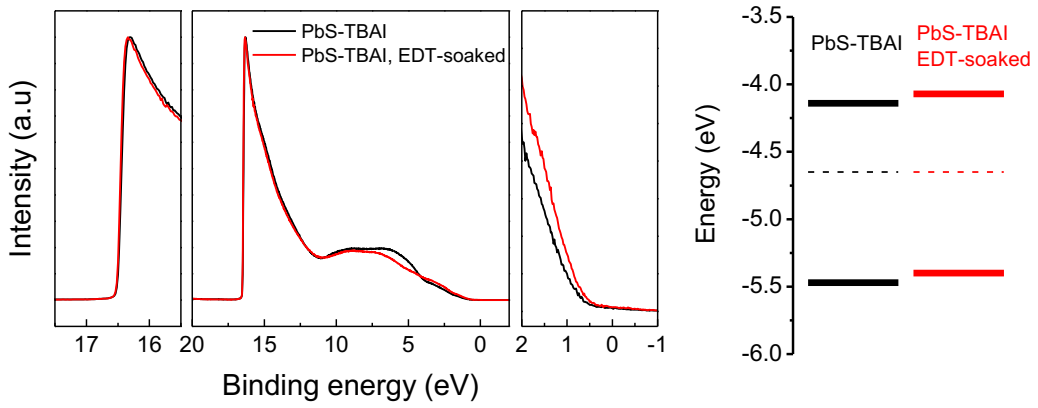

Figure 3.13 UPS spectra of a PbS-TBAI film and a PbS-TBAI film soaked in EDT solution without depositing a new PbS-EDT layer. The right figure shows the corresponding band positions with respect to vacuum.

3.6.2 Elemental Depth Profiling

X-ray Photoelectron Spectroscopy (XPS) depth profiling is used to probe the elemental compositions in the PbS-TBAI and PbS-TBAI/PbS-EDT films (Figure 3.14). The XPS depth profiling data confirm the presence of iodine (I-$3d_{2/5}$) in both films. The signal from iodine is fairly constant throughout the PbS-TBAI film (lower panel in Figure 3.14a). On the contrary, in the PbS-TBAI/PbS-EDT film, the intensity of iodine signal increases with sputtering time in the first 15 minutes (transition from PbS-EDT to PbS-TBAI layer; lower panel in Figure 3.14b) and then remains almost constant afterwards (in the PbS-TBAI layer). The evolution of the integrated intensity of the signals from Pb-4f and I-$3d_{2/5}$ as a function of sputtering time is plotted in Figure 3.14c. These data confirm the PbS-TBAI/PbS-EDT bi-layer structure in the photovoltaic devices.

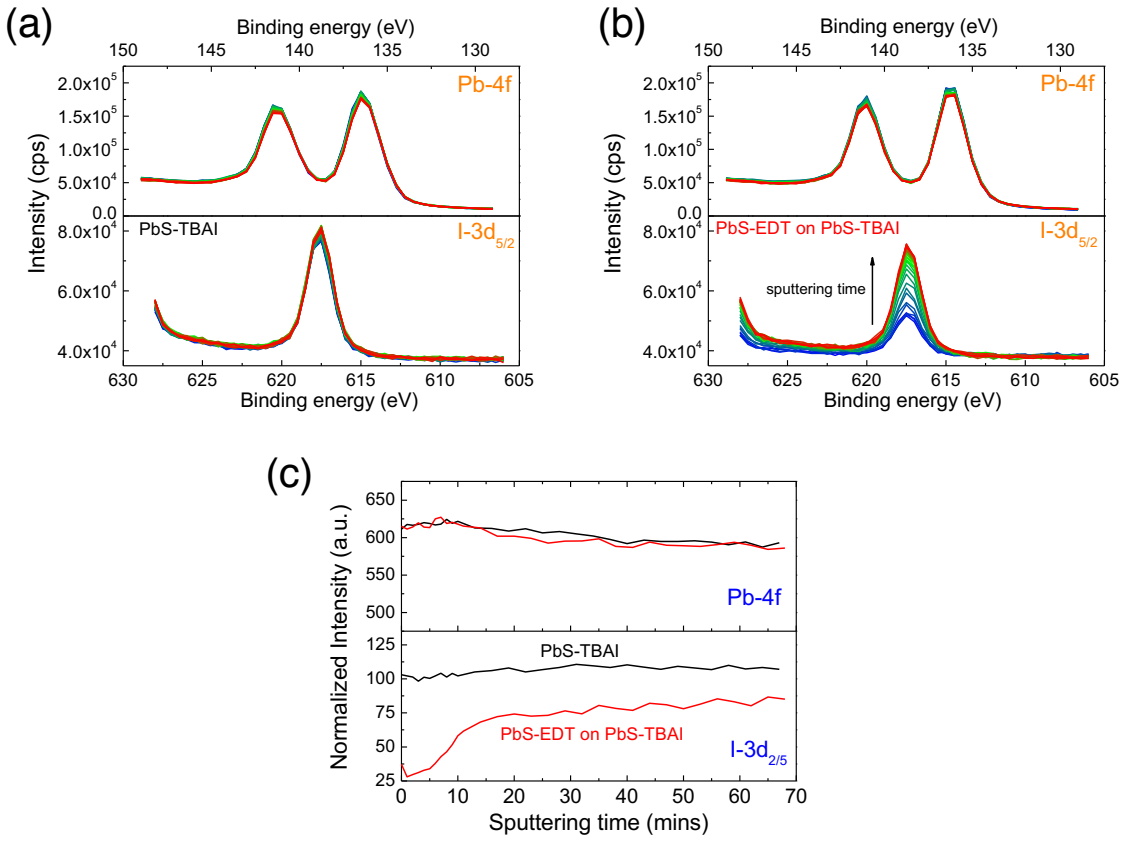

Figure 3.14 XPS depth profiling. (a) and (b), the XPS raw data showing the evolution of the signals from Pb-4f and I-3d$_{2/5}$ at different sputtering time. (a) PbS-TBAI; (b) PbS-EDT on PbS-TBAI. (c) The evolution of the integrated intensity of the signal from Pb-4f and I-3d$_{2/5}$ as a function of sputtering time. The intensities shown in this plot were calculated by integrating the signals after background subtraction and the relative intensity of each species has been normalized to their relative sensitivity factors. All calculations were done with the XPS software MultiPak.

3.7 Device Stability

3.7.1 Ligand Effects

The ligands on the surface of QDs can affect the stability of the QD films. We find that iodine passivated PbS QDs (PbS-TBAI) exhibit superior air stability compared to PbS QDs passivated with organic ligands such as PbS-EDT (Figure 3.15a). The absorption spectra of the PbS-TBAI film shows no apparent change with respect to air-storage time, indicating good air-stability of iodine passivated PbS QDs. The absorption spectra of the PbS-EDT film show a monotonic decrease in intensity and blue shift with air storage time as a result of oxidation.

The oxidation of the organic-ligand-passivated PbS QDs results in the decreasing J_{SC} and the increasing V_{OC} with air-exposure time in the PbS-EDT-only devices (Device E, Figure 3.16). It can in part explain the degradation mechanisms in previously reported QD solar cells employing organic ligands [34, 68]. However, oxidation alone may not be enough to explain the degradation mechanisms in our devices based on PbS-TBAI or PbS-TBAI/PbS-EDT.

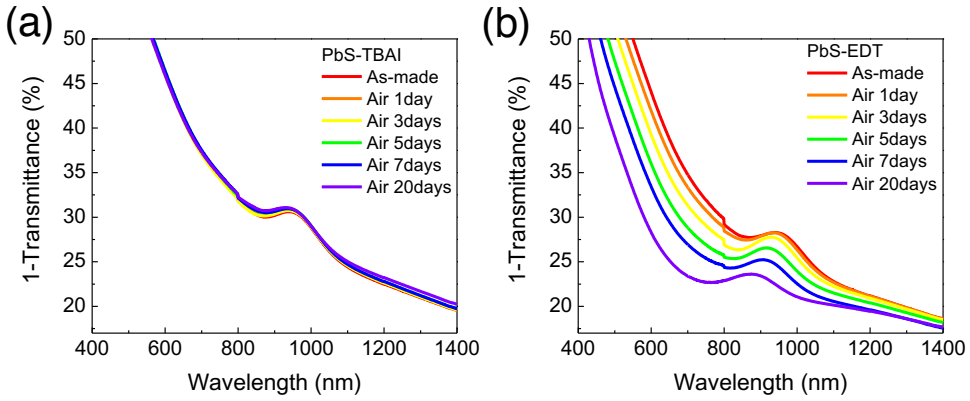

Figure 3.15 Evolution of absorption spectra of PbS thin films (2 layers) with air storage time. (a) PbS-TBAI film (b) PbS-EDT film. The discontinuity at 800nm is an artifact resulting from detector changeover.

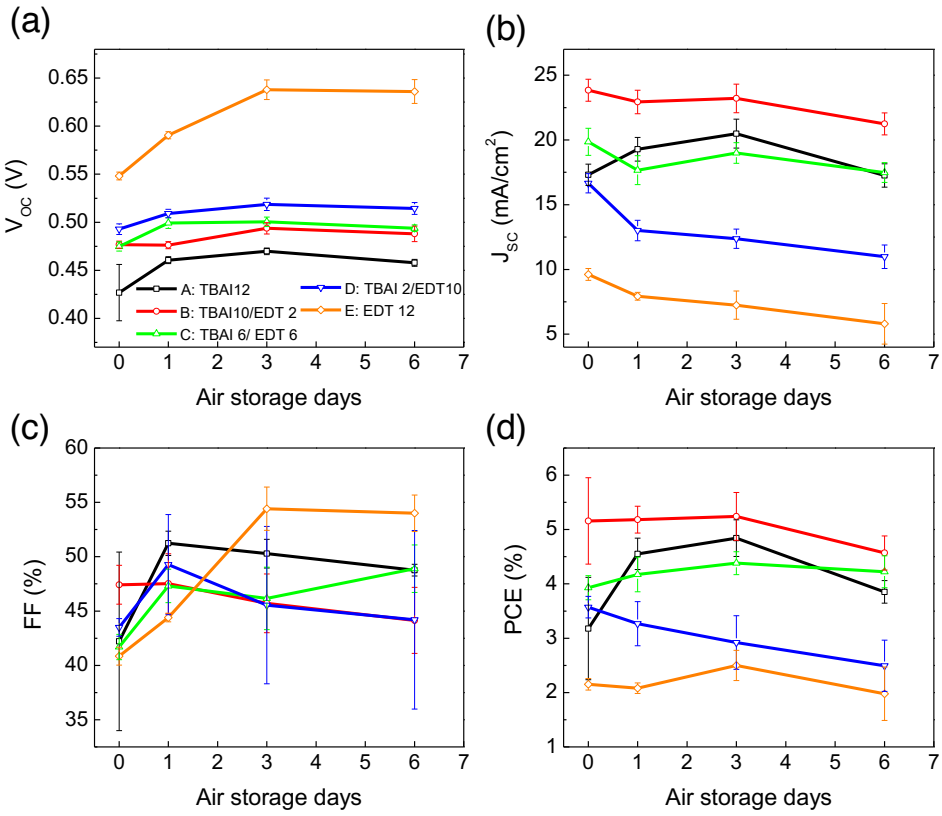

Figure 3.16 Evolution of solar cell parameters in the devices described in section 3.3.2, Figure 3.5. The device consist of different number of PbS-TBAI and PbS-EDT layers. The anode materials are MoO_3/Al.

3.7.2 MoO_3 Anode Interlayer

The stability of devices based on PbS-TBAI is found to depend to a greater extent on the interface and band alignment between the QDs and anodes than on the bulk QD layer itself. Figure 3.17 compares the evolution of solar cell performance parameters with air storage time in devices with Au and MoO_3/Au anodes, where the MoO_3 is the commonly used hole-extraction layer in PbS-based and other organic photovoltaic devices [36, 50, 73, 74]. Both PbS-TBAI and PbS-TBAI/PbS-EDT devices with Au anodes show stable performance compared to their counterparts with MoO_3/Au anodes. In contrast, devices with MoO_3/Au anodes developed S-shape J–V characteristics after air-exposure (Figure 3.18),

consistent with the development of a Schottky barrier at the anode [36, 50, 59]. This effect significantly reduces the *FF* and device performance, limiting air stability.

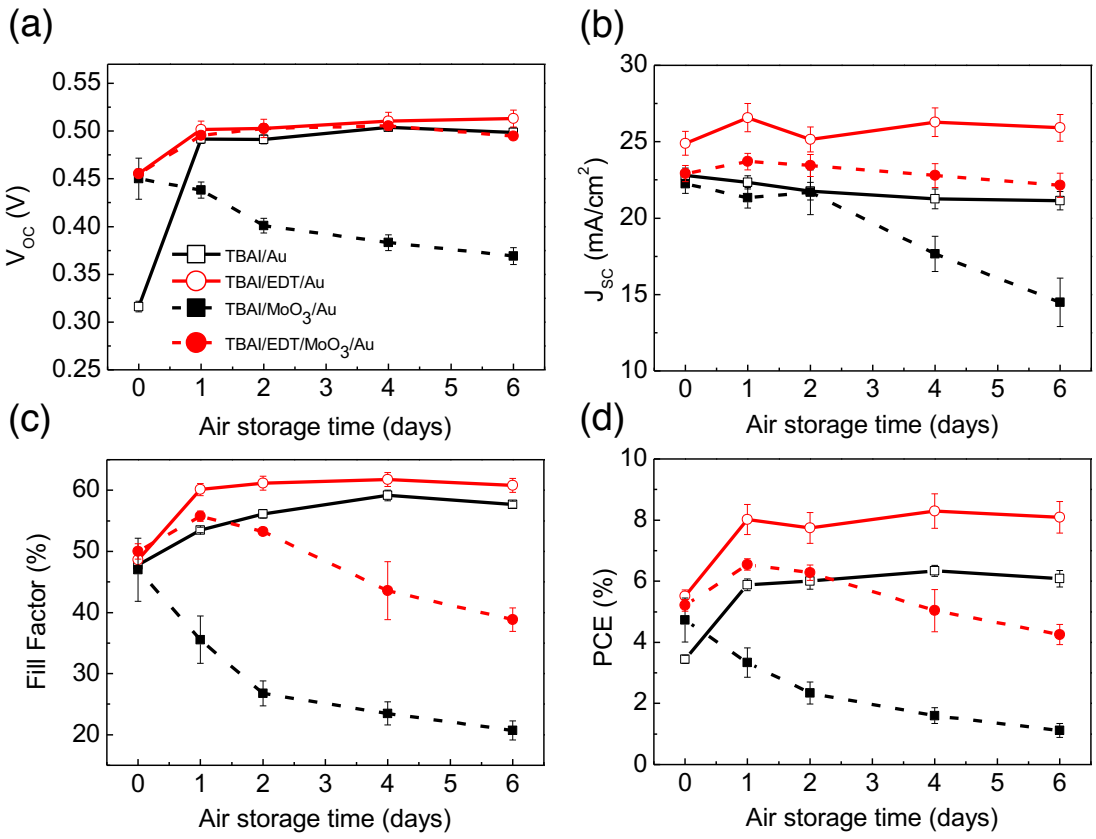

Figure 3.17 Evolution of photovoltaic parameters with air storage time in devices with Au and MoO_3/Au anodes. (a) V_{OC}; (b) J_{SC}; (c) *FF*; (d) power conversion efficiency (*PCE*). Measurements were performed in a nitrogen-filled glovebox. Day 0 denotes measurements performed after anode evaporation in vacuum. Between each measurement, the unencapsulated devices were stored in air without any humidity control. The average (symbols) and standard deviation (error bars) were calculated based on a sample of between 6 and 9 devices on the same substrate.

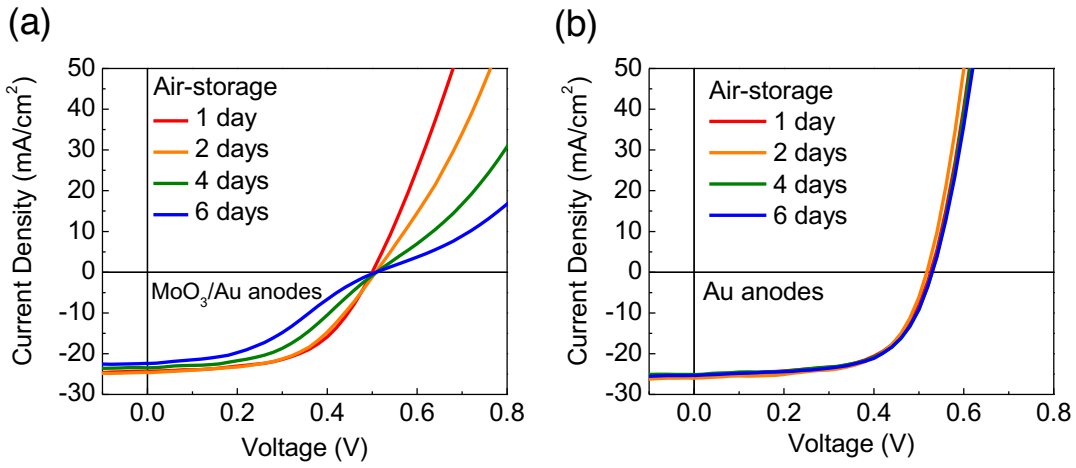

Figure 3.18 (a) Development of S-shape J–V characteristics in a PbS-TBAI/PbS-EDT device with MoO_3/Au anode after air-exposure. (b) J–V characteristics of a PbS-TBAI/PbS-EDT device with Au showing stable performance.

The mechanism through which MoO_3 acts as the hole-extraction layer is the electron transfer from its deep-lying conduction band or from gap states to the active layer [36, 50, 74]. However, the positions of these states strongly depend on the stoichiometry, environment, and deposition conditions [74, 75]. It has been shown that briefly exposing MoO_3 film deposited under vacuum to oxygen can decrease its work function by more than 1 eV to 5.5 eV [76]. Exposing MoO_3 to humid air can decrease its work function even further [77]. The S-shaped J–V characteristics in devices with a MoO_3 anode are most likely due to unfavorable band alignment between PbS and air-exposed MoO_3. We note that the air-exposure time in which this effect becomes significant varies from batch to batch of fabricated devices as a result of uncontrolled humidity in ambient storage conditions. For example, the degradation rates of the devices with a MoO_3 interlayer shown in Figure 3.16 and Figure 3.17 are different. The solar cell parameters of devices on the same substrate also show a high standard deviation. In contrast, the performance of devices without a MoO_3 interfacial layer remains

unchanged, implying that the PbS-TBAI absorber layers are functionally insensitive to oxygen and moisture during storage.

We also note that devices generally show an initial increase in V_{OC} and FF after air-exposure regardless of the active layer (PbS-TBAI, PbS-EDT, or PbS-TBAI/PbS-EDT) and anode materials (MoO_3/Al, MoO_3/Au, or Au). The ZnO/PbS films are fabricated and stored in air overnight before being transferred to a glovebox for anode deposition. The performance increases during the first hour of air-exposure after evaporation of the metal electrodes (Figure 3.19). Therefore, further oxidation of the PbS QDs is unlikely to explain the performance enhancement. We speculate that it is due to the change in PbS surface states at the PbS/anode interfaces during anode deposition under high vacuum. The origin of this initial increase in performance as a result of short air exposure is still under investigation.

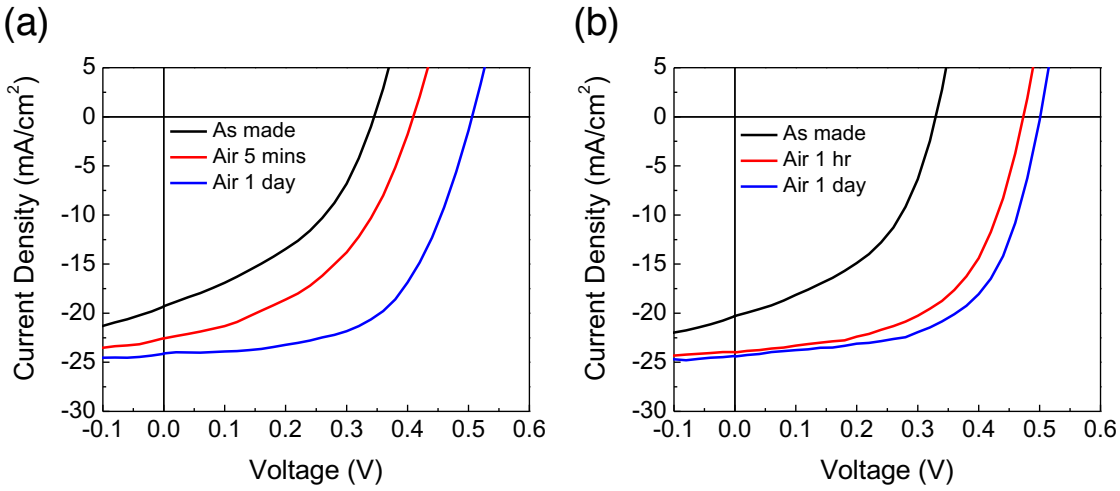

Figure 3.19 Examples of the initial increase of device performance after short air-exposure time after evaporation of the metal electrodes. The device structure is ITO/ZnO/PbS-TBAI/PbS-EDT/Au. (a) and (b) were fabricated in the same conditions but on different substrates. The devices were fabricated and stored in air overnight before anode deposition under vacuum. The air-exposure time shown here represents further air-exposure time after anode evaporation under vacuum.

3.8 Long-Term Stability and Certified Efficiencies

The devices with Au anodes not only exhibit higher performance (Figure 3.20) but also excellent long-term storage stability in air for over 150 days without any encapsulation (Figure 3.21a). During the course of the stability assessment, devices are stored in air in the dark without humidity control but with some exposure to ambient light during sample transfer to the glovebox for testing. Devices have also been tested in air (Figure 3.22) and do not show any degradation in performance after testing in air.

An unencapsulated device was sent to an accredited laboratory (Newport Corp.) after 37 days of air-storage. This device tested in air under standard AM1.5G condition shows a power conversion efficiency of 8.55±0.18% (Figure 3.21b, and Table 3-1; certification report in Appendix G), which represents the highest certified efficiency for colloidal QD photovoltaic devices at the time of the publication of this work. To the best of our knowledge, it is also the highest certified efficiency for any room-temperature solution-processed solar cell at the time of publication. Another device certified after 131 days of air-storage shows a comparable efficiency of 8.19±0.17% and the highest *FF* (66.7%) in QD solar cells at the time of the publication of this work (Appendix G).

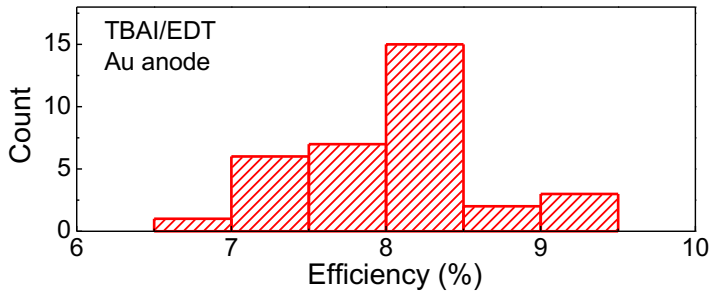

Figure 3.20 Histograms of power conversion efficiency of PbS-TBAI/PbS-EDT devices with Au anodes. The histogram shows the efficiency of more than 30 devices with Au anodes on different substrates. Unlike the devices with MoO_3 anodes whose air-stability vary due to the uncontrolled ambient humidity, all of the devices with Au anode exhibit excellent air stability.

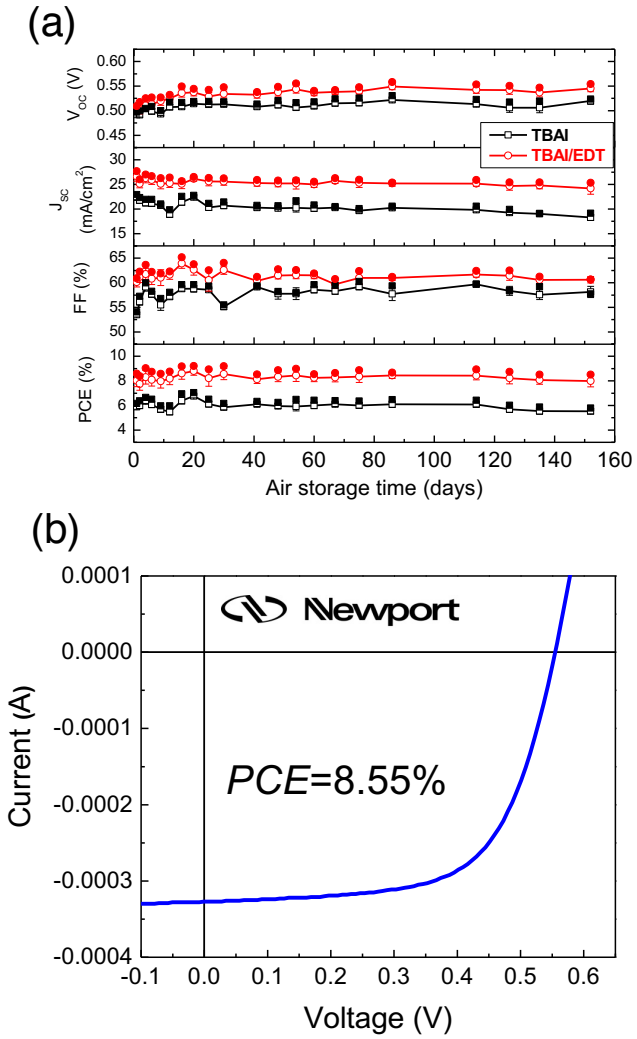

Figure 3.21 Long-term stability assessment of unencapsulated devices with Au anodes. (a) Evolution of photovoltaic parameters of PbS-TBAI (black) and PbS-TBAI/PbS-EDT(red) devices. Open symbols represent the average values and solid symbols represent the values for the best-performing device. (b) Device performance of a PbS-TBAI/PbS-EDT device certified by an accredited laboratory after 37 days of air-storage.

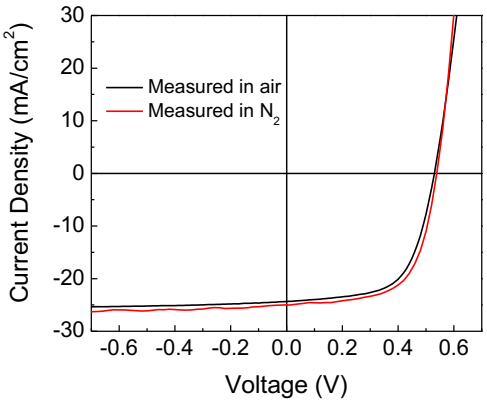

Figure 3.22 J–V characteristics of an unencapsulated PbS-TBAI/PbS-EDT device with Au anode measured in air and under inert N_2-atmosphere. No significant difference in performance was found when the device was measured in air. The slight difference is attributed to the different solar simulators used for each measurement and other experimental uncertainties.

3.9 Summary

In summary, we have demonstrated high-performance quantum dot solar cell through the engineering of band alignment at QD/QD and QD/anode interfaces. These solar cells are processed at room temperature and in air. Furthermore, they exhibit excellent air-storage stability. Our results indicate that (i) using inorganic-ligand-passivated QDs as the light-absorbing layer and (ii) removal of the MoO_3 interfacial layer are essential to achieving air-stability. Compared to other solution-processed solar cells, the present limiting factor of our device is the relatively low V_{OC}, where qV_{OC} is less than half of the optical bandgap. We suspect that elucidating the origin of the low V_{OC}, optimizing combinations of ligands and QD sizes, and further improving surface passivation via solution-phase treatments will result in continued efficiency improvements. The simplicity of the room temperature fabrication processes in ambient conditions and the robustness of the devices to ambient conditions provide advantages compared to other solution-processed solar cells. Greater understanding of the QD optoelectronic properties and further progress in materials development could lead to a generation of air-stable, solution-processable QD based solar cells.

3.10 Experimental Methods

3.10.1 Synthesis of Colloidal PbS QDs

The synthesis of oleic-acid-capped PbS QD with a first absorption peak at λ=901 nm was adapted from the literature [37, 58]. Lead acetate (11.38 g) was dissolved in 21 mL of oleic acid and 300 mL of 1-octadecene at 100 °C. The solution was degased overnight and then heated to 150 °C under nitrogen. The sulfur precursor was prepared separately by mixing 3.15 mL of hexamethyldisilathiane and 150 mL of 1-octadecene. The reaction was initiated by rapid injection of the sulfur precursor into the lead precursor solution. After synthesis, the solution was transferred into a nitrogen-filled glovebox. QDs were purified by adding a mixture of methanol and butanol followed by centrifugation. The extracted QDs were re-dispersed in hexane and stored in the glovebox. For device fabrication, PbS QDs were further precipitated twice with a mixture of butanol/ethanol and acetone, respectively, and then re-dispersed in octane (50 mg/ml).

3.10.2 Synthesis of ZnO Nanoparticles

ZnO nanoparticles were synthesized according to the literature [78]. Zinc acetate dihydrate (2.95 g) was dissolved in 125 mL of methanol at 60 °C. Potassium hydroxide (1.48 g) was dissolved in 65 mL of methanol. The potassium hydroxide solution was slowly added to the zinc acetate solution and the solution was kept stirring at 60 °C for 2.5 hours. ZnO nanocrystals were extracted by centrifugation and then washed twice by methanol followed by centrifugation. Finally, 10 ml of chloroform was added to the precipitates and the solution was filtered with a 0.45 μm filter.

3.10.3 Device Fabrication

Patterned ITO substrates (Thin Film Device Inc.) were cleaned with solvents and then treated with oxygen-plasma. ZnO layers (120nm) were fabricated by spin-coating a solution of ZnO nanoparticles onto ITO substrates. PbS QD

layers were fabricated by layer-by-layer spin-coating. For each layer, ~10 μL of PbS solution was spin-cast onto the substrate at 2500 rpm for 15 s. A TBAI solution (10mg/ml in methanol) was then applied to the substrate for 30 s followed by three rinse-spin steps with methanol. For PbS-EDT layers, an EDT solution (0.02 vol % in acetonitrile) and acetonitrile were used. All the spin-coating steps were performed under ambient condition and room light at room temperature. The thickness of each PbS-TBAI and PbS-EDT layer is about 18 nm and 23 nm, respectively, as determined by a profilometer (Veeco Dektak 6M). The films were stored in air overnight and then transferred to a nitrogen-filled glovebox for electrode evaporation. MoO_3 (Alfa) (25 nm thick), Al or Au electrode (100 nm thick) were thermally evaporated onto the films through shadow masks at a base pressure 10^{-6} mbar. The nominal device areas are defined by the overlap of the anode and cathode to be 1.24 mm^2. Larger-area devices (5.44 mm^2) have also been fabricated and show similar performance (Figure 3.23). For certification of the larger area device, a 3 mm^2 mask was attached to the device to define the device area.

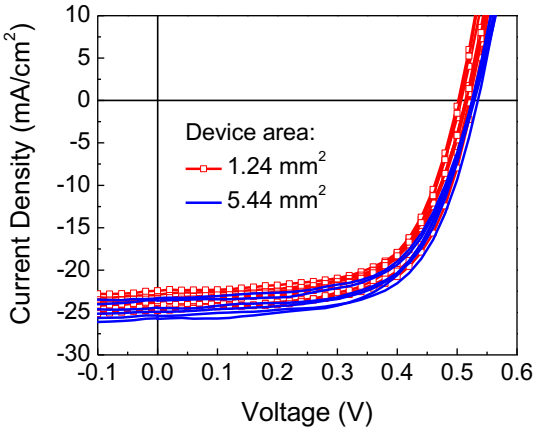

Figure 3.23 *J–V* characteristics of devices with different device areas. To test the scalability and reduce the experimental error in determining device area, we fabricated devices with a device area of 5.44 mm^2, ~4 times larger than our typical devices (1.24 mm^2). The figure plots the *J–V* curves of nine devices with 1.24 mm^2 and six devices with 5.44 mm^2 area. Devices with a larger device area show similar performance.

3.10.4 Device Characterization

Current-voltage characteristics were recorded by using a Keithley 2636A source-meter under simulated solar light illuminations (1-Sun, 100 mW/cm^2) generated by a Newport 96000 solar simulator equipped with an AM1.5G filter. The light intensity was calibrated with a Newport 91150V reference cell before each measurement. The error in efficiency measurements is estimated to be below 7%. EQE measurements were conducted under chopped monochromatic lights from an optical fiber in an underfilled geometry without bias illumination. The light source was provided by coupling the white light from a xenon lamp (Thermo Oriel 66921) through a monochromator into the optical fiber and the photocurrent was recorded by using a lock-in amplifier (Stanford Research System SR830). Both current-voltage and EQE measurements were performed under an inert-atmosphere unless stated otherwise. Devices were stored in ambient air between each measurement.

3.10.5 Ultraviolet Photoelectron Spectroscopy

PbS-TBAI and PbS-EDT samples for UPS measurements were fabricated in air by six layer-by-layer spin-coating steps to obtain ~110nm thick PbS films on glass/Cr(10nm)/Au(80nm) substrates. For PbS-EDT-thickness dependent UPS, a diluted PbS solution (10 mg/mL) was used to obtain the thinner PbS-EDT layers on PbS-TBAI films. The samples were then stored in air overnight before UPS measurements. UPS measurements were performed in an ultra high vacuum chamber (10^{-10} mbar) with a He(I) (21.2 eV) discharge lamp. Carbon tape was used to make electrical contact between the Cr/Au anode and the sample plate. A -5.0V bias was applied to the sample to accurately determine the low-kinetic energy photoelectron cut-off. Photoelectrons were collected at 0° from normal and the spectra were recorded using an electron spectrometer (Omnicron). The conduction band edge energies were calculated by adding the optical bandgap energy of 1.33 eV determined by the first exciton absorption peak in the QD thin films to the

valence band edge energies. The E_F - E_V values have an error bar of $\pm$0.02 eV resulting from curve fitting.

3.10.6 Optical Modeling

The complex refractive indices (n and k) of PbS QD films were extracted by fitting variable-angle spectroscopic ellipsometry (VASE) data. Reflection ellipsometry measurements were performed in air with a Woollam V-VASE equipped with an AutoRetarder. No significant depolarization was observed. Optical modeling was performed using custom Python scripts based on the transfer matrix method described in Ref [79, 80].

Acknowledgements

Riley Brandt helped with the J–V measurements in air. Joel Jean measured the complex dielectric constants of PbS QD films. Prof. Tonio Buonassisi provided instrumentation for solar cell measurements in air. Prof. Marc Baldo provided instumentation for UPS measurements. Dr. Liang-Yi Chang, Dr. Darcy Wanger, Dr. Dong-Kyun Ko, Dr. Andrea Maurano, Igor Coropceanu, and Chern Chuang provided helpful discussions and technical assistance during the and the preparation of this work.

This work was supported by Samsung Advanced Institute of Technology. Part of this work made use of the MRSEC Shared Experimental Facilities at the MIT Center for Materials Science and Engineering (CMSE), supported by National Science Foundation under award number DMR-08-19762, and the MIT Laser Biomedical Research Center (LBRC) under the contract number 9-P41-EB015871-26A1 supported by the National Institute of Health.

CHAPTER 4

Radiative Sub-Bandgap States in PbS QDs

This chapter is adapted with permission from Ref [81]:
C.-H. M. Chuang, A. Maurano, R. E. Brandt, G. W. Hwang, J. Jean, T. Buonassisi, V. Bulović & M. G. Bawendi, *Nano Letters*, **15,** 3286–3294 (2015). Copyright (2015) American Chemical Society.

Part of section 4.3 is adapted with permission from [82]:
G. W. Hwang, D. Kim, J. M. Cordero, M. W. B. Wilson, C.-H. M. Chuang, J. C. Grossman, & M. G. Bawendi, *Advanced Materials*, **27**, 4481-4486 (2015). Copyright (2015) John Wiley and Sons.

In this chapter, we demonstrate the presence of radiative sub-bandgap states in PbS QD films and photovoltaic devices based on photoluminescence (PL) and electroluminescence (EL) measurements. In particular, we show evidence for the filling of these states in working devices under different operating conditions. We further discuss the possible origin of these sub-bandgap states. These sub-bandgap states are most likely the origin of the high open-circuit-voltage (V_{OC}) deficit and relatively limited carrier collection that have thus far been observed in QD solar cells, as will be discussed in Chapter 5.

4.1 Photoluminescence and Electroluminescence

Figure 4.1a shows the PL spectra of a PbS-TBAI QD/PbS-EDT QD photovoltaic device under different excitation intensities. An additional emission peak (~1460 nm) with energy ~0.23 eV lower than the band-edge emission (~1145 nm) is observed. This sub-bandgap emission shows a different power dependence from the band-edge emission. At lower excitation power, the PL spectra are dominated by the sub-bandgap states emission (Figure 4.1b), while the band-edge emission dominates at higher excitation power.

By fitting the PL intensity to power law ($PL \propto I^{\alpha}$, where I is the excitation power and α is the exponent), the exponent α is found to be 0.69 for the sub-bandgap emission and 1.48 for the band-edge emission (Figure 4.2). The spectrally-integrated total PL intensity shows nearly-linear power dependence with an exponent $\alpha = 1.03$. The excitation power dependence is consistent with a competition between two emissive species, where the free-exciton-like transitions exhibit super-linear power dependence with an exponent $1 < \alpha < 2$ while transitions involving states within the gap follow a sub-linear power dependence ($\alpha < 1$) [83]. The fact that the sub-bandgap emission has not saturated at the excitation power we used suggests that these sub-bandgap states may not be completely filled at 1-Sun intensity (The excitation power density is estimated to be ~120 mW/cm^2 at an excitation power of 2.8 mW, while the 1-Sun condition is 100 mW/cm^2).

The device also shows electroluminescence (EL). Figure 4.3 shows the EL spectra of the same device under different applied biases. The EL turn-on voltage is approximately 0.5 V, and no EL signal is detected under reverse bias. The EL spectra also show emission from both band-edge and sub-bandgap states, suggesting that injected charge carriers can fill these two states.

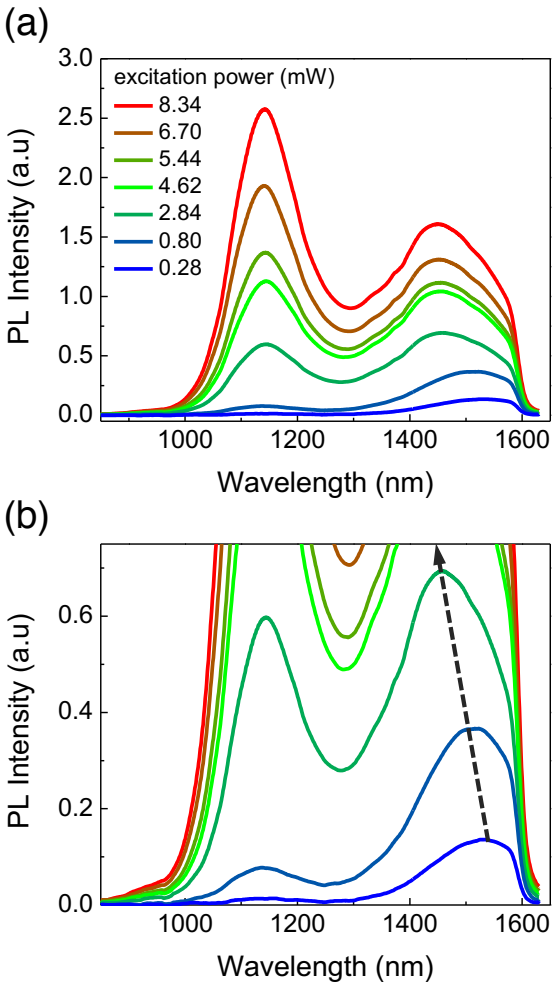

Figure 4.1 (a) PL spectra of a photovoltaic device under different excitation powers (2.84 mW corresponds to an excitation intensity of *ca.* 120 mW/cm^2). (b) magnified spectra at low excitation intensities. At low intensities, the sub-bandgap emission blue-shifts with increasing excitation power.

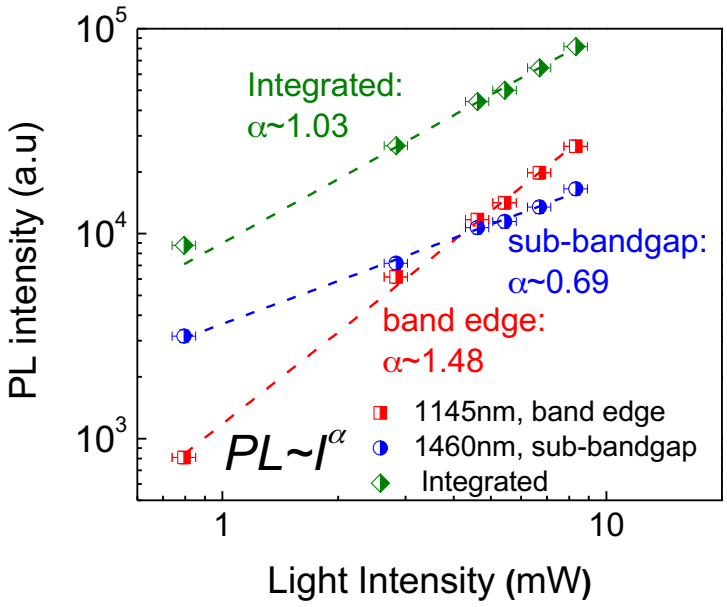

Figure 4.2 Excitation power dependence of the PL intensity for the band-edge emission peak (~1145 nm, red), the sub-bandgap emission peak (~1460 nm, blue), and the overall spectrally-integrated PL intensity (green). Dashed lines: power law fits.

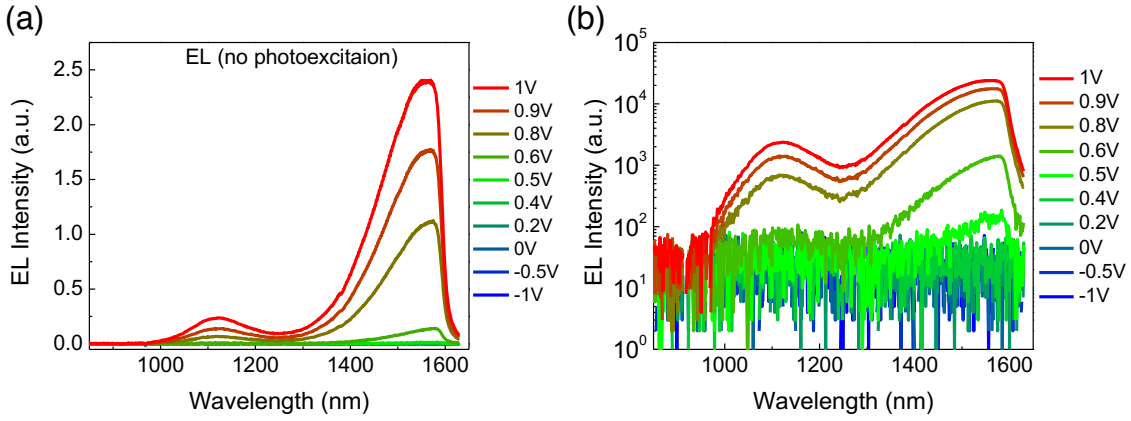

Figure 4.3 (a) EL spectra of the device shown in Figure 4.1 under different applied biases. (b) Semi-log plot. The EL turn-on voltage is approximately 0.5 V, and no EL signal is detected under reverse bias.

4.2 Filling of Sub-Bandgap States

Evidence of sub-bandgap state filling can be found in the PL spectra at different conditions. Figure 4.4a shows the total emission spectra (PL+EL) of the device under illumination and different applied biases. The contribution of the PL to the total emission is calculated by subtracting the EL spectra from the total emission (Figure 4.4c). As the applied voltage increases from reverse to forward bias, the PL intensity increases (Figure 4.4c) while the extracted photocurrent decreases monotonically (Figure 4.4b). This observation is similar to that in a recent study [84] and indicates that uncollected photogenerated carriers in part contribute to the PL in a working device. Moreover, the ratio of sub-bandgap PL to band-edge PL decreases with increasing bias (Figure 4.5), and the sub-bandgap PL slightly blueshifts (Figure 4.4d). This behavior is very similar to the power-dependent PL (Figure 4.1b) and are consistent with filling of sub-bandgap states from deeper states (lower energy states) in PbS QDs by the injected or photogenerated carriers (Figure 4.6): At higher photogenerated or injected carrier concentration (higher excitation power or higher applied voltage), shallower sub-bandgap states are filled and thus the sub-bandgap emission blueshifts and the ratio of sub-bandgap emission to band-edge emission decreases.

The EL spectra provide additional evidence of the state-filling effects. The peak position of the band-edge EL stays constant, while the position of the sub-bandgap EL shows a blueshift with increasing voltage (*i.e.*, with the amount of injected carriers; Figure 4.7). The ratio of the sub-bandgap EL to band-edge EL also decreases with increasing voltage. This behavior is identical to the power-dependent PL (Figure 4.1b) and the voltage-dependent PL (Figure 4.4c and d), confirming the sub-bandgap state filling effects.

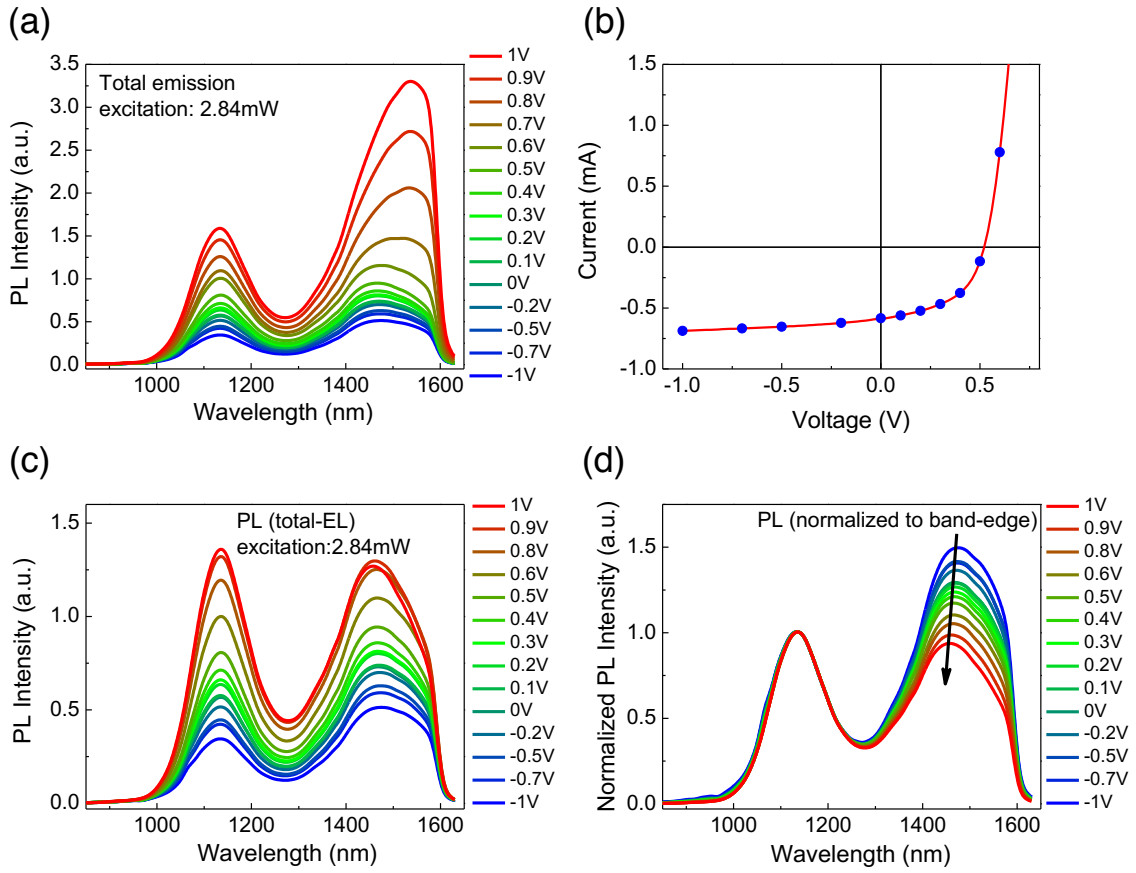

Figure 4.4 (a) Total (PL+EL) emission spectra of the device shown in Figure 4.1 under 2.84 mW laser photoexcitation with varying applied biases. The emission spectra include the contribution from both PL and EL. (b) The corresponding J–V characteristics under 2.84 mW excitation. Symbols represent some of the voltages used in (a). (c) PL contribution to total emission shown in (a). PL spectra are calculated by subtracting EL spectra from the total emission. We note that the PL signal is only from the excitation spot (~2.4 mm^2) while the EL signal is from the entire device (5.44 mm^2). (d) Normalized PL spectra under varying applied bias. The spectra are normalized to the peak band-edge emission. With increasing applied bias, the ratio of sub-bandgap PL to band-edge PL decreases and the sub-bandgap PL blue-shifts slightly, likely due to sub-bandgap state filling by injected carriers.

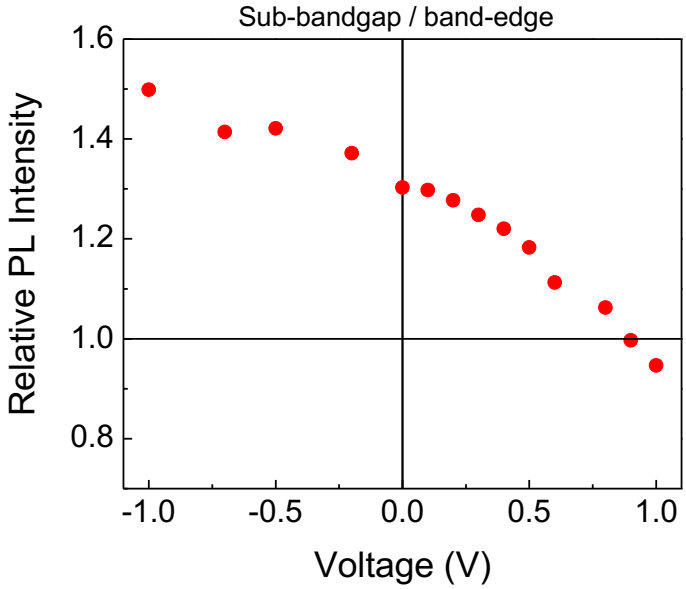

Figure 4.5 Ratio of sub-bandgap PL to bandedge PL as a function of applied voltage deduced from Figure 4.4c.

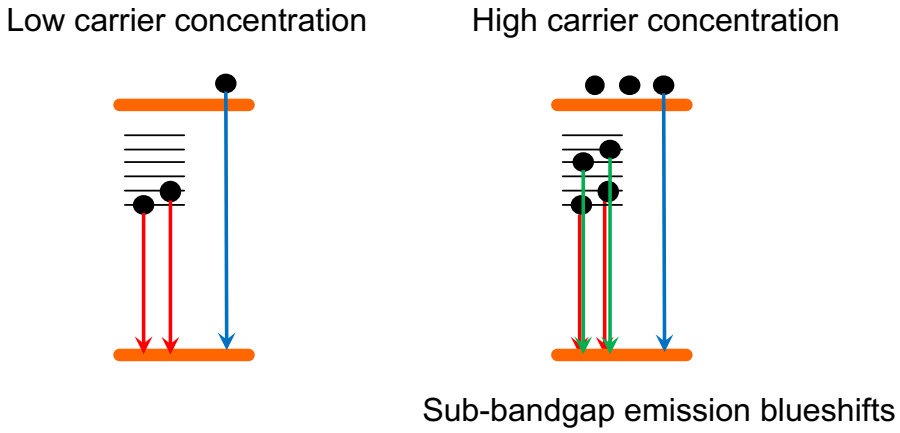

Figure 4.6 Filling of sub-bandgap states from deeper states in PbS QDs. At higher photogenerated or injected carrier concentration, more shallower sub-bandgap states are filled and thus the sub-bandgap emission blueshifts.

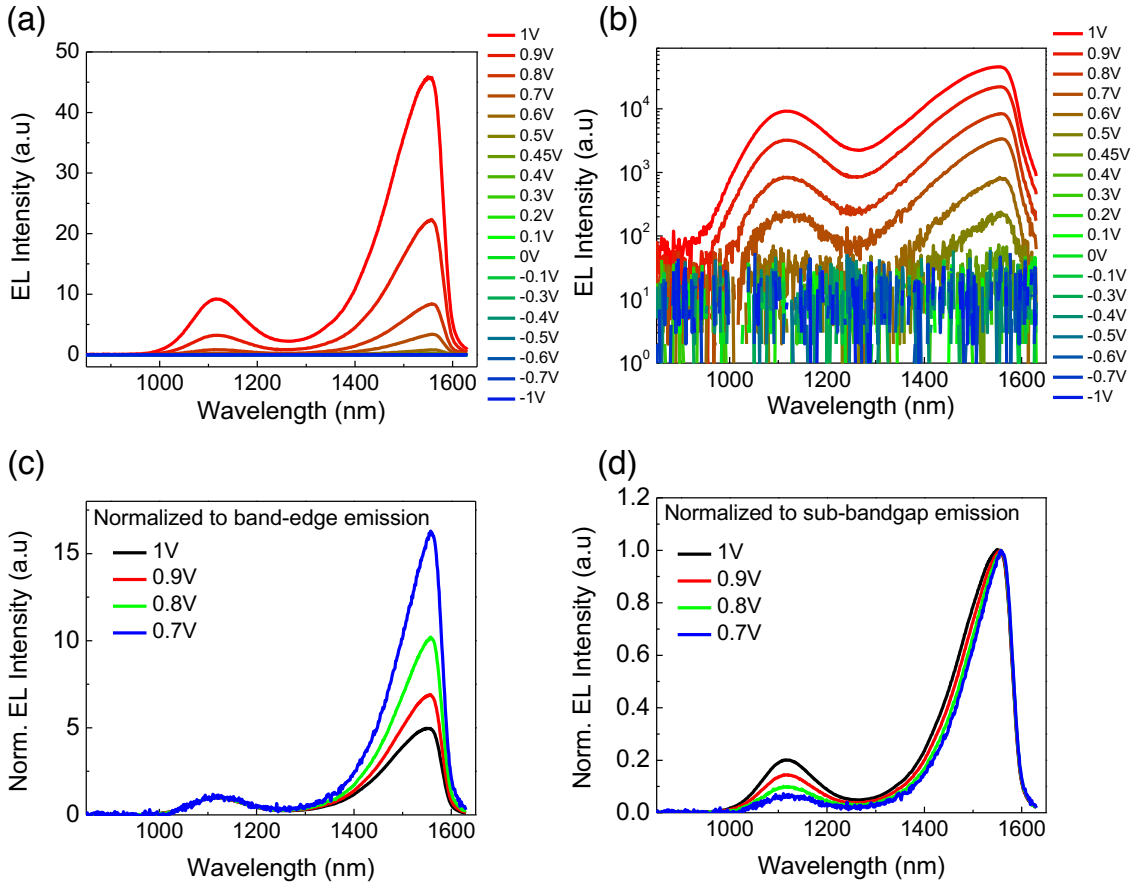

Figure 4.7 EL spectra of another PbS-TBAI QD/PbS-EDT QD device with more data points. (a) EL spectra under different applied voltages. (b) The same spectra shown in a semi-log plot. The turn-on voltage for EL is ~0.5 V. (c) The EL spectra normalized to the band-edge emission. (d) The EL spectra normalized to the sub-bandgap emission. These behaviors are consistent with sub-bandgap state filling from deeper states in PbS QDs.

4.3 Origin of Sub-Bandgap States

Although the signatures of sub-bandgap states, sometimes referred to as *mid-gap* states, *mid-gap band*, *in-gap* states, *trap* states, or *defect* states, have been observed in PbS QD thin films through different techniques [34, 85–88], the origin of these states is not well understood. In this section, we discuss the possible origin of these sub-bandgap states.

The emission spectra shown in Figure 4.1 to Figure 4.7 are for operational devices fabricated in air with a ZnO layer and metal electrodes. We verified that the sub-bandgap emission can also be observed in PbS-TBAI QD films on glass substrates that are fabricated and encapsulated in an air-free environment (Figure 4.8a). It suggests that the sub-bandgap emission originates neither from interfacial states between ZnO and PbS-TBAI QDs nor from any oxidation species in PbS-TBAI QDs.

It is widely believed that the sub-bandgap states are associated with the surface of QDs, given the high surface-to-volume ratio in QDs and the interaction between surface ligands and QDs. It is likely that these states stem from off-stoichiometry. Indeed, first-principles calculations have shown that off-stoichiometry can introduce new localized sub-bandgap states [89, 90]. We speculate that these states are mainly introduced during the solid-state ligand exchange process, especially when incomplete exchange and/or change of oxidation states (e.g. $Pb^{2+} \longrightarrow Pb^{0}$) are involved. We find that the sub-bandgap emission is significant in QD thin films after solid-state ligand exchange with some short ligands such as TBAI and EDT (Figure 4.8c). In systems with long inter-particle distances, such as PbS QDs in a solution, QD thin film with its native ligand oleic acid, PbS QD thin films after solid-state ligand exchange with octanoic acid and hexanoic acid, and QD thin films treated with methanol and acetonitrile, only band-edge emission is observed (Figure 4.8b and c). Due to low absorption cross-sections, sub-bandgap states can be difficult to distinguish from the background signal in absorption spectra. The emission, on the other hand, can be significant

because carriers originating from multiple QDs can be funneled to these sub-bandgap states (especially in systems with short interparticle distance). This phenomenon is often seen in bulk semiconductors such as ZnO, GaN, and CdS.

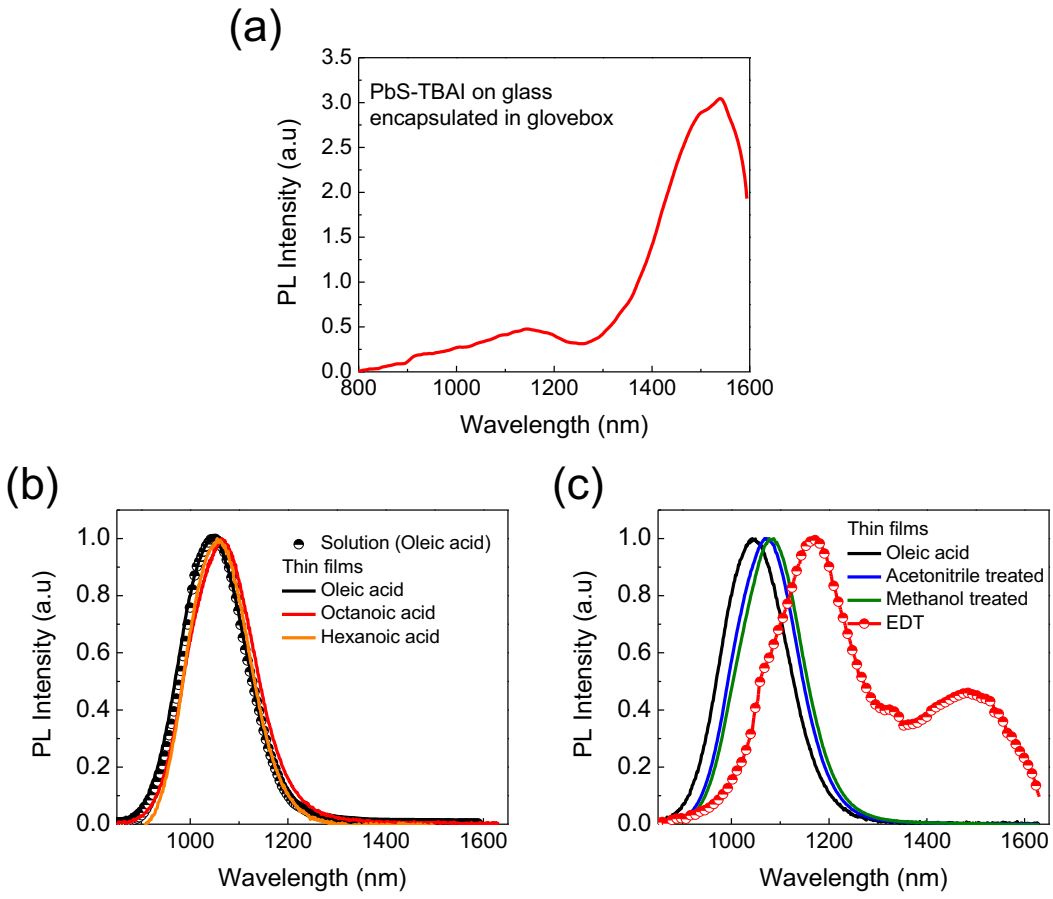

Figure 4.8 PL spectra of PbS QD thin films. (a) PL spectra of a PbS-TBAI QD film fabricated and encapsulated in an air-free environment. The presence of the sub-bandgap state emission in this sample suggests that the sub-bandgap emission originates neither from interfacial states between ZnO and PbS-TBAI QDs nor from any oxidation species in PbS-TBAI QDs. (b) PL spectra of PbS QDs in systems with long inter-particle distances: PbS QDs with the native ligand, oleic acid, in a hexane solution (symbol), a PbS QD thin film with its native ligand oleic acid (black), and PbS QD thin films after solid-state ligand exchange with octanoic acid (red) and hexanoic acid (orange). (c) PL spectra of a PbS QD thin film ligand exchanged with a short ligand EDT (red). Similar to PbS-TBAI QDs, PbS-EDT QDs also show sub-bandgap emission. Also shown are the PL spectra of PbS QD thin films treated with methanol (green) and acetonitrile (blue), the solvents used for dissolving ligands for solid-state ligand exchange.

Our recent study [82] shows that, after solid-state ligand exchange, two distinct chemical species of Pb are present in PbS QD films (Figure 4.9). The as-synthesized PbS QDs with the native oleic acid (OA) ligand show broad Pb–4f doublet peaks in the high-resolution XPS spectra, which is the combination of the signal from Pb–carboxylate (COO:Pb) and Pb–S. After ligand exchange, the signals from COO:Pb diminish while additional low binding energy peaks appear. These lower binding energy peaks correspond to metallic Pb (Pb^0, or "under-charged" Pb) and are most likely from off-stoichiometry (111) facets, which are consisting of Pb atoms only, on the surface of PbS QDs [82]. This phenomenon can be seen in PbS QDs passivated with various ligands, including inorganic ligand (TBAI) and organic ligands (EDT, 1,3-BDT). We further show that through chemical oxidation of PbS QDs with 1,4-benzoquinone (BQ), both the metallic Pb features in the XPS spectra and the sub-bandgap emission are suppressed (Figure 4.10). These experiments supports our argument that off-stoichiometry (under-charged Pb) introduced by ligand exchange may be responsible for the radiative sub-bandgap states.

We note that the sub-bandgap emission has been attributed to the presence of "electronically active impurities", lead oleate–MPA complex where MPA (3-mercaptopropionic acid) is an organic ligand used to passivate PbS QDs [87]. It was claimed that the lead oleate–MPA complex and thus sub-bandgap emission can be eliminated by using pyruvic acid to dissolve the complex. However, this explanation is unlikely to be correct, as the sub-bandgap emission can be found in PbS QDs without MPA such as iodide-passivated and EDT-passivated QDs as we have shown. In fact, pyruvic acid is also an oxidizing agent, which can achieve similar effects to that from BQ treatment [82].

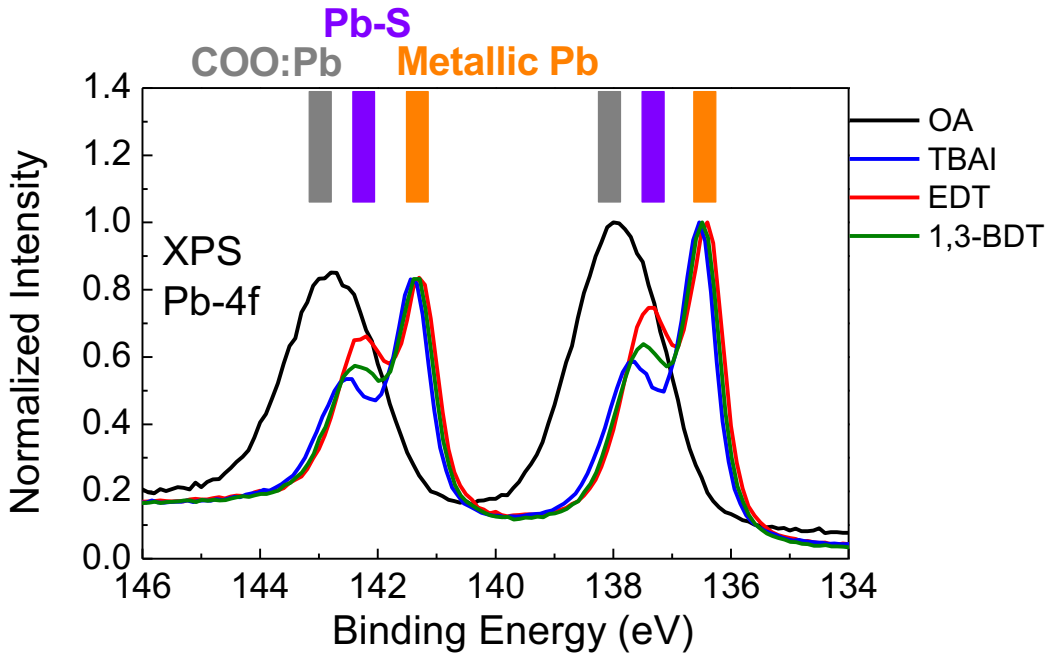

Figure 4.9 XPS result of the Pb-4f features for PbS QD thin films with different ligands. OA: oleic acid; 1,3-BDT: 1,3-benzenedithiol. The binding energies of metallic Pb, Pb–S, and COO:Pb are highlighted.

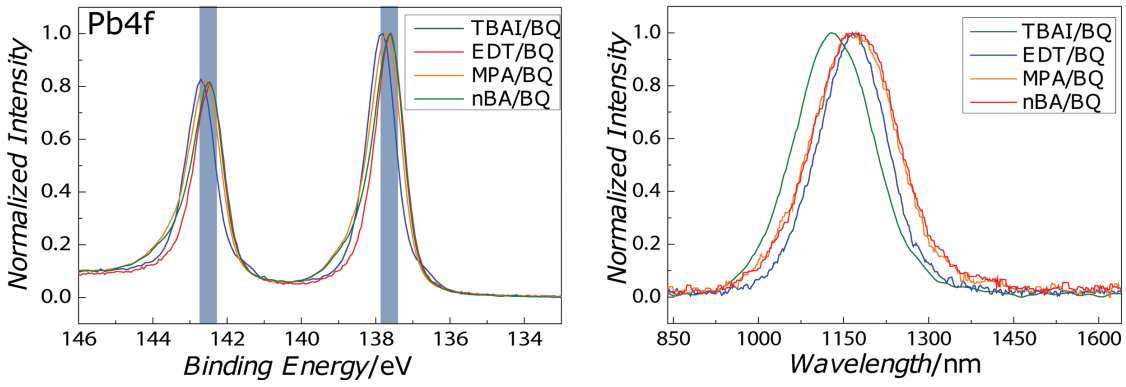

Figure 4.10 XPS (left) and PL spectra (right) of ligand-exchanged PbS QD thin films after chemical oxidation with 1,4-benzoquinone (BQ). nBA: *n*-butylamine.

4.4 Summary

The presence of radiative sub-bandgap states in PbS QD solar cells are demonstrated through PL and EL spectroscopies under different operating conditions. The blue-shift of the sub-bandgap emission with excitation power and injected carrier density indicates filling of these states from deeper states. It is found that uncollected photogenerated carriers contribute to both band-edge emission and the sub-bandgap emission. The dominance of the sub-bandgap PL at reverse bias, where photogenerated carrier collection is facilitated by the increased built-in field, suggests trapping in the sub-bandgap states as a loss mechanism.

The sub-bandgap emission can be found in PbS QD films treated with a variety of short ligands including inorganic iodide and organic molecules. The origin of these sub-bandgap states is most likely under-charged Pb atoms on the surface of QDs introduced during the solid-state ligand exchange process. As will be discussed in the following chapters, these sub-bandgap states are most likely the major cause of the voltage deficit and relatively limited carrier collection in QD solar cells. Therefore, the results presented in this chapter provide insight into improving the performance of optoelectronic devices based on QDs.

4.5 Experimental Methods

PL and EL spectra were recorded with a SpectraPro 300i spectrometer connected to liquid nitrogen cooled InGaAs detector arrays (Princeton Instruments; OMA V, 512x1 pixels). A 532 nm laser was used as the excitation source for PL. The excitation intensity was adjusted by a series of neutral density filters and measured directly with a power meter. For the PL and EL measurements on photovoltaic devices, the devices were placed in a custom-made stage and connected to a sourcemeter (Keithley 2636A). For bias-dependent emission spectra, the emission spectra in the dark (EL only) and under photoexcitation (total emission) were recorded at different applied biases. The PL was calculated by subtracting the EL from the total emission. To avoid potential charging effects, the order of the applied bias was chosen randomly. To ensure that the PL at different biases was entirely from the active area of the biased device, an underfill geometry was used. The laser was focused to a spot size (*ca.* 2.4mm^2) smaller than the total device active area (5.44mm^2). The excitation density is estimated from the spot size and the device EQE (ca. 70% at 532nm).

CHAPTER 5

Origin of the Open-Circuit Voltage Deficit in Quantum Dot Solar Cells

This chapter is adapted with permission from Ref [81]:
C.-H. M. Chuang, A. Maurano, R. E. Brandt, G. W. Hwang, J. Jean, T. Buonassisi, V. Bulović & M. G. Bawendi, *Nano Letters*, **15,** 3286–3294 (2015).

Abstract

Quantum dot photovoltaics (QDPV) offer the potential for low-cost solar cells. To develop strategies for continued improvement in QDPVs, a better understanding of the factors that limit their performance is essential. Here, we study carrier recombination processes that limit the power conversion efficiency of PbS QDPVs. In Chapter 4, we have demonstrated the presence of radiative sub-bandgap states and sub-bandgap state filling in operating devices by using photoluminescence (PL) and electroluminescence (EL) spectroscopy. These sub-bandgap states are most likely the origin of the high open-circuit-voltage (V_{OC}) deficit and relatively limited carrier collection that have thus far been observed in QDPVs. Combining these results with our perspectives on recent progress in QDPV, we conclude that eliminating sub-bandgap states in PbS QD films has the potential to show a greater gain than may be attainable by optimization of interfaces between QDs and other materials. We suggest possible future directions that could guide the design of high-performance QDPVs.

5.1 Introduction

Developing low-cost technologies for efficient solar energy harvesting has long been a goal of energy sustainability. In the past decade, solution-processed solar cells based on lead chalcogenide (PbX, X=S, Se, Te) colloidal quantum dots (QDs) have become one emerging photovoltaic (PV) technology [29] that can potentially meet this goal. Bulk lead chalcogenides have bandgaps below 0.5 eV. Owing to the quantum confinement effect, the bandgap of lead chalcogenide QDs can be tuned from approximately 0.6 eV to 1.5 eV. The unique combination of a low bandgap energy and broad tunability enables infrared photon harvesting and the development of multi-junction solar cells [61]. Among lead chalcogenide QDs, PbS has received the most attention for solar cell applications. Their inexpensive and Earth-abundant nature [39], scalable synthesis, good stability, and solution-processability make PbS QDs a promising candidate for low-cost solar cells. Indeed, the certified QDPV efficiency record has rapidly increased from 3% to >9% within 4 years, predominantly due to improvements in PbS QDPV [29, 32–36]. The feasibility of PbS QDPV on flexible plastic substrates has been successfully demonstrated [91]. Device stability has also rapidly improved, with reports of >1000 hours of operation stability [32, 92] and >150 days of air stability [35].

Despite recent advances, the power conversion efficiency of QDPV is still below the expected performance for a semiconductor with this bandgap range. One primary limitation is the large open-circuit voltage (V_{OC}) deficit (defined as E_g/q - V_{OC}, where E_g is the absorber bandgap and q is the elementary charge). This large V_{OC} deficit is often seen in QDPVs regardless of device structure and surface ligands, but its origin is not fully understood. Recently, halide-based ligands (*i.e.*, Cl^-, Br^-, I^-) have been shown to improve the stability of PbS and PbSe QDs [35, 38, 93–96]. While QDPVs made of halide-passivated QDs achieve high short-circuit current densities (J_{SC}) and efficiencies, they typically exhibit somewhat lower V_{OC} values than devices employing organic ligand-passivated QDs [33–35, 97]. This phenomenon cannot be explained in terms of the degree of surface passivation and

is not fully understood. In this work, we investigate the working mechanism of efficient PbS QD solar cells. We identify the possible origins of the large V_{OC} deficit. In particular, we show that radiative sub-bandgap likely account for both the V_{OC} deficit and the limited carrier collection. Based on these findings, future prospects for QDPV are discussed, and potential routes to improving QDPV performance are suggested.

5.2 Open-Circuit Voltage Deficit

5.2.1 Large Open-Circuit Voltage Deficit in Quantum Dot Solar Cells

The devices investigated in this work are planar heterojunction ZnO/PbS QD solar cells with an iodide-passivated PbS QD absorber layer. This layer is formed by solid-state ligand exchange with tetrabutylammonium iodide (TBAI). For some devices, a thin layer of 1,2-ethanedithiol(EDT)-passivated PbS QDs is introduced as an electron-blocking layer between the PbS-TBAI QD layer and Au electrode (Figure 5.1a). This PbS-TBAI QD/PbS-EDT QD device structure yields some of the highest efficiency QD solar cells to date. Experimental details are provided in section 5.9 and in our previous publication [35].

As shown in Figure 5.1b, the qV_{OC} (555 meV) of a certified 8.6 % device [35] is significantly lower than the absorption onset energy of a PbS-TBAI QD film. Figure 5.1c and d compare the V_{OC} deficit in QDPV with that of other leading PV technologies, with V_{OC} values corresponding to certified record-efficiency devices [98]. As the definition of bandgap differs between communities, we consider a range between two values for the PbS QD bandgap: the optical gap, conventionally defined as the first exciton absorption peak (here, 1.33 eV), and the onset of the external quantum efficiency (EQE) (1.13 eV). Given the broad exciton absorption peak in QDs, the EQE onset is preferred when comparing the measured V_{OC} with the Shockley-Queisser limit [28]. Although the V_{OC} deficit (575 mV) in QDPV is comparable to that in CdTe and CZTSSe solar cells, it is ~200mV larger than that

in single-crystalline Si solar cell with a similar bandgap ($E_g = 1.12$ eV, $V_{OC} = 740$ mV).

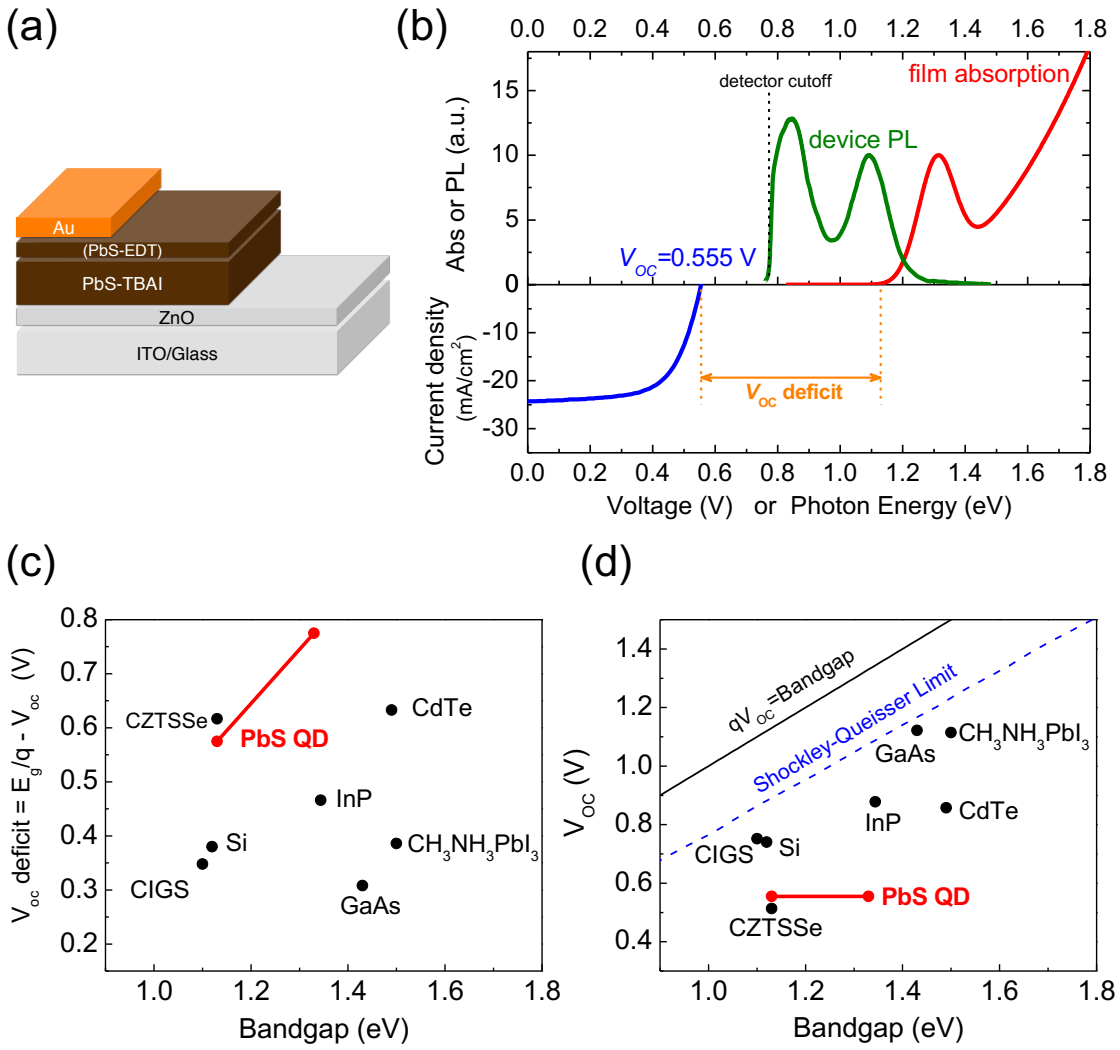

Figure 5.1 V_{OC} deficit in PbS QDPV. (a) Device structure. (b) Upper panel: absorption spectra of a PbS-TBAI QD film and photoluminescence (PL) spectra of a PbS-TBAI QD/PbS-EDT QD device. Lower panel: J-V characteristics of the certified 8.6 %-efficient QDPV ($V_{OC} = 0.555$ V) [35]. (c) The V_{OC} deficits in PbS QDPV and other common PV materials. The two bandgap values shown for PbS QDs correspond to different definitions (see text). V_{OC} values correspond to certified record-efficiency devices [98]. CIGS: $CuIn_xGa_{1-x}Se_2$; CZTSSe: $Cu_2ZnSnS_xSe_{4-x}$. (d) Comparison of the V_{OC} and the absorber bandgap of various materials. The Shockley-Queisser limit at 300 K is also shown.

5.2.2 Sources of Open-Circuit Voltage Deficit

Sources of V_{OC} deficit could be: (1) poor QD monodispersity [99], (2) insufficient photon absorption, (3) incomplete charge collection, and (4) fast carrier recombination rate.

Poor monodispersity of QDs broadens the absorption spectrum near the band-edge, whose sharpness is known to be correlated with device V_{OC} [99, 100]. However, monodispersity is unlikely to be the primary cause of the large V_{OC} deficit. Previous calculation has shown that a 50 meV Urbach energy (the exponential decay constant of the absorption coefficient near the absorption edge) reduces the V_{OC} of QDPVs to ~50% of its Shockley-Queisser limit [99]. However, the measured Urbach energy in PbS QD films by Erslev *et al.* [101] is as low as 14–20 meV. It has also been shown that intentionally incorporating 10 % of QDs with a smaller bandgap only results in 10–20 mV of reduction in V_{OC} [102]. In addition, our PbS QDs show reasonably narrow size distribution with a standard deviation of 5.8% according to the empirical equation described by Weidman *et al.*, which is an overestimated distribution due to the assumption of a delta function single particle absorption band [38]. Therefore, we conclude that monodispersity is not the primary cause of large V_{OC} deficits in QD solar cells.

Insufficient absorption and incomplete charge collection result in a low J_{SC}, which leads to a lower V_{OC} (Equation (5-1))

$$V_{OC} = \frac{nkT}{q} \ln\left(\frac{J_{SC}}{J_0} + 1\right) \tag{5-1}$$

where n is the diode ideality factor, k the Boltzmann constant, T the temperature, and J_0 the reverse saturation current density. However, insufficient absorption and incomplete charge collection are not likely primary causes of the large V_{OC} deficit, either, as V_{OC} scales logarithmically with J_{SC}. We thus focus our attention on carrier recombination mechanisms, which are dominated by junction characteristics

and the presence of sub-bandgap states in the absorber (*i.e.*, the sub-bandgap emissive states in Figure 5.1b).

5.3 Device Characteristics

5.3.1 *J*–V Characteristics

We carried out several device characterization techniques to investigate the working mechanisms of these devices. The diode ideality factor n is an indicator of the dominant recombination mechanism. By fitting the dark J–V curves with the ideal diode equation (Equation (5-2)), n is determined to be 1.8±0.1 for both PbS-TBAI QD and PbS-TBAI QD/PbS-EDT QD devices (Figure 5.2a).

$$J = J_0 \left[\exp\left(-\frac{qV}{nkT} \right) - 1 \right] \tag{5-2}$$

Alternatively, n is found to be 1.5±0.1 from the light intensity dependence of the short-circuit current density (J_{SC}) (Figure 5.2b) and V_{OC} (Figure 5.2c) according to Equation (5-1). When band-to-band recombination dominates, n is equal to 1. The ideality factor n>1 indicates that other recombination mechanisms such as trap-assisted recombination (n=2) in PbS QDs within the space-charge region (or depletion region) are involved.

The similarity in the ideality factor and dark J-V characteristics of the PbS-TBAI QD and PbS-TBAI QD/PbS-EDT QD devices suggest similar recombination mechanisms, which points to two important conclusions. First, the higher V_{OC} of the PbS-TBAI QD/PbS-EDT QD device compared to the PbS-TBAI QD device is a consequence of its higher J_{SC} under the same light intensity. This is consistent with the electron-blocking effect of the PbS-EDT QD layer, which improves the charge carrier collection efficiency (Chapter 3) [35]. Second, since the addition of the PbS-TBAI QD/PbS-EDT QD interface does not appear to affect carrier generation-recombination mechanisms, the ZnO/PbS QD heterojunction must dominate the carrier recombination processes (J_0) and thus the V_{OC}. The dominant

recombination process is thus either space-charge region recombination in PbS-TBAI QDs or interfacial recombination at the ZnO/PbS-TBAI QD interface.

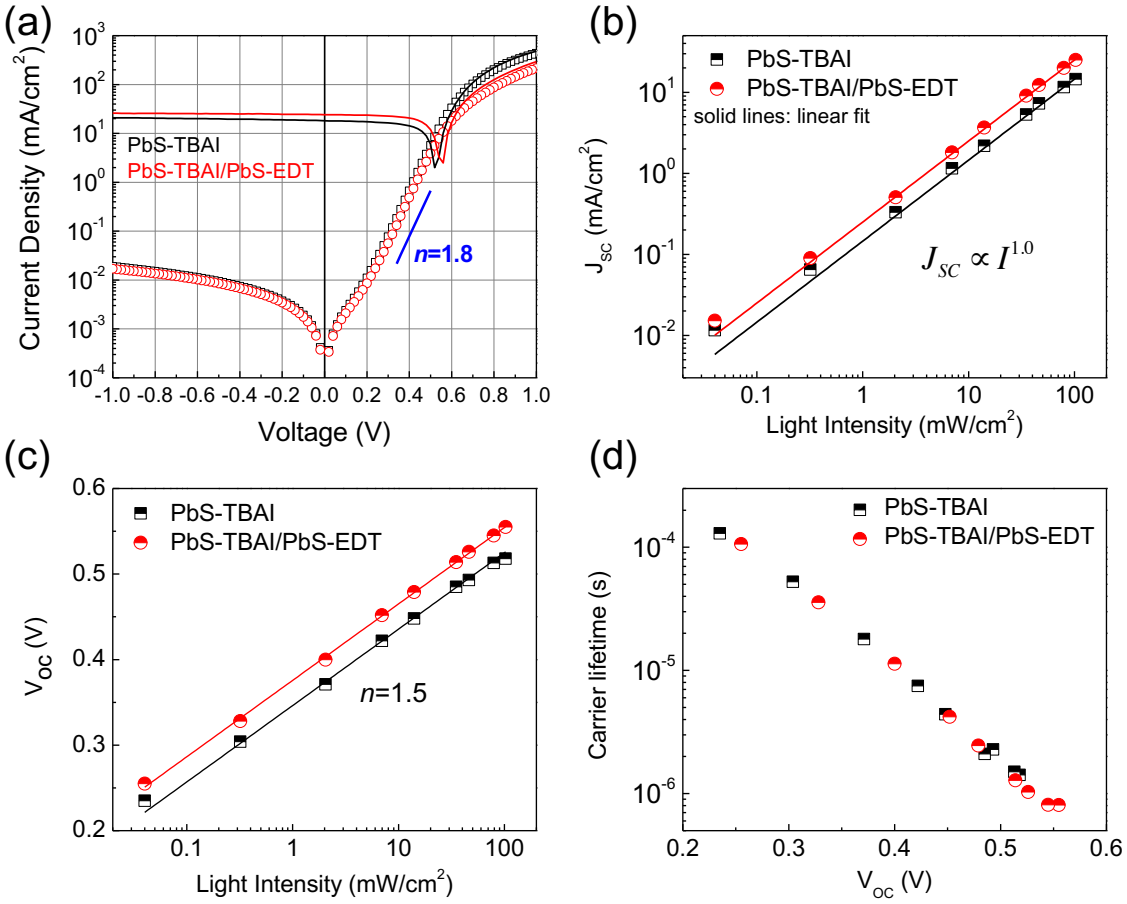

Figure 5.2 Device characteristics of PbS-TBAI QD and PbS-TBAI QD/PbS-EDT QD devices. (a) J–V characteristics of devices in the dark (open markers) and under 100mW/cm^2 AM1.5 illumination (solid lines). The straight line indicates the slope corresponding to an ideality factor n=1.8. (b) Light-intensity dependence of J_{SC}. Solid lines: linear fits. (c) Light intensity dependence of V_{OC}. Solid lines: logarithmic fits with an ideality factor n=1.5. (d) Carrier lifetime as a function of V_{OC}. Lifetimes are determined from transient photovoltage measurements with a varying steady-state white light bias to generate different V_{OC} values.

5.3.2 Carrier Lifetimes

Figure 5.2d shows a study of carrier recombination dynamics using transient photovoltage measurements at various steady-state bias light intensities. The carrier lifetimes as a function of V_{OC} for PbS-TBAI QD and PbS-TBAI QD/PbS-EDT QD devices are almost identical, further supporting similar dominant recombination mechanisms and rate constants. Zhao *et al.* [58] and Brown *et al.* [47] have shown that different PbS QD layers can alter both the carrier lifetimes and their slopes versus V_{OC}. When different recombination mechanisms are present, a longer carrier lifetime usually translates into a higher V_{OC}. In contrast, the devices studied here have identical ZnO/PbS QD heterojunctions. Under identical white light bias, the PbS-TBAI QD/PbS-EDT QD device—which exhibits a higher V_{OC}—shows a shorter carrier lifetime, due to the higher steady-state photogenerated carrier concentration (Figure 5.3a). We note that under 1-Sun illumination (100 mW/cm^2), the carrier lifetimes for PbS-TBAI QD/PbS-EDT QD and PbS-TBAI QD devices are 0.8 μs and 1.4 μs, respectively, which indicates faster recombination rates than observed in devices based on PbS-EDT QDs (2 μs; Figure 5.3b) and other organic ligand-passivated PbS QDs (2–13 μs) [47, 103]

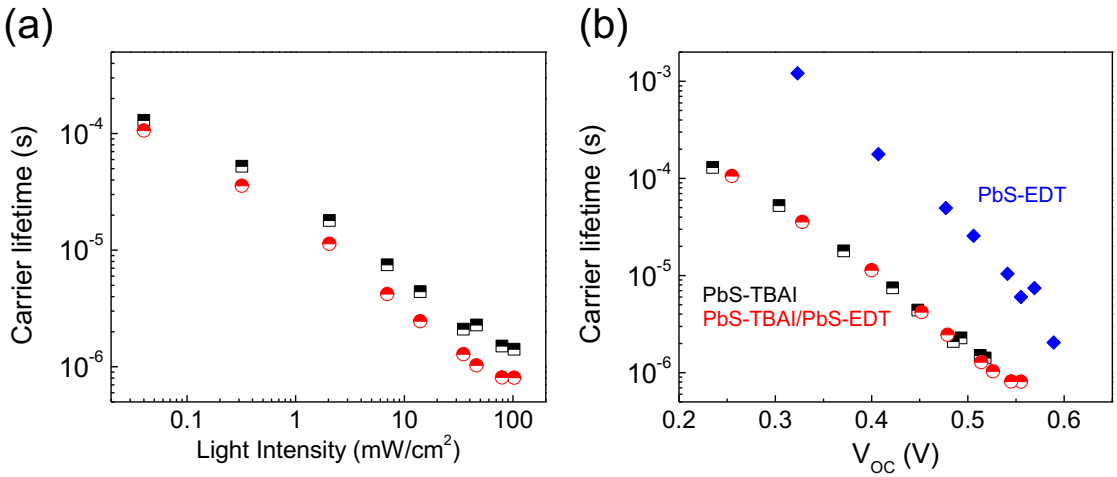

Figure 5.3 (a) Carrier lifetime as a function of light intensity. (b) Comparison of carrier lifetimes as a function of V_{OC} for devices based on iodide (TBAI)-passivated PbS QDs and organic ligand (EDT)-passivated PbS QDs. Devices based on organic ligand-passivated PbS QDs show slower recombination rates and higher V_{OC} values than halide passivated PbS QDs.

5.3.3 Temperature-Dependent *J*–*V* Characteristics

The temperature-dependent J-V characteristics provide further insight into generation–recombination processes contributing to the diode current (Figure 5.4a-c). For a single thermally activated carrier generation-recombination mechanism, J_0 can be expressed as Equation (5-3). Substitution of Equation (5-3) into Equation (5-1) yields Equation (5-4):

$$J_0 = J_{00} \exp\left(\frac{-E_a}{nkT}\right) \tag{5-3}$$

$$V_{OC} = \frac{E_a}{q} - \frac{nkT}{q} \ln\left(\frac{J_{00}}{J_{SC}}\right) \tag{5-4}$$

where E_a is the activation energy, and J_{00} the pre-factor [104]. An activation energy equal to the absorber bandgap implies the dominance of bulk generation-recombination in the absorber. An activation energy smaller than the bandgap

often implies the significance of interfacial recombination [104]. In the high-temperature range where n, J_{00}, and J_{SC} are nearly temperature-independent, E_a can be determined by extrapolating V_{OC} to 0 K. As shown in Figure 5.4a, for a PbS-TBAI QD/PbS-EDT QD device, E_a is determined to be 0.92±0.01 eV for all three illumination intensities (The J–V characteristics of the device under illumination are shown in Figure 5.5b). In the range where n, J_{00}, and J_{SC} show temperature dependence, E_a can be determined from Equation (5-5), a re-organized form of Equation (5-3) [104].

$$n\ln(J_0) = -\frac{E_a}{kT} + n\ln(J_{00}) \tag{5-5}$$

From Equation (5-5) and the dark J–V curves at different temperatures (Figure 5.4b), E_a is determined to be 0.94±0.01 eV (Figure 5.4d), in good agreement with the value extracted from the T–V_{OC} plot (Figure 5.4a). The PbS-TBAI QD device shows similar behavior with an activation energy of 0.96±0.01 eV (Figure 5.4d, Figure 5.5a and Figure 5.6).

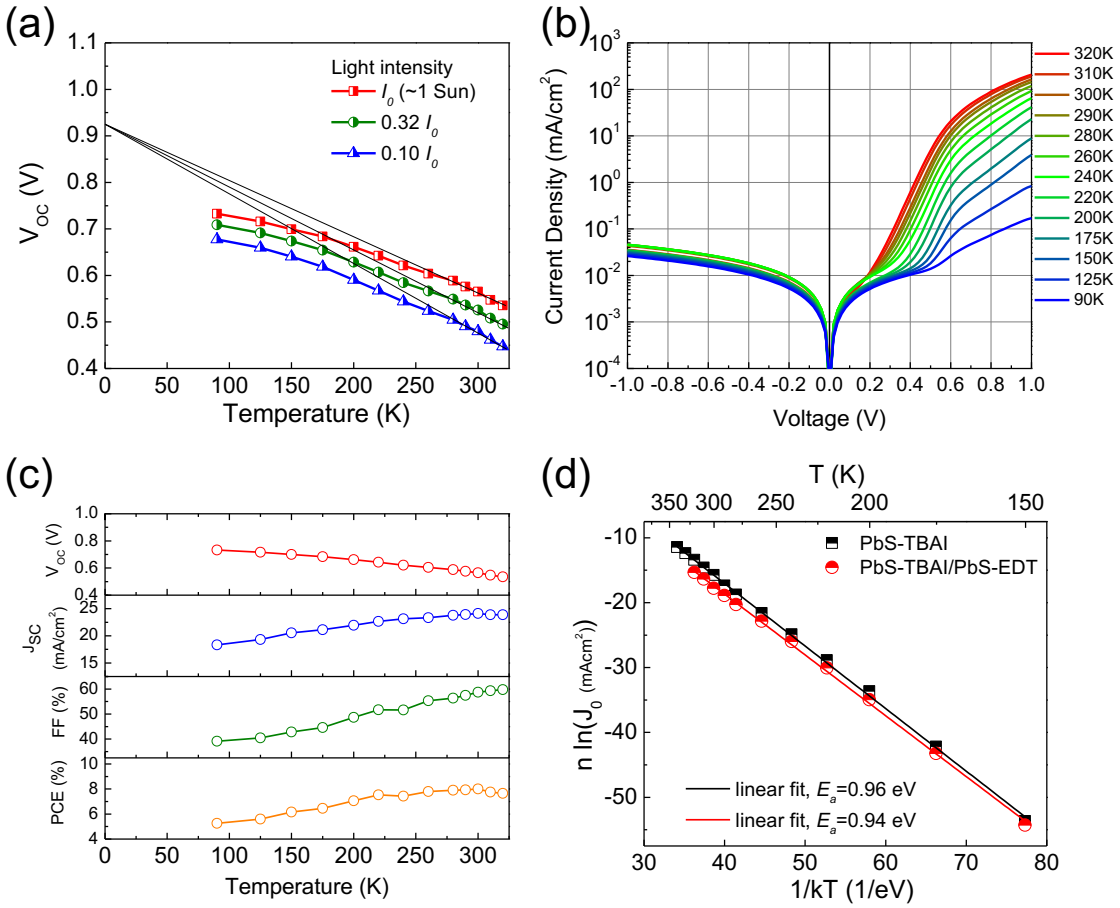

Figure 5.4 Temperature dependence of PbS-TBAI QD/PbS-EDT QD QDPV performance. (a) Temperature dependence of V_{OC} under 3 different light intensities. Black lines: linear fits. (b) Temperature dependence of dark J-V characteristics. (c) Temperature dependence of photovoltaic parameters under approximately 1-Sun illumination. (d) Relationship between n ln(J_0) and $1/kT$ (symbols) for estimation of the activation energy E_{a}. Values of n and J_0 are extracted by fitting the dark J-V curves shown in (b). Solid lines: linear fit corresponding to $E_{\mathrm{a}} = 0.94 \pm 0.01$ eV for a PbS-TBAI QD/PbS-EDT QD device (red). The PbS-TBAI QD device shows similar behavior with an activation energy of 0.96 ± 0.01 eV (black).

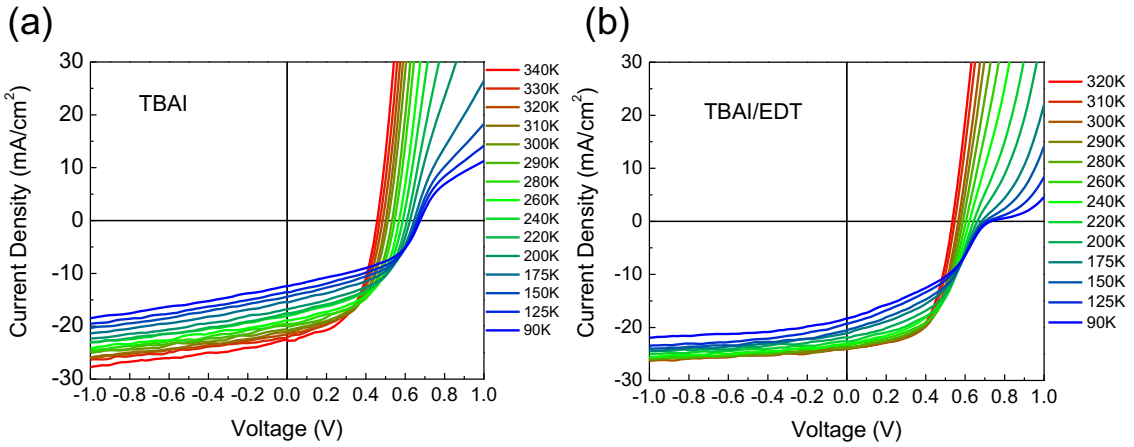

Figure 5.5 J-V characteristics of devices under approximately 100mW/cm^2 illumination at different temperatures. (a) PbS-TBAI QD device, (b) PbS-TBAI QD/PbS-EDT QD device.

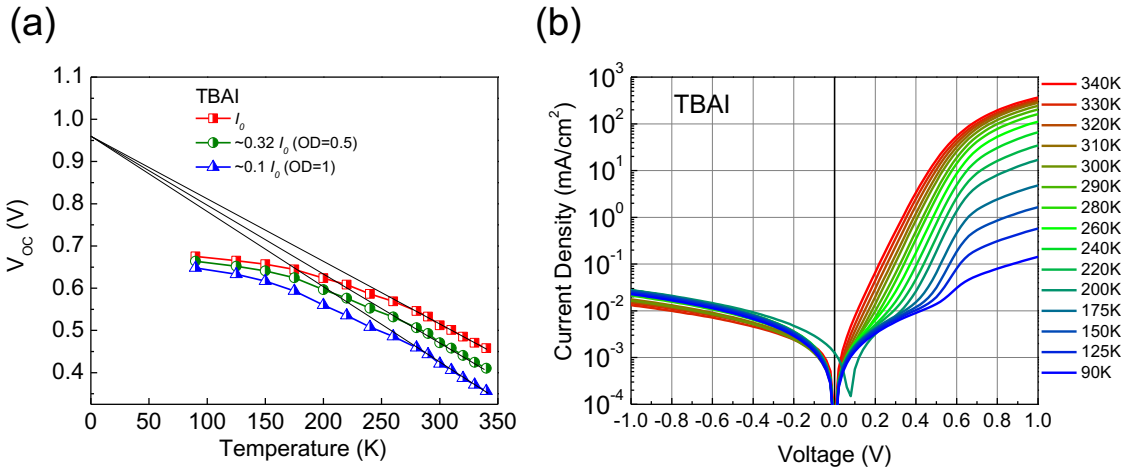

Figure 5.6 Temperature dependence of PbS-TBAI QDPV performance. (a) Temperature dependence of V_{OC} under 3 different light intensities. Black lines: linear fits. (b) Temperature dependence of dark J-V characteristics.

5.4 Sub-Bandgap States as the Origin of High V_{OC} Deficit

Based on the experimental results described above, we discuss the origins of the V_{OC} deficit. One component of the V_{OC} deficit is the below-bandgap activation energy (E_a~0.92 eV) for dark current generation, which can be interpreted in two possible scenarios:

(1) Interfacial recombination could be a dominant process, and E_a represents the bandgap of PbS QDs minus the conduction band offset between ZnO and PbS QDs (Figure 5.7a).

(2) E_a is the energy difference between the sub-bandgap states and the band edge—the "effective gap" in QDs (Figure 5.7b).

As we discuss below, scenario (2) appears more likely to be the origin of the below-bandgap activation energy.

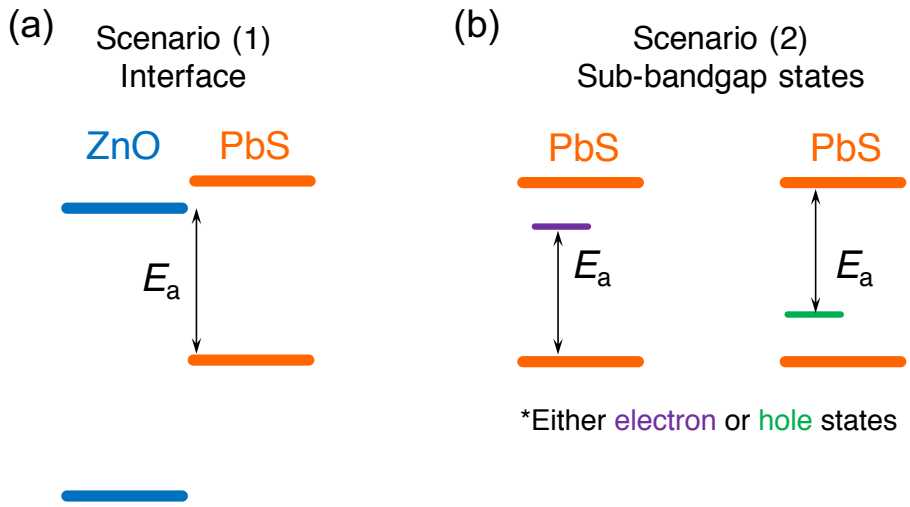

Figure 5.7 Mechanisms for the below-bandgap activation energy (E_a) for dark current generation (a) interface recombination. (b) sub-bandgap states. E_a could be the difference between sub-bandgap states and valence band (left) or conduction band (right), depending on the nature of the sub-bandgap states.

If interfacial recombination at the ZnO/PbS QD heterojunction is the dominant mechanism (scenario 1), optimization of the ZnO/PbS QD interface by tuning the band-edge energy levels or carrier concentration of ZnO could potentially improve the V_{OC}. Enhancement of V_{OC} *via* these approaches has been seen [103, 105–107], yet the observed V_{OC} values are similar to those reported elsewhere and remain considerably lower than the bandgap. In addition, caveats exist in determining the band alignment at heterojunctions. In related literature, the band-edge positions of oxides and QDs are often measured individually and referenced to the vacuum level to form the band diagram. This approach could be inaccurate, as we discuss in the section 5.8.1. In short, surface states, surface dipoles, gap states, and chemical interactions between two materials could affect the band offset or cause Fermi level pinning [108]. Such phenomena have been seen in many QDPV systems [35, 36, 48, 50, 59]. Consequently, for discussion on the effects of interfacial band alignment engineering on device performance, performing direct measurements of the relative band alignment from bilayer samples may be more valuable.

In the case of scenario (2), the effective gap E_a is determined by the position of the sub-bandgap energy levels (Figure 5.7b). The good agreement of the energy difference between the bandgap and E_a ($E_g - E_a \approx 0.21$ eV), and the energy difference between the band-edge and sub-bandgap state emission (~0.23 eV), is consistent with this scenario. This energy difference is similar to the trap activation energy (~0.26 eV) for PbS QDs of this size.[109] This scenario also explains the limits of achievable V_{OC} from interface engineering of the oxide layer in previous reports [103, 105–107]. In scenario (2), the generation-recombination is dominated by *bulk* generation-recombination in QDs through the sub-bandgap states. Thus, the "effective gap" E_a represents the upper bound of the achievable V_{OC}. A similar effective gap concept has been proposed by Nagpal and Klimov, who further proposed the existence of a weakly conducting "mid-gap band" formed by these states for charge transport [85]. We have confirmed that EDT-treated QDs show

similar sub-bandgap emission (Figure 4.8), suggesting sub-bandgap states are not unique to halide-treated QDs. Therefore, this component of the V_{OC} deficit exists in organic ligand passivated QDs as well. In fact, a below-bandgap E_a in organic ligand-passivated QDs has also been reported [110].

5.5 Minor Component of V_{OC} Deficit

Another component of the V_{OC} deficit at room temperature depends on the junction characteristics which determine the J_{SC}, n, and J_{00} (and thus the slope in Figure 5.4a). The latter two factors are not independent of each other, both being governed by recombination–generation mechanisms, carrier concentration, carrier mobility, and carrier lifetimes in the two materials forming the junction. (A brief discussion on the validity of carrier type, concentration, and mobility is provided in section 5.8.2).

The difference in the V_{OC} of organic and halide-passivated QD devices may be attributed to this second component of the V_{OC} deficit. As mentioned earlier, devices based on PbS-TBAI QDs show faster carrier recombination rates than devices based on organic ligand-passivated PbS QDs. In line with the fast recombination rate, the J_0 of our PbS-TBAI QD and PbS-TBAI QD/PbS-EDT QD devices, $(1.1 \pm 0.2) \times 10^{-4}$ mA/cm^2, is several orders of magnitude higher than that of other organic ligand-passivated PbS QDPVs (10^{-7}–10^{-5} mA/cm^2) [47, 59, 111]. We argue that the high J_0 in PbS-TBAI QD devices may be due to the low hole concentration. Based on measured band positions, the Fermi level is closer to the mid-gap in PbS-TBAI QD than in PbS-EDT QD, suggesting a lower hole concentration in the former [35]. In a typical p–n junction, decreasing the hole concentration of the p-type material (the PbS QD layer in the ZnO/PbS QD heterojunction) increases both J_0 and the p-side depletion width. For PbS QD cells with short carrier diffusion lengths (<100 nm) [64], the majority of collected photocarriers is generated within the depletion region. Therefore, a longer depletion width can improve photocurrent collection efficiency and thus J_{SC}. Nevertheless,

the higher J_0 would also cause a reduction in V_{OC}. This argument may explain the general trend observed in QDPVs: devices based on PbS-TBAI QDs or other halide passivated PbS QDs exhibit a higher J_{SC} than organic ligand-passivated PbS QDs [33–35], but a lower V_{OC} due to the high recombination rate and J_0.

5.6 Discussion: Future Direction

The sub-bandgap states may also be responsible for inefficient carrier collection, a significant loss in QDPVs with a thicker absorber layer. To date, the highest $J_{SC,EQE}$ (J_{SC} calculated by integrating the product of EQE and the AM1.5 solar photon flux; we note parenthetically that this calculation appears to have been performed incorrectly in some publications as we discuss in section 5.8.3) in QDPV is 26–29 mA/cm^2 for devices with an EQE onset of ~1 eV [44, 97]. The highest reported and independently verified J_{SC} is 24.2±0.7 mA/cm^2 for a device with an EQE onset of ~1.13 eV [35]. These values are only 60% of their corresponding theoretical maxima. It can be seen from Figure 5.8a that a device with a thin PbS-TBAI QD absorber (220 nm thick) shows a high internal quantum efficiency (IQE) of 70–80%, consistent with reported high IQE in lead chalcogenide QDs [44, 56]. Clearly, insufficient absorption of long-wavelength photons limits EQE in thin devices. However, thicker devices benefit from increased absorption of long-wavelength photons at the expense of carrier collection efficiency (Figure 5.8b and Figure 5.8c), a consequence of short carrier diffusion lengths. We believe it is the presence of the sub-bandgap states instead of carrier mobility that limits the carrier diffusion length. Although the trapped carrier density in PbS QDs seems relatively low, only 10^{-4} – 10^{-2} per QD [112, 113], the corresponding volumetric concentration (10^{15} – 10^{17} cm^{-3}) is comparable to or higher than the concentration of photogenerated carriers. At such high concentrations, increasing carrier mobility does not improve the carrier diffusion length [99, 113].

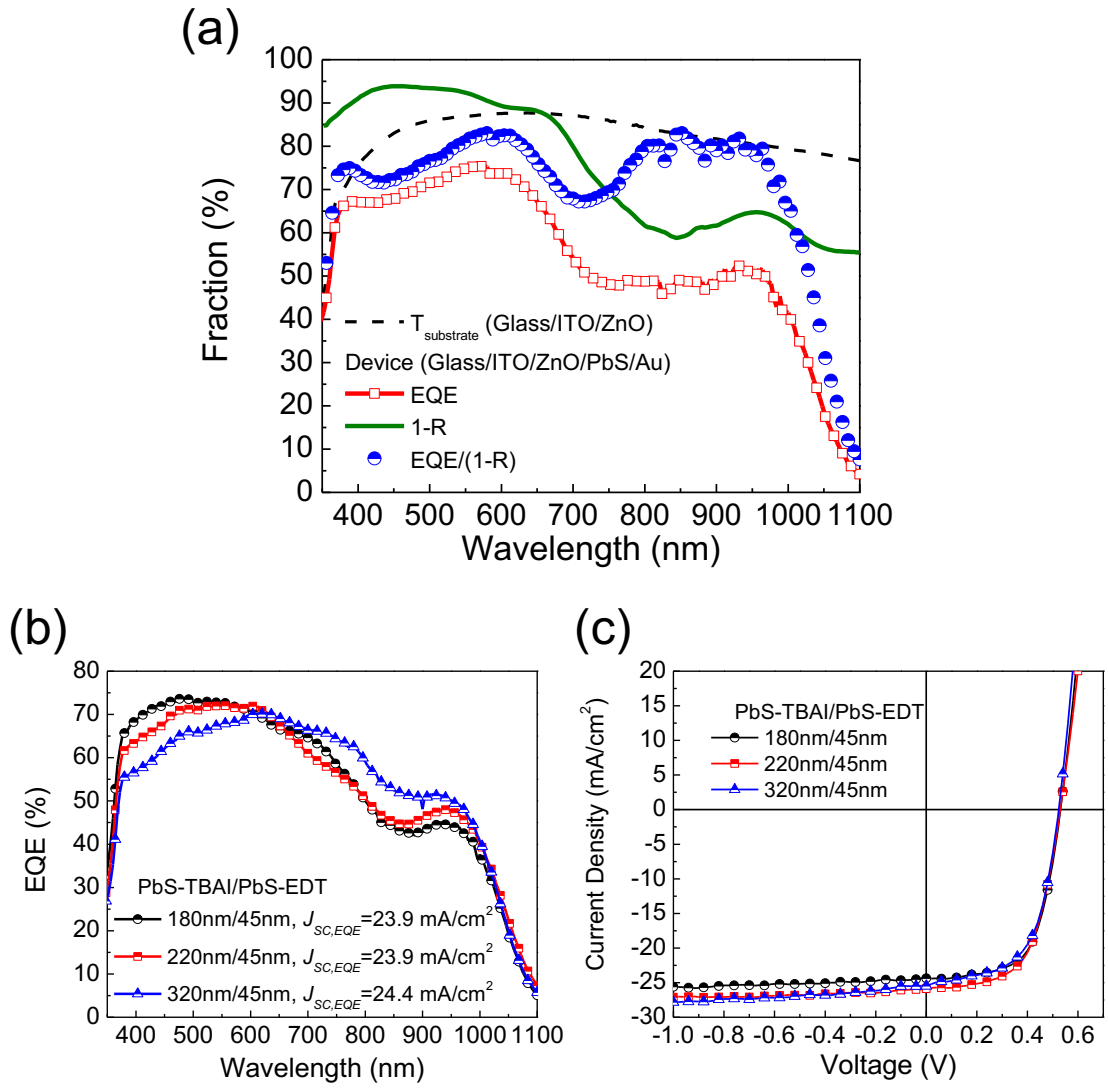

Figure 5.8 Inefficient photocurrent collection efficiency of thicker PbS-TBAI QD/PbS-EDT QD solar cells. (a) The EQE, 1-R, and EQE/(1-R) spectra of a thin PbS-TBAI QD(220 nm)/PbS-EDT QD(45 nm) device; R: diffuse reflectance of the device. The 1-R represents an upper bound for PbS QD absorption so EQE/(1-R) represents a lower bound for IQE in the PbS QD layer. The transmittance of the substrate (glass/ITO/ZnO) $T_{\text{substrate}}$ is also shown. The device shows lower EQE at long-wavelengths due to insufficient photon absorption. (b) EQE spectra of PbS-TBAI QD/PbS-EDT QD devices with different PbS-TBAI QD absorber thicknesses. Expected short-circuit current densities ($J_{\text{SC,EQE}}$) are calculated by integrating the EQE with the AM1.5 solar spectra (100 mW/cm^2). Thicker devices benefit from increased absorption of long-wavelength photons at the expense of carrier collection efficiency. (c) J-V characteristics of the devices shown in (b).

PbS-TBAI/PbS-EDT	V_{OC} (V)	J_{SC} (mA/cm^2)	*FF* (%)	*PCE* (%)	$J_{SC,\ EQE}$ (mA/cm^2)
180 nm / 45 nm	0.531	24.4	63.1	8.2	23.9
220 nm / 45 nm	0.530	25.9	60.3	8.3	23.9
320 nm / 45 nm	0.524	25.4	58.6	7.8	24.4

Table 5-1 Solar cell parameters of the devices shown in Figure 5.8.

The presence of sub-bandgap states limits both V_{OC} and carrier collection. The latter limitation has been mitigated by employing nanostructured oxides to improve carrier collection efficiency [69, 97, 114]. However, the fundamental problem regarding the presence of sub-bandgap states remains yet to be solved. Rath *et al.* [110] have demonstrated a bulk-heterojunction device structure that can fill the sub-bandgap states in the dark by blending ZnO and PbS QDs. These devices exhibit an E_a equal to their absorber bandgap (1.05 eV), an ideality factor close to 1, and a high V_{OC} (0.7 V) close to the theoretical limit, although poor charge transport in that device structure limits photocurrent collection and efficiency. This demonstration also supports our claims that interfacial recombination may not be the dominant process. Therefore, it is clear that eliminating sub-bandgap states in PbS QD films is essential to improving QDPV. This could show a greater potential gain than may be attainable by further optimization of the QD/oxide interfaces. A recent study indicates that the number of trap states influences J_0 and thus the V_{OC} deficit in metal-semiconductor-metal devices, implying a potential gain in V_{OC} by reducing the density of trap states [109]. It is worth noting that even with significant sub-bandgap states, current QDPVs still achieve efficiencies as high as ~9%. Eliminating sub-bandgap states can potentially increase the diffusion length by reducing recombination and trapping in these states, leading to simultaneous and significant improvements in

V_{OC} and J_{SC}. These improvements may well lead to power conversion efficiencies above 15%.

We highlight tailoring QD stoichiometry as a promising route to achieving this goal. Stoichiometric control of QDs has been demonstrated in PbSe QD Schottky devices by thermally evaporating excess Pb or Se atoms onto the surface [115]. Finding effective methods to control the stoichiometry across the whole QD layer may pave the way for highly efficient QDPVs. Possible strategies include exploring new ligands in combination with post-deposition treatments. In particular, employing recently developed halide ligands [33, 116, 117] and tuning the carrier concentration and stoichiometry could be promising approaches.

5.7 Summary

In summary, we have presented various analyses that provide a deeper understanding of the device working mechanisms and the present limitations in PbS QD solar cells. Our PL and EL studies unambiguously demonstrate the presence of sub-bandgap state filling effects in efficient PbS QDPVs. We show that the V_{OC} deficit can be attributed to two components: The below-bandgap activation energy accounts for a ~0.2 V loss in the maximum achievable V_{OC} and is most likely due to the energy level of the sub-bandgap states. Inefficient carrier collection and heterojunction characteristics such as the low hole concentration in halide-treated PbS QDs account for remaining losses. We conclude that eliminating the sub-bandgap states is essential to improving the performance of PbS QDPVs. We discuss possible origins of these states and suggest future directions that could guide the design of highly efficient QD solar cells.

5.8 Additional Discussion

5.8.1 Band Alignment at A Heterojunction

In many related works, the individually measured band edge positions of oxides and QDs are used. The band alignment is then determined by referencing these individually measured band edge positions to the vacuum level. Drawing the band alignment diagrams in this way could be misleading and incorrect due to the following reasons: (1) This simple band diagram is drawn before equilibration of the Fermi levels and therefore does not take into account band bending. A simple example is the band alignment between *n*-Si and *p*-Si with identical band edges relative to vacuum. (2) Surface states, surface dipole, gap states, and any interaction between two materials could affect the band offset or lead to Fermi level pinning. Therefore, the simplest model, Anderson's rule (or electron affinity rule), which states that the band offset at a heterojunction before and after contact remains the same, often fails to explain the measured band offset [25, 108]. Anderson's rule assumes that the potential is continuous across the interface. Therefore, the vacuum energy is continuous, and the conduction bands align according to their free-surface electron affinities. In reality, charge transfer or sheets of charges at an interface cause a step change in the potential right at the interface, so the band offset can shift away from the continuous potential model.

In the case of Si *p*–*n* homojunction, there are no surface states at the junction, so the electric potential is continuous. A *p*–*n* homojunction is typically a buried junction created by thermal diffusion or well-controlled ion implantation of dopants into a wafer followed by thermal annealing (drive-in). In other words, this type of buried junction is not created by depositing one material onto another different material. In the case of a buried junction, the conduction bands align across the junction. In contrast, the effects of surface states on the band alignment in Si-based heterojunctions have been widely observed and discussed, particularly at the Si-SiO_2 and Si-metal interfaces [25].

In the case of QDPVs and other emerging PV technologies, the heterojunctions are mostly created by sequential depositions of different materials. Surface states, Fermi-level pinning, surface dipoles, and chemical bonding between two materials may all alter the band offsets. Such phenomena have been seen in many QDPV systems. The Schottky barrier height between QDs and metals of different work functions is one example [48]. The existence of a hole extraction barrier between QDs and high work function metals is another [36, 50, 59]. The band alignment between QD layers with different ligand treatments is still another [35]. Therefore, simply quoting the individually measured band positions of two materials to draw the band alignment could lead to an incorrect band alignment. The actual band offsets should be measured directly on bilayer samples. A detailed discussion about the band alignment at a heterojunction and techniques to determine the band alignment can be found in a review article by Franciosi and Van de Walle [108].

5.8.2 Validity of Carrier Concentration and Carrier Type

To further improve device performance, it is important to understand and to accurately measure the carrier type, carrier concentration, and density of trap or sub-bandgap states. A thorough review by Bozyigit and Wood discusses the detail and the validity of several electrical characterization techniques.[118] In particular, they questioned the validity of previous attempts to quantify the carrier concentration in QDPVs by Mott-Schottky analysis [118]. We also note that carrier mobility and carrier type determined by field-effect transistor (FET) characteristics might not be representative of those in a photovoltaic device. FETs operate with a high density of electrically *injected* carriers moving in a long channel in the dark; in contrast, photovoltaic devices operate with a relatively low density of photogenerated carriers moving in the short vertical direction. Furthermore, FET characteristics also depend on the metal contacts. A recent study has demonstrated that PbSe QD can form either an *n*-channel or a *p*-channel FET, depending on the metal contact [119]. Therefore, *n*-channel QD FET characteristics do not guarantee

n-type QDs with electron as majority carriers. Care must be taken when interpreting the correlation between the performance of QD FETs and QDPVs.

5.8.3 Validity of Reported J_{SC} and Efficiency

The overestimation of J_{SC} and efficiency due to mischaracterization in many emerging PVs has drawn great attention [120]. Since PbX QDPVs have broad absorption ranges and can deliver a high J_{SC}, mismatch between the lamp and AM1.5 solar spectrum could lead to a significant error. A good practice is to compare the measured J_{SC} with the calculated $J_{SC,EQE}$. In most cases, the discrepancy between these two values should be within experimental error. If a large discrepancy is found, an explanation should be given [120]. Comparison of J_{SC} with the calculated $J_{SC,EQE}$ is often done in reported QDPVs. However, surprisingly, the calculation of $J_{SC,EQE}$ in QDPVs appears to have been performed incorrectly in many publications, leading to a 10–20% overestimation of $J_{SC,EQE}$, which is coincidentally similar to the measured J_{SC}. We suggest double-checking the calculation methods and the reference solar spectrum used for the calculation.

5.9 Experimental Methods

5.9.1 *J-V* Characteristics

All reported *J-V* curves in this work were measured by reverse scans (from +1 V to -1 V) with a short delay time (typically 10 ms). Devices show negligible hysteresis (difference between forward scan and reverse scan) under these testing conditions (Figure 5.9).

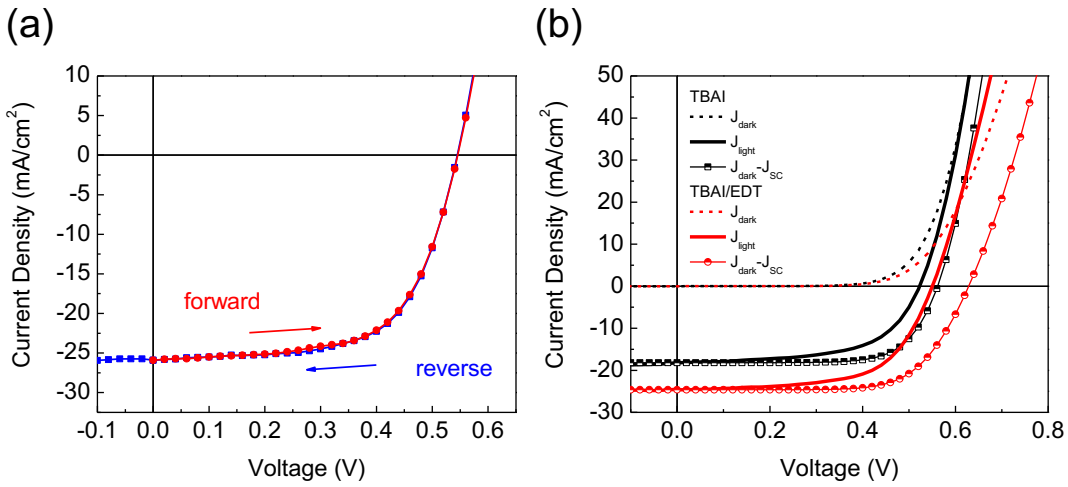

Figure 5.9 (a) Representative *J-V* curves of a PbS-TBAI QD/PbS-EDT QD device measured by forward (0V to +1V) and reverse scan (+1V to –1V). The device shows negligible hysteresis effects. (b) Dark *J-V* curves (J_{dark}), light *J-V* curves (J_{light}) and the superposition of J_{dark} and J_{SC} ($J_{dark} - J_{SC}$) of PbS-TBAI QD and PbS-TBAI QD/PbS-EDT QD devices. The J_{light} are not the superposition of the dark *J–V* curves and the J_{SC}, suggesting slight differences in generation-recombination mechanisms under dark and illumination or voltage-dependent carrier collection. This could explain the difference in the ideality factor n determined from J_{dark} and the light-intensity-dependence of V_{OC}.

5.9.2 *J-V-T* Measurements

For temperature-dependent *J-V* measurements, devices were mounted onto a custom-made stage in a liquid nitrogen-cooled cryostat. The white-light source was provided by a xenon lamp coupled to an optical fiber. The illumination intensity (I_0) was adjusted so that the *J-V* characteristics under I_0 approximately

match that under 100 mW/cm^2 AM1.5 illumination. For lower illumination intensities, neutral-density filters were placed between the cryostat and the light source (OD = 0.5 for 0.32 I_0, OD = 1 for 0.1 I_0; OD: optical density). Measurements were performed from low temperature to high temperature. Devices were allowed to equilibrate with the temperature of the cryostat for at least 20 minutes at different temperatures.

5.9.3 Transient Photovoltage

Transient photovoltage measurements were conducted with a Newport laser diode (832 nm) driven by a modulated square wave from a waveform generator (Agilent 33220). The steady-state white-light illumination was provided by a solar simulator. A series of neutral density filters was placed between the light source and the devices to adjust the intensity of the steady state bias white light. V_{OC} decay transients were recorded with a Tektronix TDS 3054B digital oscilloscope. The V_{OC} conditions were set by connecting the device output to the 1 MΩ input impedance of the oscilloscope.

5.9.4 Absorption, Reflection, and Estimation of IQE

The absorption spectrum of the PbS-TBAI QD film shown in Figure 1a was calculated by extinction coefficient: $\alpha = 4\pi\kappa/\lambda$, where α is the absorption coefficient, κ the extinction coefficient, λ the wavelength. Refractive index and extinction coefficient spectra of QD films were extracted by fitting variable-angle spectroscopic ellipsometry (VASE) data. Reflection ellipsometry measurements were performed in air with a Woollam V-VASE equipped with an AutoRetarder. No significant depolarization was observed.

The transmittance (T) and specular reflectance (R_{specular}) spectra of thin films and devices were measured with a UV-Vis-NIR spectrometer (Cary 5000, Agilent). Specular reflectance spectra were measured in a near-normal incidence (8°) geometry with a specular reflection accessory (Harrick Scientific). Diffuse

reflectance (R) measurements were taken on the full device stack using a Perkin-Elmer Lambda 950 UV-Vis spectrophotometer, with a 150 mm integrating sphere.

The absorption (A) of thin films and device stack were calculated by $A = 1 - T - R$ (Figure 5.10). Devices show negligible transmittance ($<1\%$) due to the presence of the reflective metal electrode (Figure 5.10c). The measured 1-T-R represents the total absorption of the device stack and thus the upper bound of the absorption in the PbS QD layer. The device IQE was estimated as EQE/(1-R), which represents the lower bound of the IQE of the PbS QD layer.

Acknowledgements

Patrick Brown, Jessica Carr, Justin Caram, Igor Coropceanu, Dr. Dong-Kyun Ko, Jonathan Mailoa, Jennifer Scherer, Mark Weidman, and Dr. Mark Wilson provided fruitful discussions and technical assistance. This work was supported by Samsung Advanced Institute of Technology, and in part by an NSF CAREER award ECCS-1150878. Part of this work made use of the MIT Laser Biomedical Research Center (LBRC) under contract number 9-P41-EB015871-26A1, supported by the National Institute of Health.

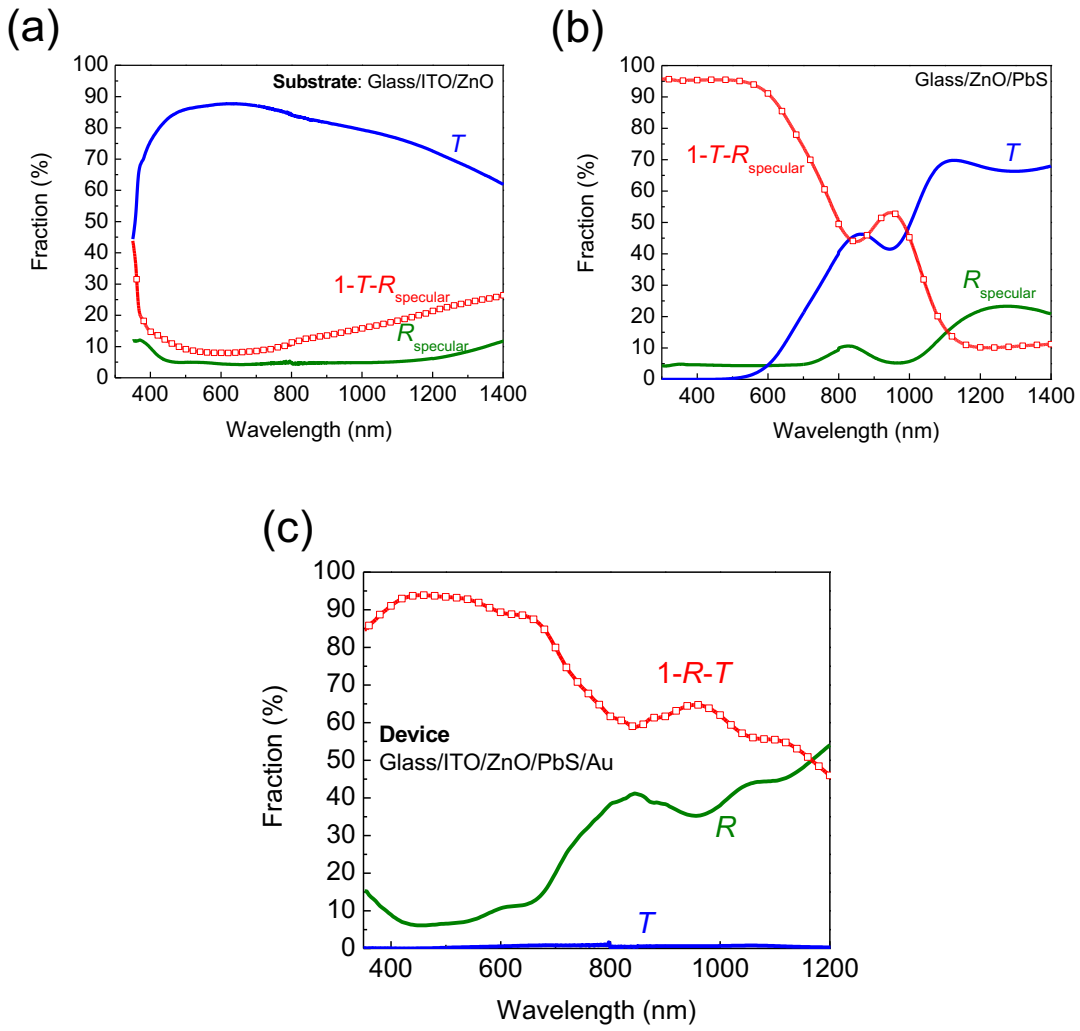

Figure 5.10 Transmittance (T), diffuse reflectance (R) or specular reflectance (R_{specular}), and absorption (1-T-R) spectra of (a) a glass/ITO/ZnO substrate, (b) a glass/ZnO/PbS-TBAI QD (~220 nm) film, and (c) a complete device stack, glass/ITO/ZnO/PbS-TBAI QD(~220 nm)/PbS-EDT QD(~45 nm). The 1-T-R in (c) represents the absorption of the device stack and thus the upper bound of the absorption in the PbS QD layer.

Appendix A
ZnO Nanowires for Improved Photocurrent Extraction in QD Solar Cells

This work is in collaboration with Paul H. Rekemeyer and Sehoon Chang.
A manuscript containing more details of this work has been submitted for publication.

A strategy to overcome the trade-off between light absorption and photocurrent collection (due to short carrier diffusion lengths) in QD solar cells is to pair QDs with nanostructured *n*-type materials. By using nanostructures, the effective distance for photogenerated minority carriers to travel to the charge-collecting layers is reduced. Therefore, the photocurrent collection efficiency in thicker devices, which can absorb more light, would not be significantly sacrificed. ZnO or TiO_2 nanowires have been previously employed in QD solar cells to improve photocurrent extraction [69, 97, 114]. However, the efficiencies of these previous devices are limited to about 6 % because of the quality of the PbS QD layer. Specifically, both the ligand used to passivate PbS QDs and the back surface at the QD/anode interface are not optimal. In this work, we combine ZnO nanowires with the PbS-TBAI/PbS-EDT device architecture. The nanowire-based devices show higher performance and J_{SC} compared to planar devices due to the improved photocurrent collection.

Figure A.1a shows a scanning electron microscopy (SEM) image of ZnO nanowires grown on a ITO substrate used in this work. The ZnO nanowires were grown *via* a hydrothermal method adapted from the literature [69]. A tilted SEM image of a ZnO nanowire/PbS QD photovoltaic device shows a good infiltration of QDs into the ZnO nanowires (Figure A.1b). High resolution transmission electron microscopy (HRTEM) coupled with energy dispersive spectroscopy (EDS), shown in Figure A.2, was used to confirm the existence of two distinct PbS QD functional layers and the penetration of PbS QDs into the ZnO nanowire array. The ~40 nm thick PbS-EDT layer can be distinguished from the PbS-TBAI layer in the bright-field transmission electron microscopy (TEM) images due to the different mass-thickness contrast in PbS QDs with and without heavy iodide atoms (Figure A.2a and b). The cross-sectional elemental analysis by the energy dispersive X-ray spectroscopy (EDS) coupled with SEM (Figure A.2c) further confirms this ZnO nanowire/PbS-TBAI/PbS-EDT/Au device architecture.

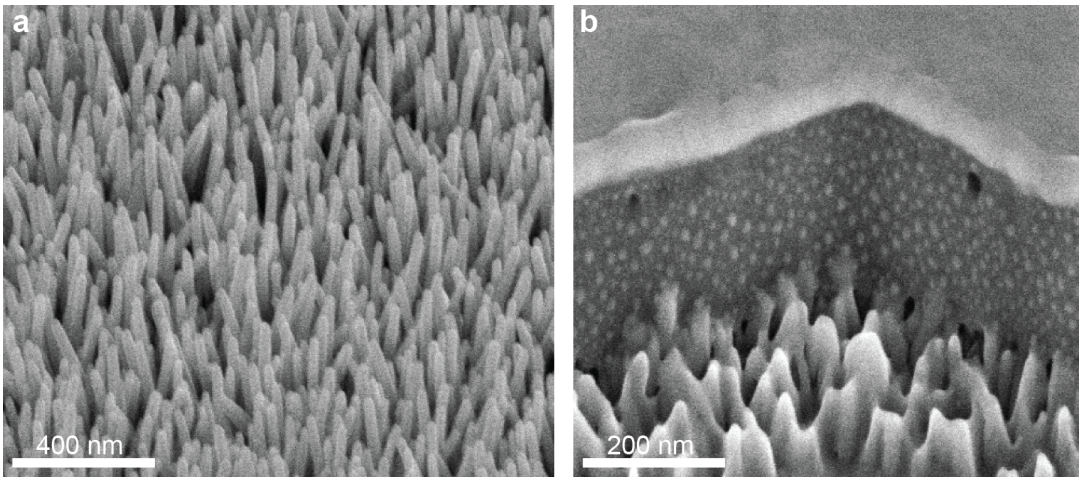

Figure A.1 (a) 45° tilt SEM image of ZnO nanowire arrays grown on ITO electrode. (b) 45° tilt SEM image of the ZnO nanowire arrays covered with QDs after partially removing the PbS QD layer with a focused ion beam.

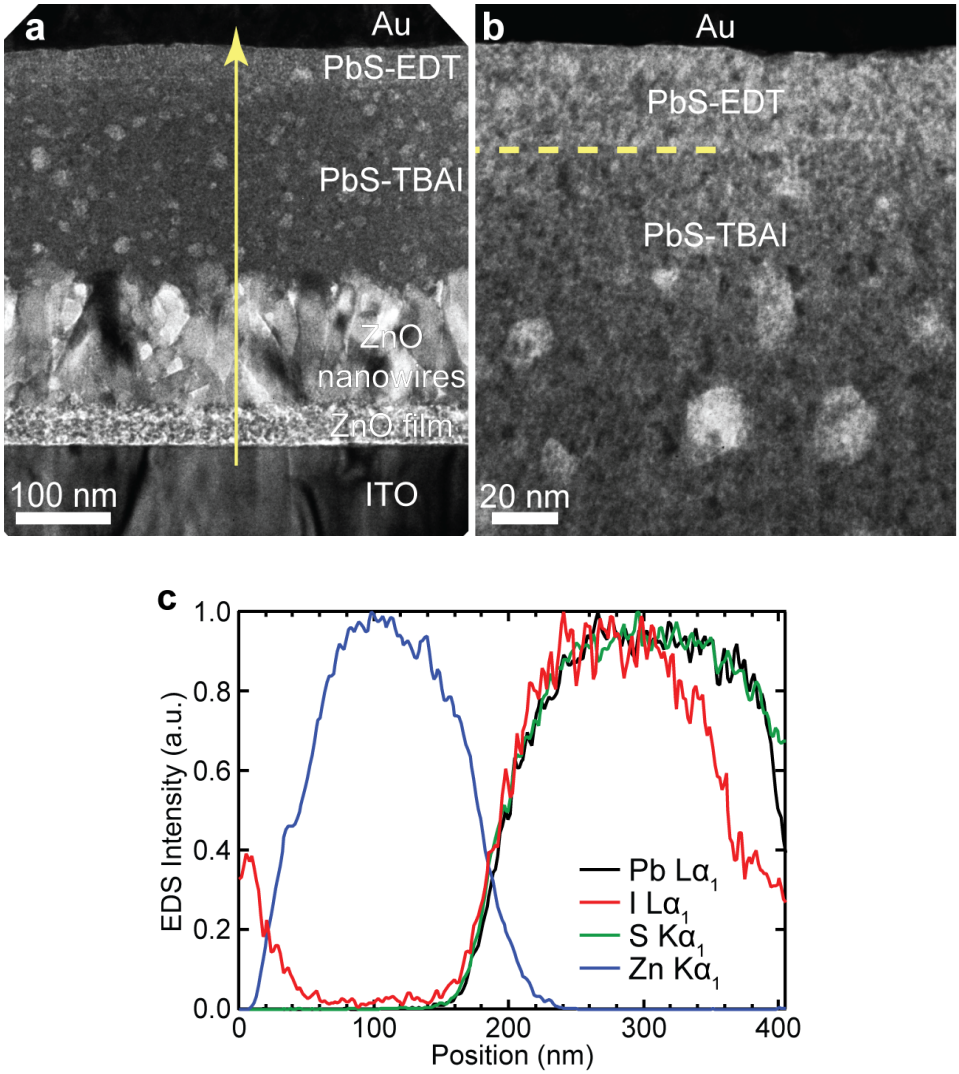

Figure A.2 (a) Bright-field cross-section TEM image of a device. (b) Higher magnification bright-field TEM image of the QD film immediately below the Au contact. The PbS-EDT layer gives less mass-thickness scattering than the PbS-TBAI layer, and thus appears brighter. (c) Normalized EDS linescan along the arrow in (a) confirming that the PbS-TBAI and PbS-EDT layers are chemically distinct. The iodine signal at position <60 nm is an artifact due to the proximity of the I $K_{\alpha 1}$ (3.94 keV) and the Sn $K_{\beta 2}$ (3.90 keV; from ITO) characteristic X-ray lines.

The J–V characteristics of a representative ZnO nanowire/PbS-TBAI/PbS-EDT device is shown in Figure A.3a. This nanowire-based device exhibits a high J_{SC} of 29.2 mA/cm^2 and a power conversion efficiency of 9.6 %. Integrating the corresponding EQE spectra with AM1.5 solar spectrum yields a predicted $J_{SC,EQE}$ of 29.4 mA/cm^2 (Figure A.3b), supporting the high measured J_{SC}. This J_{SC} value is higher than any planar ZnO/PbS-TBAI/PbS-EDT devices we have fabricated. It is also the highest reported J_{SC} for devices made of PbS QDs with the first exciton peaks at 850–950 nm, the most widely used PbS QDs for solar cells (in the optimal bandgap range). The results demonstrate the effectiveness of the combination of ZnO nanowires and the cascade energy level in PbS-TBAI/PbS-EDT for enhanced photocurrent collection in QD solar cells.

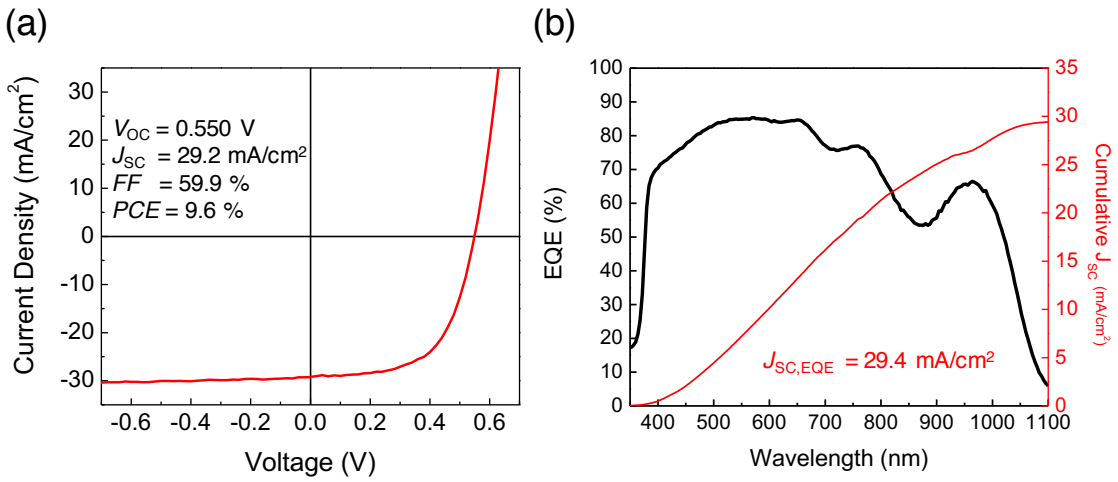

Figure A.3 (a) J–V characteristics of a representative ZnO nanowire/PbS-TBAI/PbS-EDT device. (b) The corresponding EQE spectrum (black) and the cumulative $J_{SC,EQE}$ (red) calculated by integrating the EQE with AM1.5 solar spectrum, comfirming the high J_{SC} in nanowire-based devices.

Appendix B
Extended Studies of the Band Alignment Strategy: Ligand/Size Combinations

Figure B.1a shows the thickness dependent UPS spectra of PbS-BDT (1,3-benzedithiol) on PbS-TBAI. The relative band alignment deduced from the UPS spectra is shown in Figure B.1b. No significant band offset is observed at the PbS-TBAI/PbS-BDT interface, unlike the PbS-TBAI/PbS-EDT device (Figure 3.9b) This TBAI/BDT combination does not result in improved device performance (Figure B.2) as a result of the lack of benefit from the band alignment strategy. The J_{SC} and V_{OC} are almost identical to a PbS-TBAI-only device.

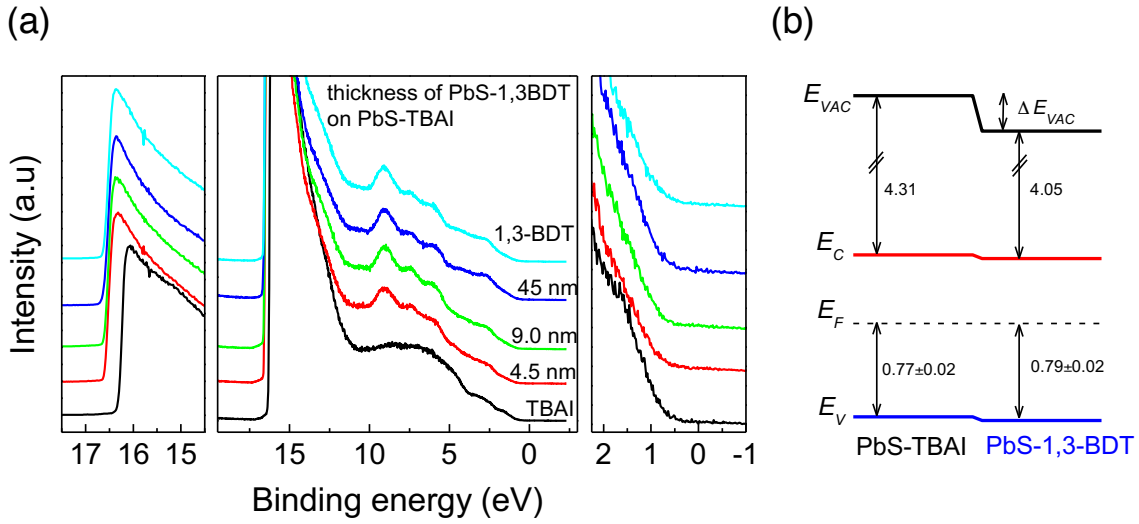

Figure B.1 (a) UPS spectra of PbS-TBAI, PbS-BDT, and PbS-BDT on PbS/TBAI with different thickness. (b) The relative band alignment deduced from the UPS spectra.

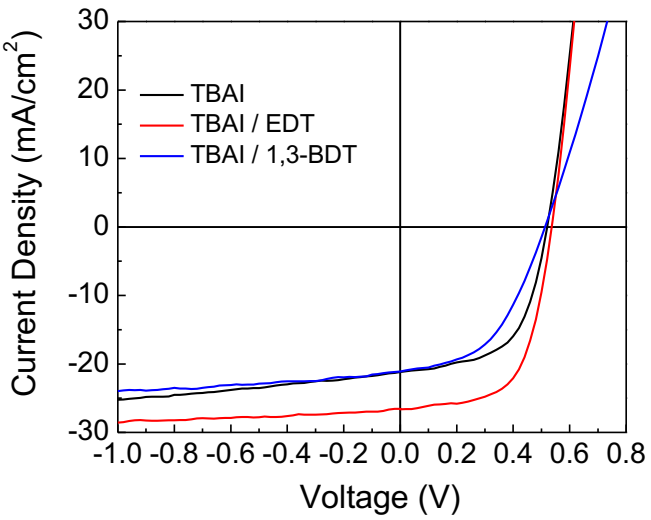

Figure B.2 J–V characteristics of a PbS-TBAI/PbS-BDT devices compared to a PbS-TBAI only device and a PbS-TBAI/PbS-EDT device.

Figure B.3 shows the J–V characteristics of TBAI/EDT devices employed different combinations of QDs. The TBAI-only devices made of 1.3 eV (black curve) and 1.5 eV (blue curve) QDs both show high *FF*. The band alignment strategy works well in the device made of 1.3 eV QDs (red curve). However, for devices employing 1.5 eV PbS-EDT QDs, S-shape J–V characteristics are found (green and orange curves). The results suggest that 1.5 eV PbS-EDT QDs do not form a favorable band alignment to the PbS-TBAI QDs and/or the Au electrode. This could be specific to this batch of QDs or QDs with this size (bandgap).

These results shown in Appendix B not only demonstrate the effectiveness of the band alignment strategy we developed but also indicate the importance of determining the relative band alignment between QDs with different ligand/QD size combinations.

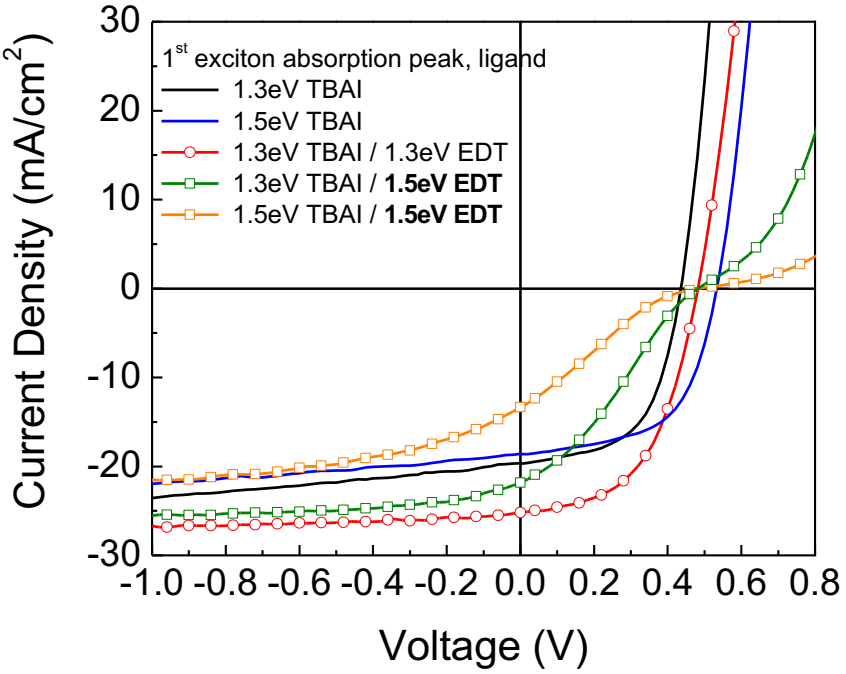

Figure B.3 J–V characteristics of devices employed different combinations of QD size.

Appendix C
Operational Stability Tests

Figure C.1a shows the results of an operational stability test on a PbS-TBAI/PbS-EDT device. During this preliminary study, the unencapsulated device was illuminated under constant AM 1.5 (100 mW/cm^2) illumination in air. The illumination spot size is larger than the substrate. A thermocouple was attached to the surface of the device to track the temperature. Between each *J*–*V* scan, the device was held at open-circuit under illumination (zero applied voltage and no current flow). As shown in the figure, the temperature of the device increased rapidly from ~25°C to ~50°C in the first 10 minutes and then stabilized at ~70 °C after 60 minutes. The change in efficiency is mainly from the change of V_{OC} and *FF*, which strongly correlate to temperature, whereas the J_{SC} is relatively insensitive to temperature. The performance of the device recovered to its original values after cooling back to room temperature in the dark. The device also continued to show similar efficiencies afterwards. Since the solar cell parameters are strongly temperature-dependent, the lack of a temperature control stage prevents us from decoupling the stability data from temperature effects.

In a modified experiment (Figure C.1b), in order to reduce heating effects, a heat sink and a smaller illumination spot size (smaller than the substrate but larger than the active area of the device under test) was used. The light source was a xenon lamp coupled to an optical fiber. The illumination intensity was adjusted

so that the J-V characteristics approximately match illumination at 100 mW/cm^2 AM 1.5 condition. Part of the glass-side of the substrate outside the active area was connected to a metal plate (as a heat sink) by using conducting copper tape. In this operational test, the device performance is stable up to 24 hours (Figure C.1b). These preliminary tests demonstrate the robustness of the QD solar cell based on iodide-passivated QDs under continuous illumination. The results are also consistent with a report of >1000 hours of operational stability in bromide-passivated PbS QD solar cells [92].

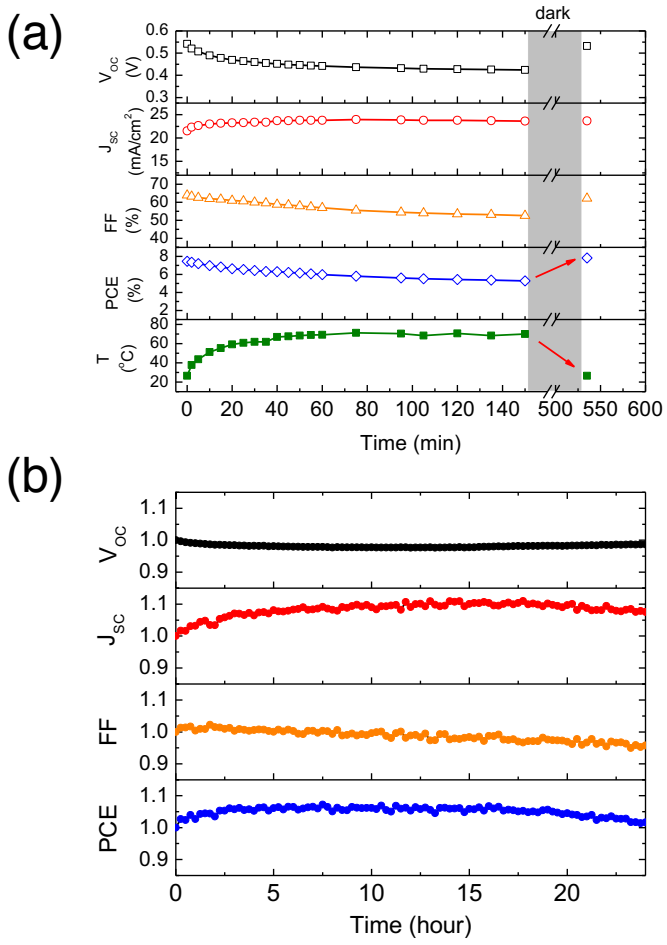

Figure C.1 Evolution of solar cell parameters of an unencapsulated cell under constant illumination in air. (a) illumination spot size larger than the substrate; no heat sink. (b) illumination spot size smaller than the substrate (but larger than the active area of the device); the device was connected to a heat sink. The parameters shown are normalized to the original values.

Appendix D
Post-Deposition Treatments on the Performance of QD solar Cells

Some post-deposition treatments were performed on PbS-TBAI films, attempting to "oxidize" the undercharged Pb atoms on the surface of QDs. Figure D.1 shows the characteristics of PbS-TBAI (180 nm)/PbS-EDT devices with (red) and without (blue) mild thermal annealing in air (100 °C, 20 minutes). The annealed device shows an improvement in the performance, achieving a high *FF* of 0.68 and a power conversion efficiency of 9.6 %. The difference in J_{SC} and EQE for devices with and without annealing are similar (comparable to experimental errors; Figure D.1a and Figure D.1b), suggesting that for devices with this thickness the carrier collection at 0 V is efficient and is not affected by thermal annealing. The improvement in *FF* might be due to a better carrier transport (higher carrier mobility) in the annealed PbS QDs [121], and/or a reduced density of sub-bandgap states/trapped carriers. Both effects could result in a longer carrier diffusion length, a weaker field-dependent carrier collection efficiency at forward biases, and thus a higher *FF*.

This mild thermal annealing treatment in air was applied to a device with a much thicker PbS-TBAI layer (360 nm). The higher EQE in this annealed thicker device (black curve in Figure D.1), particularly in the short-wavelength region,

suggests that the carrier diffusion length may be improved after the thermal treatment, unlike the devices without annealing shown in Figure 5.8b, which shows a reduction of EQE in the short-wavelength region and an improvement in the long-wavelength region with increasing thickness. However, it appears that the diffusion length is still short compared to the thickness of the device, as this device shows a stronger field dependent carrier collection and thus a lower *FF*.

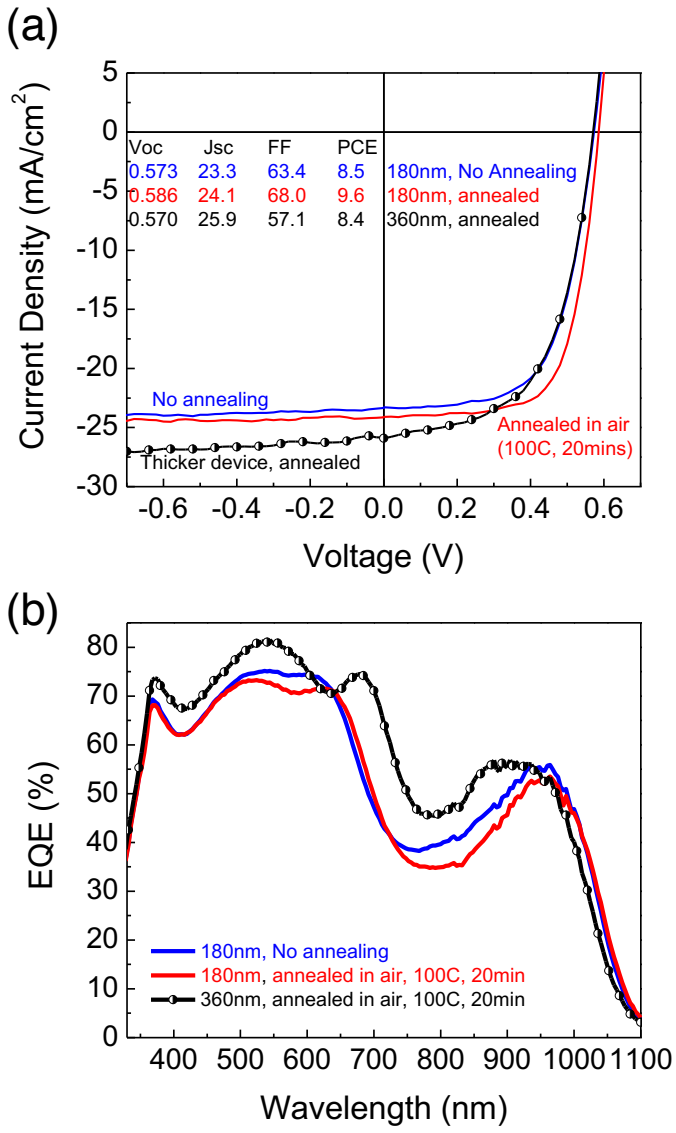

Figure D.1 Effects of thermal annealing in air on the performance of QD solar cells. (a) *J*–*V* characteristics. (b) The corresponsding EQE spectra.

It is also found that performing the thermal annealing on devices before the deposition of the PbS-EDT layer (*i.e.*, only the PbS-TBAI QDs layer is annealed; green curve in Figure D.2) and after the deposition of PbS-EDT layer (both layers are annealed; red curve) results in a similar performance enhancement when compared to the device without annealing (blue curve).

In an attempt to convert the undercharged Pb atoms on the surface of QDs into PbS, a thin layer of elemental sulfur (S) was deposited onto the PbS-TBAI layer by spin-coating (S in a saturated toluene solution). The film was then annealed in air, cooled down to room temperature, and then rinsed with toluene to remove the sulfur on the film before the deposition of the PbS-EDT layer. The resulting device performance (black curve in Figure D.2) is similar to other annealed devices without sulfur.

In summary, mild thermal annealing in air is found to slightly improve the performance of PbS QD solar cells, although more studies are required to verify the exact mechanisms contributing to the improvement. Importantly, the results demonstrate that PbS-TBAI is stable in air up to 100 °C. The slight improvement in V_{OC} in devices with thermal annealing indicates that this treatment may not completely eliminate the sub-bandgap states. This is consistent with the robustness of PbS-TBAI QDs, which cannot be easily oxidized in air. The attempt to oxidize the undercharged Pb atoms by thermal annealing with elemental sulfur did not achieve positive results. Therefore, these experiments suggest that finding other effective chemical oxidation methods to eliminate the sub-bandgap states would be good future directions.

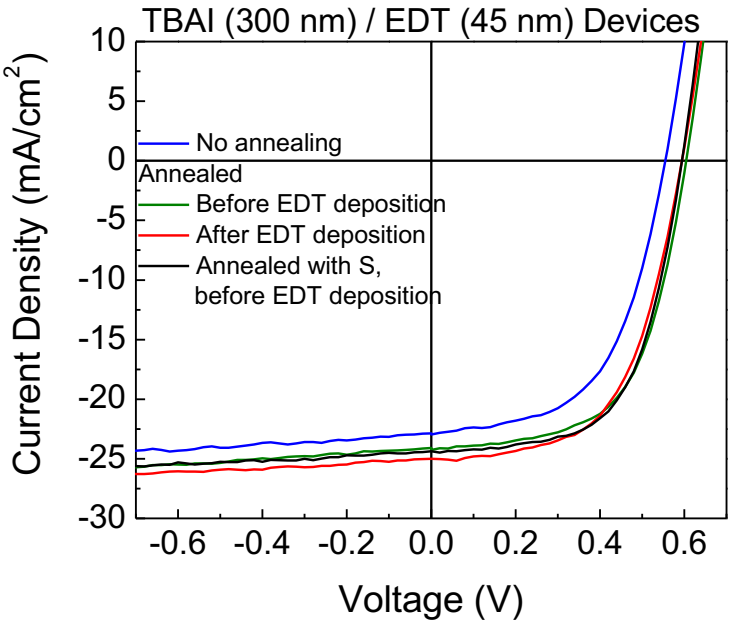

Figure D.2 J–V characteristics of devices with different post-deposition treatments.

Appendix E
Sodium Iodide (NaI) treatment

In this experiment, we show that iodide-passivated QDs can be fabricated by solid-state ligand exchange with purely inorganic salt sodium iodide (NaI). Figure E.1 shows the J–V characteristics and the cross-section scanning electron microscopy (SEM) image of a PbS-NaI/PbS-EDT device. The device was fabricated in a similar way to PbS-TBAI devices except that a NaI solution (10 mg/ml in methanol) was used for solid-state ligand exchange. The device was further annealed in air at 100 °C for 30 minutes before the deposition of the gold electrode. The PbS-NaI/PbS-EDT shows a V_{OC} of 0.548 V, a J_{SC} of 26.6 mA/cm^2, a FF of 60.48%, and a PCE of 8.8 % (Figure E.1a), comparable to PbS-TBAI/PbS-EDT devices. The results suggest that iodide-passivated QDs of similar quality can be obtained from different iodide salts, either with organic cation tetrabutylammonium (TBA^+) or inorganic cation Na^+. The TBA^+ ion may not exist in the final iodide-passivated PbS QD films (even if it does, it is not a necessary component and does not significantly affect the optoelectronic properties). In addition, the size of the cation does not directly affect the properties of the iodide-passivated QDs (TBA^+ is rather bulky compared to Na^+). It should be noted that the reactivity of the cations, the solubility of the iodide salts, and the solubility of cation-oleate may have different effects[122–124], but it is not the case in the TBAI and NaI treated PbS QDs.

One of the PbS-NaI/PbS-EDT device was sent to an accredited laboratory for an independent certification, showing the following certified solar cell parameters: V_{OC} = 0.5409±0.0054 V, J_{SC}=26.2±0.3 mA/cm^2, FF=58.6±1.2%, PCE=8.31±0.18% (Figure G.3). To the best of our knowledge, this is the highest certified J_{SC} in QD solar cells to date.

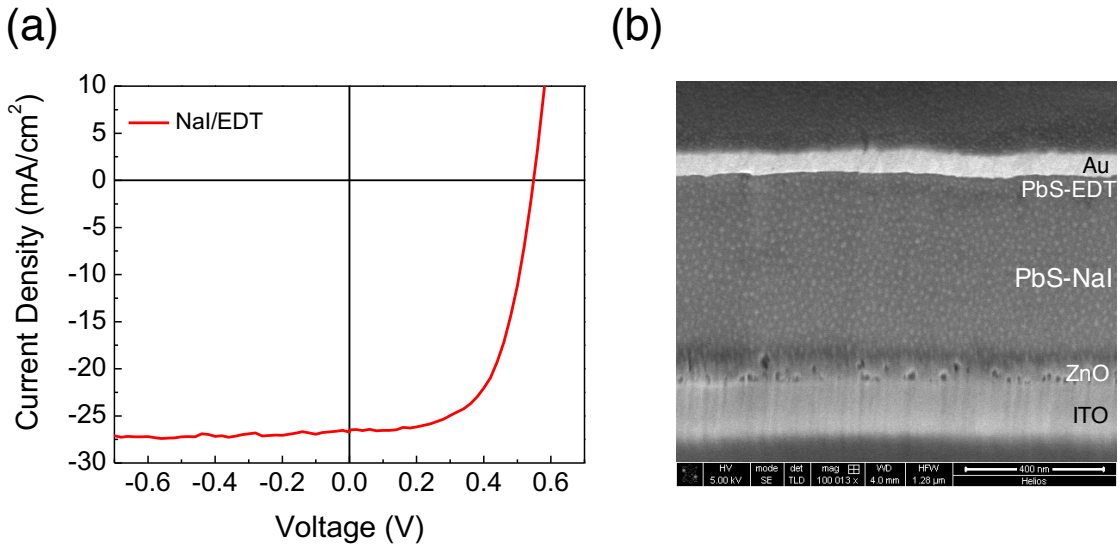

Figure E.1 (a) J–V characteristics of a PbS-NaI/PbS-EDT device. (b) Corss-section SEM image of the device. Scale bar: 400 nm.
SEM image: Paul Rekemeyer.

Appendix F

Tandem QD Solar Cells

Tandem cells with identical absorbers may overcome the trade-off between light-absorption and carrier collection by reducing the distance carriers have to travel to the collecting layers. This strategy has been employed in organic tandem cells [125], but has not yet been demonstrated in QD-based tandem cells.

Our preliminary work demonstrates the feasibility of this type of QD tandem cells (Figure F.1). The device architecture is ITO/top cell/recombination layer/bottom cell/Au, where the top cell is ZnO/PbS-TBAI (100 nm)/PbS-EDT (22 nm) and the bottom cell is ZnO/PbS-TBAI (300 nm)/PbS-EDT (45 nm). The recombination layer used in this solar cell is MoO_3 (10nm)/Au (2 nm). The power conversion efficiency of this preliminary tandem cell is 6.7 % (V_{OC}=0.951 V, J_{SC}=13.8 mA/cm^2, FF=51.3 %), which is higher than previously demonstrated QD tandem cells [61]. We expect that by optimizing the thickness of each sub-cell, the materials for the recombination layer, and the thickness of the recombination layer, the efficiency of tandem cell with identical absorbing material will exceed the efficiency of single junction cells. The optimization of the recombination layer would also serve as the basis for subsequent work on tandem cells with different absorbers.

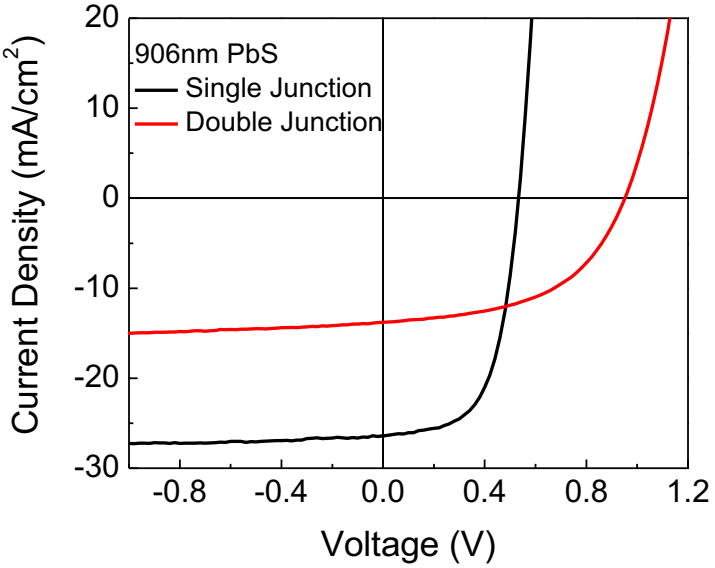

Figure F.1 J–V characteristics of a PbS QD double junction solar cell consisting of subcells made of QDs of the same bandgap (absorption peak at 906 nm) but different thicknesses.

Appendix G
Device Certification Reports

Figure G.1 shows the certification report of the 8.6 % record efficient (as of 2013) PbS-TBAI/PbS-EDT device described in Chapter 3.

Figure G.2 shows the certification report of a high *FF* (66.7%) PbS-TBAI/PbS-EDT device described in Chapter 3.

Figure G.3 shows the certification report of a PbS-NaI/PbS-EDT device described in Appendix E. This device shows the highest certified J_{SC} (26.2 mA/cm^2) to date.

Newport

ACCREDITED
Calibration Cert. # 2893.01

Technology and Application Center
PV Lab
Newport Calibration Cert. # 0930

DUT S/N: Cell 3
Newport Calibration #: 0930
Manufacturer: MIT
Material: CQD
Temperature Sensor: None
Environmental conditions at the time of calibration: Temperature: 23 ± 1 °C; Humidity: 45 ± 2%

The above DUT has been tested using the following methods to meet the ISO 17025 Standard by the PV Lab at Newport Corporation. Quoted uncertainties are expanded using a coverage factor of $k = 2$ and expressed with an approximately 95% level of confidence. Measurement of total irradiance is traceable to the World Radiometric Reference (WRR) and all other measurements and uncertainties are traceable to either NIST or CNRC and the International System of Units (SI). The performance parameters reported in this certificate apply only at the time of the test, and imply no past or future performance level.

Efficency [%]	8.55	±	0.18	V_oc [V]	0.5546	±	0.0055	I_sc [A]	0.00033	±	0.00001
P_max [mW]	0.12	±	0.00	V_max [V]	0.4201	±	0.0042	I_max [A]	0.00028	±	0.00001
FF [%]	63.8	±	1.3	Area [cm^2]	0.0137	±	0.0000	M	0.983	±	0.003

Methods:
I-V: ASTM E948-09 *Standard Test Method for Electrical Performance of Photovoltaic Cells Using Reference Cells Under Simulated Sunlight*
QE: ASTM E1021-06 *Standard Test Method for Spectral Responsivity Measurements of Photovoltaic Devices*

Standard Reporting Conditions:
Spectrum: AM1.5-G (ASTM G173-03/IEC 60904-3 ed. 2)
1000.0 W/m^2 at 25.0°C

Secondary Reference Cell:
Device S/N: 10510-0054 KG5
Device Material: mono-Si
Window Material: KG5
Certification: National Renewable Energy Laboratory
A2LA accreditation certificate # 2236.01
ISO Tracking #: 1754
Certified short circuit current (I_{sc}) under standard reporting conditions (SRC): 47.88mA
Calibration due date: 10-Jul-14

Solar Simulator:
Spectrum: Newport Corporation filename *Sol3A_Spectroradiometer_Scan_0130.xls*
Total irradiance: 1000 W/m^2 based on I_{sc} of the above Secondary Reference Cell

Quantum Efficiency for DUT:
Newport Corporation filename *QE 0930.xls*
Spectral mismatch correction factor: M = 0.983 ± 0.003

DUT Calibration Procedures:
Newport Corporation document QE1021 V1_6
Newport Corporation document Area Measurement V1_4
Newport Corporation document PV948 V1_9

Cal Cert V1.6	Issue Date: Oct 24, 2013	Page 2 of 2
	Reviewed and Approved by: Matthew O'Donnell	

Figure G.1 Certified record efficiency for colloidal quantum dot solar cells as of October, 2013. This unencapsulated device had been stored in air for 37 days before being tested in air by an accredited laboratory.

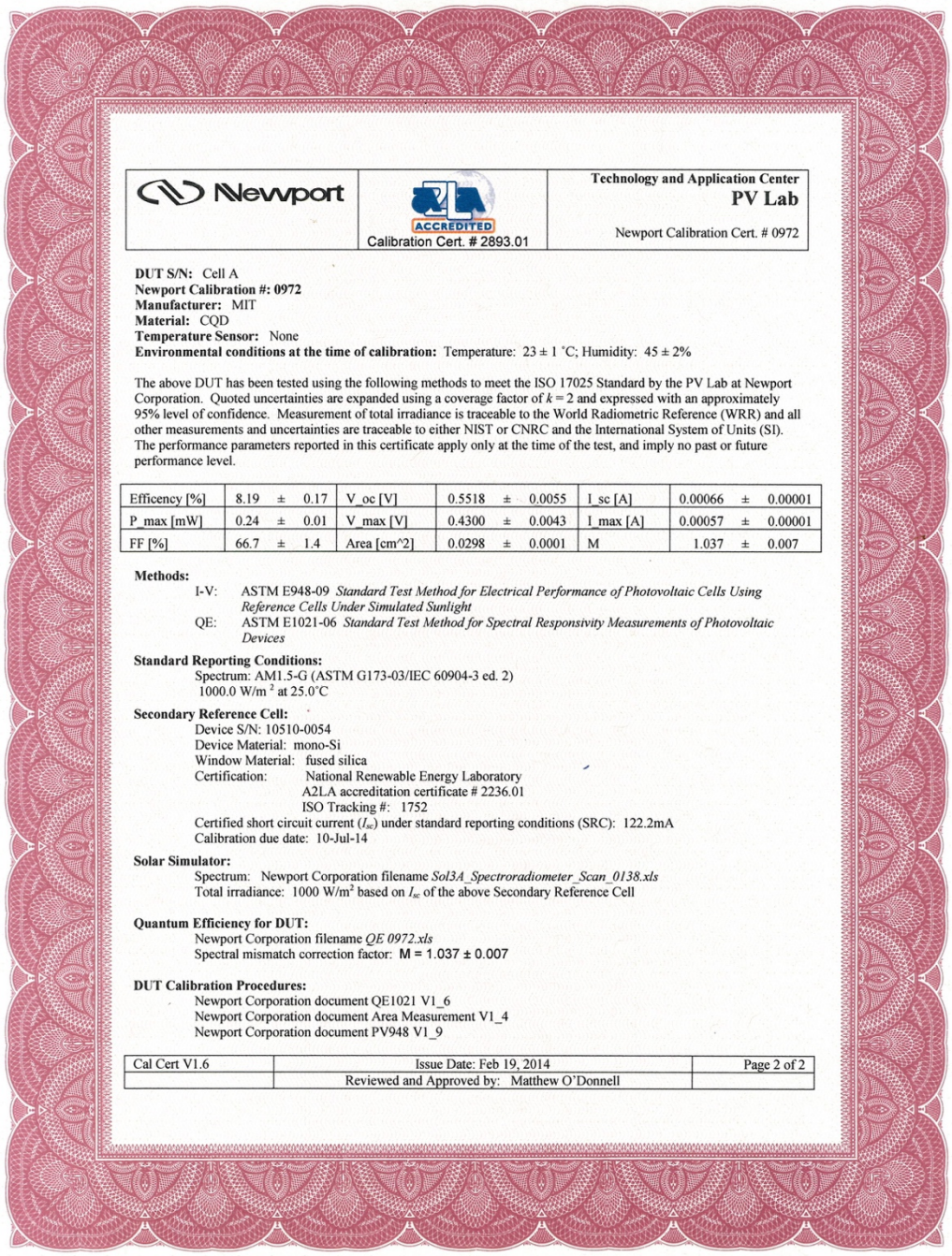

Newport

ACCREDITED
Calibration Cert. # 2893.01

Technology and Application Center
PV Lab
Newport Calibration Cert. # 0972

DUT S/N: Cell A
Newport Calibration #: 0972
Manufacturer: MIT
Material: CQD
Temperature Sensor: None
Environmental conditions at the time of calibration: Temperature: 23 ± 1 °C; Humidity: 45 ± 2%

The above DUT has been tested using the following methods to meet the ISO 17025 Standard by the PV Lab at Newport Corporation. Quoted uncertainties are expanded using a coverage factor of $k = 2$ and expressed with an approximately 95% level of confidence. Measurement of total irradiance is traceable to the World Radiometric Reference (WRR) and all other measurements and uncertainties are traceable to either NIST or CNRC and the International System of Units (SI). The performance parameters reported in this certificate apply only at the time of the test, and imply no past or future performance level.

Efficency [%]	8.19	± 0.17	V_oc [V]	0.5518	± 0.0055	I_sc [A]	0.00066	± 0.00001
P_max [mW]	0.24	± 0.01	V_max [V]	0.4300	± 0.0043	I_max [A]	0.00057	± 0.00001
FF [%]	66.7	± 1.4	Area [cm^2]	0.0298	± 0.0001	M	1.037	± 0.007

Methods:
I-V: ASTM E948-09 *Standard Test Method for Electrical Performance of Photovoltaic Cells Using Reference Cells Under Simulated Sunlight*
QE: ASTM E1021-06 *Standard Test Method for Spectral Responsivity Measurements of Photovoltaic Devices*

Standard Reporting Conditions:
Spectrum: AM1.5-G (ASTM G173-03/IEC 60904-3 ed. 2)
1000.0 W/m ^{2} at 25.0°C

Secondary Reference Cell:
Device S/N: 10510-0054
Device Material: mono-Si
Window Material: fused silica
Certification: National Renewable Energy Laboratory
A2LA accreditation certificate # 2236.01
ISO Tracking #: 1752
Certified short circuit current (I_{sc}) under standard reporting conditions (SRC): 122.2mA
Calibration due date: 10-Jul-14

Solar Simulator:
Spectrum: Newport Corporation filename *Sol3A_Spectroradiometer_Scan_0138.xls*
Total irradiance: 1000 W/m^2 based on I_{sc} of the above Secondary Reference Cell

Quantum Efficiency for DUT:
Newport Corporation filename *QE 0972.xls*
Spectral mismatch correction factor: M = 1.037 ± 0.007

DUT Calibration Procedures:
Newport Corporation document QE1021 V1_6
Newport Corporation document Area Measurement V1_4
Newport Corporation document PV948 V1_9

Cal Cert V1.6	Issue Date: Feb 19, 2014	Page 2 of 2
	Reviewed and Approved by: Matthew O'Donnell	

Figure G.2 Certified performance for a high fill factor device. This device was certified after 131 days of air storage and showed the highest FF of 66.7% in QD solar cells as of 2014. The nominal total device area for this device is 5.44 mm^2 defined by the overlap of the anode and cathode. For the certification, a 3 mm^2 mask was attached to the device to define the device area.

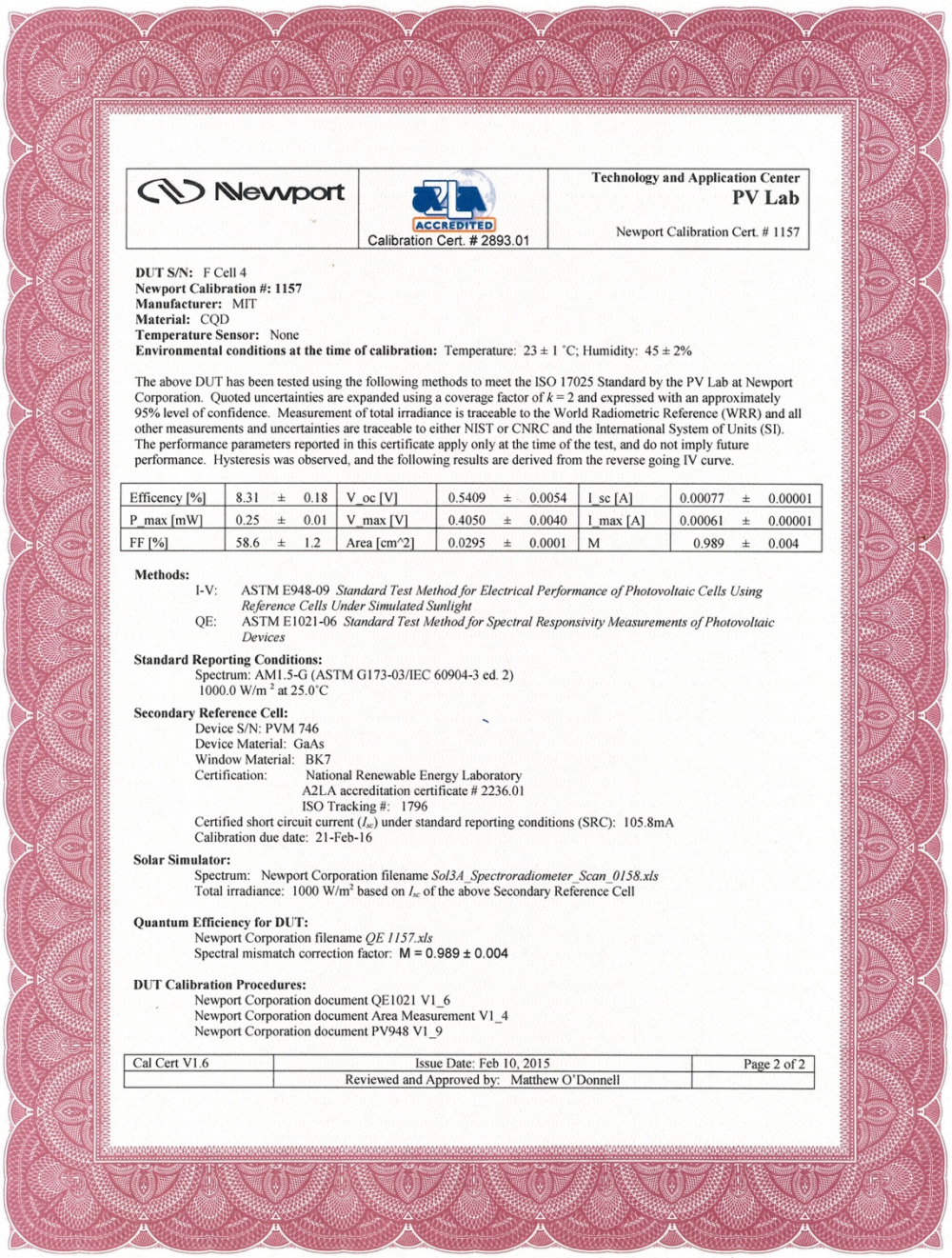

Newport

ACCREDITED
Calibration Cert. # 2893.01

Technology and Application Center
PV Lab
Newport Calibration Cert. # 1157

DUT S/N: F Cell 4
Newport Calibration #: 1157
Manufacturer: MIT
Material: CQD
Temperature Sensor: None
Environmental conditions at the time of calibration: Temperature: 23 ± 1 °C; Humidity: 45 ± 2%

The above DUT has been tested using the following methods to meet the ISO 17025 Standard by the PV Lab at Newport Corporation. Quoted uncertainties are expanded using a coverage factor of $k = 2$ and expressed with an approximately 95% level of confidence. Measurement of total irradiance is traceable to the World Radiometric Reference (WRR) and all other measurements and uncertainties are traceable to either NIST or CNRC and the International System of Units (SI). The performance parameters reported in this certificate apply only at the time of the test, and do not imply future performance. Hysteresis was observed, and the following results are derived from the reverse going IV curve.

Efficency [%]	8.31	±	0.18	V_oc [V]	0.5409	±	0.0054	I_sc [A]	0.00077	±	0.00001
P_max [mW]	0.25	±	0.01	V_max [V]	0.4050	±	0.0040	I_max [A]	0.00061	±	0.00001
FF [%]	58.6	±	1.2	Area [cm^2]	0.0295	±	0.0001	M	0.989	±	0.004

Methods:
I-V: ASTM E948-09 *Standard Test Method for Electrical Performance of Photovoltaic Cells Using Reference Cells Under Simulated Sunlight*
QE: ASTM E1021-06 *Standard Test Method for Spectral Responsivity Measurements of Photovoltaic Devices*

Standard Reporting Conditions:
Spectrum: AM1.5-G (ASTM G173-03/IEC 60904-3 ed. 2)
1000.0 W/m ^{2} at 25.0°C

Secondary Reference Cell:
Device S/N: PVM 746
Device Material: GaAs
Window Material: BK7
Certification: National Renewable Energy Laboratory
A2LA accreditation certificate # 2236.01
ISO Tracking #: 1796
Certified short circuit current (I_{sc}) under standard reporting conditions (SRC): 105.8mA
Calibration due date: 21-Feb-16

Solar Simulator:
Spectrum: Newport Corporation filename *Sol3A_Spectroradiometer_Scan_0158.xls*
Total irradiance: 1000 W/m^2 based on I_{sc} of the above Secondary Reference Cell

Quantum Efficiency for DUT:
Newport Corporation filename *QE 1157.xls*
Spectral mismatch correction factor: M = 0.989 ± 0.004

DUT Calibration Procedures:
Newport Corporation document QE1021 V1_6
Newport Corporation document Area Measurement V1_4
Newport Corporation document PV948 V1_9

Cal Cert V1.6	Issue Date: Feb 10, 2015	Page 2 of 2
	Reviewed and Approved by: Matthew O'Donnell	

Figure G.3 Certified device performance for a PbS-NaI/PbS-EDT device with the highest certified J_{SC} to date.

Bibliography

[1] F. W. Wise, Lead Salt Quantum Dots: The Limit of Strong Quantum Confinement. *Accounts of Chemical Research*, **33,** 773–780 (2000).

[2] C. B. Murray, D. J. Norris & M. G. Bawendi, Synthesis and Characterization of Nearly Monodisperse CdE (E = Sulfur, Selenium, Tellurium) Semiconductor Nanocrystallites. *Journal of the American Chemical Society*, **115,** 8706–8715 (1993).

[3] O. Chen, J. Zhao, V. P. Chauhan, J. Cui, C. Wong, D. K. Harris, H. Wei, H. Han, D. Fukumura, R. K. Jain & M. G. Bawendi, Compact High-Quality CdSe-CdS Core-Shell Nanocrystals with Narrow Emission Linewidths and Suppressed Blinking. *Nature Materials*, **12,** 445–51 (2013).

[4] J. Cui, A. P. Beyler, L. F. Marshall, O. Chen, D. K. Harris, D. D. Wanger, X. Brokmann & M. G. Bawendi, Direct Probe of Spectral Inhomogeneity Reveals Synthetic Tunability of Single-Nanocrystal Spectral Linewidths. *Nature Chemistry*, **5,** 602–6 (2013).

[5] V. I. Klimov, A. A. Mikhailovsky, S. Xu, A. Malko, J. A. Hollingsworth, C. A. Leatherdale, H. Eisler & M. G. Bawendi, Optical Gain and Stimulated Emission in Nanocrystal Quantum Dots. *Science*, **290,** 314–7 (2000).

[6] H. J. Eisler, V. C. Sundar, M. G. Bawendi, M. Walsh, H. I. Smith & V. Klimov, Color-Selective Semiconductor Nanocrystal Laser. *Applied Physics Letters*, **80,** 4614–4616 (2002).

[7] Y. Shirasaki, G. J. Supran, M. G. Bawendi & V. Bulović, Emergence of Colloidal Quantum-Dot Light-Emitting Technologies. *Nature Photonics*, **7,** 13–23 (2013).

[8] B. S. Mashford, M. Stevenson, Z. Popovic, C. Hamilton, Z. Zhou, C. Breen, J. Steckel, V. Bulovic, M. Bawendi, S. Coe-Sullivan & P. T. Kazlas, High-Efficiency Quantum-Dot Light-Emitting Devices with Enhanced Charge Injection. *Nature Photonics*, **7,** 407–412 (2013).

[9] P. O. Anikeeva, J. E. Halpert, M. G. Bawendi & V. Bulović, Quantum Dot Light-Emitting Devices with Electroluminescence Tunable over the Entire Visible Spectrum. *Nano Letters*, **9,** 2532–2536 (2009).

[10] G. J. Supran, K. W. Song, G. W. Hwang, R. E. Correa, J. Scherer, E. a.

Dauler, Y. Shirasaki, M. G. Bawendi & V. Bulović, High-Performance Shortwave-Infrared Light-Emitting Devices Using Core-Shell (PbS-CdS) Colloidal Quantum Dots. *Advanced Materials*, **27,** 1437–1442 (2015).

[11] K. Bourzac, Quantum Dots Go on Display. *Nature*, **493,** 283–283 (2013).

[12] S. M. Geyer, J. M. Scherer, N. Moloto, F. B. Jaworski & M. G. Bawendi, Efficient Luminescent down-Shifting Detectors Based on Colloidal Quantum Dots for Dual-Band Detection Applications. *ACS Nano*, **5,** 5566–5571 (2011).

[13] H.-S. Han, E. Niemeyer, Y. Huang, W. S. Kamoun, J. D. Martin, J. Bhaumik, Y. Chen, S. Roberge, J. Cui, M. R. Martin, D. Fukumura, R. K. Jain, M. G. Bawendi & D. G. Duda, Quantum Dot/antibody Conjugates for in Vivo Cytometric Imaging in Mice. *Proceedings of the National Academy of Sciences*, **112,** 1350–1355 (2015).

[14] J. Bao & M. G. Bawendi, A Colloidal Quantum Dot Spectrometer. *Nature*, **523,** 67–70 (2015).

[15] D. V Talapin, PbSe Nanocrystal Solids for N- and P-Channel Thin Film Field-Effect Transistors. *Science*, **310,** 86–89 (2005).

[16] T. P. Osedach, N. Zhao, T. L. Andrew, P. R. Brown, D. D. Wanger, D. B. Strasfeld, L. Chang, M. G. Bawendi & V. Bulović, Bias-Stress Effect in 1,2-Ethanedithiol-Treated PbS Quantum Dot Field-Effect Transistors. *ACS Nano*, **6,** 3121–7 (2012).

[17] S. J. Oh, N. E. Berry, J.-H. Choi, E. A. Gaulding, H. Lin, T. Paik, B. T. Diroll, S. Muramoto, C. B. Murray & C. R. Kagan, Designing High-Performance PbS and PbSe Nanocrystal Electronic Devices through Stepwise, Post-Synthesis, Colloidal Atomic Layer Deposition. *Nano Letters*, **14,** 1559–66 (2014).

[18] M. H. Zarghami, Y. Liu, M. Gibbs, E. Gebremichael, C. Webster & M. Law, P-Type PbSe and PbS Quantum Dot Solids Prepared with Short-Chain Acids and Diacids. *ACS Nano*, **4,** 2475–85 (2010).

[19] J.-S. Lee, M. V Kovalenko, J. Huang, D. S. Chung & D. V Talapin, Band-like Transport, High Electron Mobility and High Photoconductivity in All-Inorganic Nanocrystal Arrays. *Nature Nanotechnology*, **6,** 348–352 (2011).

[20] M. V Kovalenko, M. Scheele & D. V Talapin, Colloidal Nanocrystals with Molecular Metal Chalcogenide Surface Ligands. *Science*, **324,** 1417–1420

(2009).

[21] M. Law, J. M. Luther, Q. Song, B. K. Hughes, C. L. Perkins & A. J. Nozik, Structural, Optical, and Electrical Properties of PbSe Nanocrystal Solids Treated Thermally or with Simple Amines. *Journal of the American Chemical Society*, **130,** 5974–85 (2008).

[22] S. A. McDonald, G. Konstantatos, S. Zhang, P. W. Cyr, E. J. D. Klem, L. Levina & E. H. Sargent, Solution-Processed PbS Quantum Dot Infrared Photodetectors and Photovoltaics. *Nature Materials*, **4,** 138–42 (2005).

[23] G. Konstantatos, I. Howard, A. Fischer, S. Hoogland, J. Clifford, E. Klem, L. Levina & E. H. Sargent, Ultrasensitive Solution-Cast Quantum Dot Photodetectors. *Nature*, **442,** 180–183 (2006).

[24] J. P. Clifford, G. Konstantatos, K. W. Johnston, S. Hoogland, L. Levina & E. H. Sargent, Fast, Sensitive and Spectrally Tuneable Colloidal-Quantum-Dot Photodetectors. *Nature Nanotechnology*, **4,** 40–44 (2009).

[25] S. M. Sze & K. K. Ng, *Physics of Semiconductor Devices*. John Wiley & Sons, Inc. (2006)

[26] D. A. Neamen, *Semiconductor Physics and Devices: Basic Principles*. McGraw-Hill (2003)

[27] R. Scheer & H.-W. Schock, *Chalcogenide Photovoltaics: Physics, Technologies, and Thin Film Devices*. Wiley-VCH Verlag GmbH & Co. KGaA (2011)

[28] W. Shockley & H. J. Queisser, Detailed Balance Limit of Efficiency of P-N Junction Solar Cells. *Journal of Applied Physics*, **32,** 510–519 (1961).

[29] National Renewable Energy Laboratory, *Best Research-Cell Efficiencies*. at http://www.nrel.gov/ncpv/images/efficiency_chart.jpg

[30] M. Graetzel, R. A. J. Janssen, D. B. Mitzi & E. H. Sargent, Materials Interface Engineering for Solution-Processed Photovoltaics. *Nature*, **488,** 304–12 (2012).

[31] E. H. Sargent, Colloidal Quantum Dot Solar Cells. *Nature Photonics*, **6,** 133–135 (2012).

[32] J. M. Luther, J. Gao, M. T. Lloyd, O. E. Semonin, M. C. Beard & A. J. Nozik, Stability Assessment on a 3% Bilayer PbS/ZnO Quantum Dot

Heterojunction Solar Cell. *Advanced Materials*, **22,** 3704–3707 (2010).

[33] J. Tang, K. W. Kemp, S. Hoogland, K. S. Jeong, H. Liu, L. Levina, M. Furukawa, X. Wang, R. Debnath, D. Cha, K. W. Chou, A. Fischer, A. Amassian, J. B. Asbury & E. H. Sargent, Colloidal-Quantum-Dot Photovoltaics Using Atomic-Ligand Passivation. *Nature Materials*, **10,** 765–771 (2011).

[34] A. H. Ip, S. M. Thon, S. Hoogland, O. Voznyy, D. Zhitomirsky, R. Debnath, L. Levina, L. R. Rollny, G. H. Carey, A. Fischer, K. W. Kemp, I. J. Kramer, Z. Ning, A. J. Labelle, K. W. Chou, A. Amassian & E. H. Sargent, Hybrid Passivated Colloidal Quantum Dot Solids. *Nature Nanotechnology*, **7,** 577–582 (2012).

[35] C.-H. M. Chuang, P. R. Brown, V. Bulović & M. G. Bawendi, Improved Performance and Stability in Quantum Dot Solar Cells through Band Alignment Engineering. *Nature Materials*, **13,** 796–801 (2014).

[36] J. Gao, C. L. Perkins, J. M. Luther, M. C. Hanna, H. Chen, O. E. Semonin, A. J. Nozik, R. J. Ellingson & M. C. Beard, N-Type Transition Metal Oxide as a Hole Extraction Layer in PbS Quantum Dot Solar Cells. *Nano Letters*, **11,** 3263–3266 (2011).

[37] M. A. Hines & G. D. Scholes, Colloidal PbS Nanocrystals with Size-Tunable near-Infrared Emission: Observation of Post-Synthesis Self-Narrowing of the Particle Size Distribution. *Advanced Materials*, **15,** 1844–1849 (2003).

[38] M. C. Weidman, M. E. Beck, R. S. Hoffman, F. Prins & W. A. Tisdale, Monodisperse, Air-Stable PbS Nanocrystals via Precursor Stoichiometry Control. *ACS Nano*, **8,** 6363–71 (2014).

[39] C. Wadia, A. P. Alivisatos & D. M. Kammen, Materials Availability Expands the Opportunity for Large-Scale Photovoltaics Deployment. *Environmental Science & Technology*, **43,** 2072–2077 (2009).

[40] J. Jean, P. R. Brown, R. L. Jaffe, T. Buonassisi & V. Bulović, Pathways for Solar Photovoltaics. *Energy & Environmental Science*, **8,** 1200–1219 (2015).

[41] A. Fischer, L. Rollny, J. Pan, G. H. Carey, S. M. Thon, S. Hoogland, O. Voznyy, D. Zhitomirsky, J. Y. Kim, O. M. Bakr & E. H. Sargent, Directly Deposited Quantum Dot Solids Using a Colloidally Stable Nanoparticle Ink. *Advanced Materials*, **25,** 5742–5749 (2013).

[42] Z. Ning, H. Dong, Q. Zhang, O. Voznyy & E. H. Sargent, Solar Cells Based on Inks of N-Type Colloidal Quantum Dots. *ACS Nano*, **8,** 10321–10327 (2014).

[43] J. J. Choi, J. Luria, B.-R. Hyun, A. C. Bartnik, L. Sun, Y.-F. Lim, J. a Marohn, F. W. Wise & T. Hanrath, Photogenerated Exciton Dissociation in Highly Coupled Lead Salt Nanocrystal Assemblies. *Nano Letters*, **10,** 1805–11 (2010).

[44] O. E. Semonin, J. M. Luther, S. Choi, H.-Y. Chen, J. Gao, A. J. Nozik & M. C. Beard, Peak External Photocurrent Quantum Efficiency Exceeding 100% via MEG in a Quantum Dot Solar Cell. *Science*, **334,** 1530–3 (2011).

[45] Y. Liu, M. Gibbs, J. Puthussery, S. Gaik, R. Ihly, H. W. Hillhouse & M. Law, Dependence of Carrier Mobility on Nanocrystal Size and Ligand Length in PbSe Nanocrystal Solids. *Nano Letters*, **10,** 1960–9 (2010).

[46] Y. Gao, M. Aerts, C. S. S. Sandeep, E. Talgorn, T. J. Savenije, S. Kinge, L. D. A. Siebbeles & A. J. Houtepen, Photoconductivity of PbSe Quantum-Dot Solids: Dependence on Ligand Anchor Group and Length. *ACS Nano*, **6,** 9606 (2012).

[47] P. R. Brown, D. Kim, R. R. Lunt, N. Zhao, M. G. Bawendi, J. C. Grossman & V. Bulović, Energy Level Modification in Lead Sulfide Quantum Dot Thin Films through Ligand Exchange. *ACS Nano*, **8,** 5863–72 (2014).

[48] J. M. Luther, M. Law, M. C. Beard, Q. Song, M. O. Reese, R. J. Ellingson & A. J. Nozik, Schottky Solar Cells Based on Colloidal Nanocrystal Films. *Nano Letters*, **8,** 3488–92 (2008).

[49] J. J. Choi, Y.-F. Lim, M. B. Santiago-Berrios, M. Oh, B.-R. Hyun, L. Sun, A. C. Bartnik, A. Goedhart, G. G. Malliaras, H. D. Abruña, F. W. Wise & T. Hanrath, PbSe Nanocrystal Excitonic Solar Cells. *Nano Letters*, **9,** 3749–55 (2009).

[50] P. R. Brown, R. R. Lunt, N. Zhao, T. P. Osedach, D. D. Wanger, L.-Y. Chang, M. G. Bawendi & V. Bulović, Improved Current Extraction from ZnO/PbS Quantum Dot Heterojunction Photovoltaics Using a MoO3 Interfacial Layer. *Nano Letters*, **11,** 2955–2961 (2011).

[51] A. G. Pattantyus-Abraham, I. J. Kramer, A. R. Barkhouse, X. Wang, G. Konstantatos, R. Debnath, L. Levina, I. Raabe, M. K. Nazeeruddin, M.

Grätzel & E. H. Sargent, Depleted-Heterojunction Colloidal Quantum Dot Solar Cells. *ACS Nano*, **4,** 3374–80 (2010).

[52] W. U. Huynh, J. J. Dittmer & A. P. Alivisatos, Hybrid Nanorod-Polymer Solar Cells. *Science*, **295,** 2425–7 (2002).

[53] I. Gur, N. A. Fromer, M. L. Geier & A. P. Alivisatos, Air-Stable All-Inorganic Nanocrystal Solar Cells Processed from Solution. *Science*, **310,** 462–5 (2005).

[54] K. W. Johnston, A. G. Pattantyus-Abraham, J. P. Clifford, S. H. Myrskog, D. D. MacNeil, L. Levina & E. H. Sargent, Schottky-Quantum Dot Photovoltaics for Efficient Infrared Power Conversion. *Applied Physics Letters*, **92,** 151115 (2008).

[55] E. J. D. Klem, D. D. MacNeil, P. W. Cyr, L. Levina & E. H. Sargent, Efficient Solution-Processed Infrared Photovoltaic Cells: Planarized All-Inorganic Bulk Heterojunction Devices via Inter-Quantum-Dot Bridging during Growth from Solution. *Applied Physics Letters*, **90,** 183113 (2007).

[56] E. Talgorn, Y. Gao, M. Aerts, L. T. Kunneman, J. M. Schins, T. J. Savenije, M. a van Huis, H. S. J. van der Zant, A. J. Houtepen & L. D. a Siebbeles, Unity Quantum Yield of Photogenerated Charges and Band-like Transport in Quantum-Dot Solids. *Nature Nanotechnology*, **6,** 733–9 (2011).

[57] L.-Y. Chang, R. R. Lunt, P. R. Brown, V. Bulović & M. G. Bawendi, Low-Temperature Solution-Processed Solar Cells Based on PbS Colloidal Quantum dot/CdS Heterojunctions. *Nano Letters*, **13,** 994–9 (2013).

[58] N. Zhao, T. P. Osedach, L.-Y. Chang, S. M. Geyer, D. Wanger, M. T. Binda, A. C. Arango, M. G. Bawendi & V. Bulovic, Colloidal PbS Quantum Dot Solar Cells with High Fill Factor. *ACS Nano*, **4,** 3743–52 (2010).

[59] J. Gao, J. M. Luther, O. E. Semonin, R. J. Ellingson, A. J. Nozik & M. C. Beard, Quantum Dot Size Dependent J-V Characteristics in Heterojunction ZnO/PbS Quantum Dot Solar Cells. *Nano Letters*, **11,** 1002–8 (2011).

[60] J. J. Choi, W. N. Wenger, R. S. Hoffman, Y.-F. Lim, J. Luria, J. Jasieniak, J. a Marohn & T. Hanrath, Solution-Processed Nanocrystal Quantum Dot Tandem Solar Cells. *Advanced Materials*, **23,** 3144–3148 (2011).

[61] X. Wang, G. I. Koleilat, J. Tang, H. Liu, I. J. Kramer, R. Debnath, L. Brzozowski, D. A. R. Barkhouse, L. Levina, S. Hoogland & E. H. Sargent,

Tandem Colloidal Quantum Dot Solar Cells Employing a Graded Recombination Layer. *Nature Photonics*, **5,** 480–484 (2011).

[62] R. Schaller & V. Klimov, High Efficiency Carrier Multiplication in PbSe Nanocrystals: Implications for Solar Energy Conversion. *Physical Review Letters*, **92,** 1–4 (2004).

[63] G. Nair, L.-Y. Chang, S. M. Geyer & M. G. Bawendi, Perspective on the Prospects of a Carrier Multiplication Nanocrystal Solar Cell. *Nano Letters*, **11,** 2145–51 (2011).

[64] D. Zhitomirsky, O. Voznyy, S. Hoogland & E. H. Sargent, Measuring Charge Carrier Diffusion in Coupled Colloidal Quantum Dot Solids. *ACS Nano*, **7,** 5282–90 (2013).

[65] J. Tang, H. Liu, D. Zhitomirsky, S. Hoogland, X. Wang, M. Furukawa, L. Levina & E. H. Sargent, Quantum Junction Solar Cells. *Nano Letters*, **12,** 4889–94 (2012).

[66] A. K. Rath, M. Bernechea, L. Martinez, F. P. G. de Arquer, J. Osmond & G. Konstantatos, Solution-Processed Inorganic Bulk Nano-Heterojunctions and Their Application to Solar Cells. *Nature Photonics*, **6,** 529–534 (2012).

[67] Z. Ning, D. Zhitomirsky, V. Adinolfi, B. Sutherland, J. Xu, O. Voznyy, P. Maraghechi, X. Lan, S. Hoogland, Y. Ren & E. H. Sargent, Graded Doping for Enhanced Colloidal Quantum Dot Photovoltaics. *Advanced Materials*, **25,** 1719–23 (2013).

[68] M. Yuan, D. Zhitomirsky, V. Adinolfi, O. Voznyy, K. W. Kemp, Z. Ning, X. Lan, J. Xu, J. Y. Kim, H. Dong & E. H. Sargent, Doping Control via Molecularly Engineered Surface Ligand Coordination. *Advanced Materials*, **25,** 5586–92 (2013).

[69] J. Jean, S. Chang, P. R. Brown, J. J. Cheng, P. H. Rekemeyer, M. G. Bawendi, S. Gradečak & V. Bulović, ZnO Nanowire Arrays for Enhanced Photocurrent in PbS Quantum Dot Solar Cells. *Advanced Materials*, **25,** 2790–2796 (2013).

[70] M. Soreni-Harari, N. Yaacobi-Gross, D. Steiner, A. Aharoni, U. Banin, O. Millo & N. Tessler, Tuning Energetic Levels in Nanocrystal Quantum Dots through Surface Manipulations. *Nano Letters*, **8,** 678–84 (2008).

[71] J. Jasieniak, M. Califano & S. E. Watkins, Size-Dependent Valence and

Conduction Band-Edge Energies of Semiconductor Nanocrystals. *ACS Nano*, **5,** 5888–902 (2011).

[72] P. R. Brown, D. Kim, R. R. Lunt, N. Zhao, M. G. Bawendi, J. C. Grossman & V. Bulović, Level Modification. *ACS Nano*, **8,** 5863–72 (2014).

[73] V. Shrotriya, G. Li, Y. Yao, C.-W. Chu & Y. Yang, Transition Metal Oxides as the Buffer Layer for Polymer Photovoltaic Cells. *Applied Physics Letters*, **88,** 073508 (2006).

[74] J. Meyer, S. Hamwi, M. Kröger, W. Kowalsky, T. Riedl & A. Kahn, Transition Metal Oxides for Organic Electronics: Energetics, Device Physics and Applications. *Advanced Materials*, **24,** 5408–5427 (2012).

[75] M. T. Greiner, M. G. Helander, W. Tang, Z. Wang, J. Qiu & Z. Lu, Universal Energy-Level Alignment of Molecules on Metal Oxides. *Nature Materials*, **11,** 76–81 (2012).

[76] J. Meyer, A. Shu, M. Kröger & A. Kahn, Effect of Contamination on the Electronic Structure and Hole-Injection Properties of MoO3/organic Semiconductor Interfaces. *Applied Physics Letters*, **96,** 133308 (2010).

[77] H. Ding, Y. Gao, C. Small, D. Y. Kim, J. Subbiah & F. So, Energy Level Evolution of Air and Oxygen Exposed Molybdenum Trioxide Films. *Applied Physics Letters*, **96,** 243307 (2010).

[78] W. J. E. Beek, M. M. Wienk, M. Kemerink, X. Yang & R. A. J. Janssen, Hybrid Zinc Oxide Conjugated Polymer Bulk Heterojunction Solar Cells. *The Journal of Physical Chemistry. B*, **109,** 9505–16 (2005).

[79] L. A. A. Pettersson, L. S. Roman, O. Ingana & I. Introduction, Modeling Photocurrent Action Spectra of Photovoltaic Devices Based on Organic Thin Films. **86,** 487–496 (1999).

[80] G. F. Burkhard, E. T. Hoke & M. D. McGehee, Accounting for Interference, Scattering, and Electrode Absorption to Make Accurate Internal Quantum Efficiency Measurements in Organic and Other Thin Solar Cells. *Advanced Materials*, **22,** 3293–3297 (2010).

[81] C.-H. M. Chuang, A. Maurano, R. E. Brandt, G. W. Hwang, J. Jean, T. Buonassisi, V. Bulović & M. G. Bawendi, Open-Circuit Voltage Deficit, Radiative Sub-Bandgap States, and Prospects in Quantum Dot Solar Cells. *Nano Letters*, **15,** 3286–3294 (2015).

[82] G. W. Hwang, D. Kim, J. M. Cordero, M. W. B. Wilson, C.-H. M. Chuang, J. C. Grossman & M. G. Bawendi, Identifying and Eliminating Emissive Sub-Bandgap States in Thin Films of PbS Nanocrystals. *Advanced Materials*, **27,** 4481–4486 (2015).

[83] T. Schmidt, K. Lischka & W. Zulehner, Excitation-Power Dependence of the near-Band-Edge Photoluminescence of Semiconductors. *Physical Review B*, **45,** 8989–8994 (1992).

[84] J. Gao, J. Zhang, J. van de Lagemaat, J. C. Johnson & M. C. Beard, Charge Generation in PbS Quantum Dot Solar Cells Characterized by Temperature-Dependent Steady-State Photoluminescence. *ACS Nano*, **8,** 12814–12825 (2014).

[85] P. Nagpal & V. I. Klimov, Role of Mid-Gap States in Charge Transport and Photoconductivity in Semiconductor Nanocrystal Films. *Nature Communications*, **2,** 486 (2011).

[86] D. Bozyigit, S. Volk, O. Yarema & V. Wood, Quantification of Deep Traps in Nanocrystal Solids, Their Electronic Properties, and Their Influence on Device Behavior. *Nano Letters*, **13,** 5284–8 (2013).

[87] G. H. Carey, I. J. Kramer, P. Kanjanaboos, G. Moreno-Bautista, O. Voznyy, L. Rollny, J. A. Tang, S. Hoogland & E. H. Sargent, Electronically Active Impurities in Colloidal Quantum Dot Solids. *ACS Nano*, **8,** 11763–11769 (2014).

[88] Y. Zhang, D. Zherebetskyy, N. D. Bronstein, S. Barja, L. Lichtenstein, D. Schuppisser, L.-W. Wang, a. P. Alivisatos & M. Salmeron, Charge Percolation Pathways Guided by Defects in Quantum Dot Solids. *Nano Letters*, **15,** 3249–3253 (2015).

[89] D. Kim, D.-H. Kim, J.-H. Lee & J. C. Grossman, Impact of Stoichiometry on the Electronic Structure of PbS Quantum Dots. *Physical Review Letters*, **110,** 196802 (2013).

[90] O. Voznyy, D. Zhitomirsky, P. Stadler, Z. Ning, S. Hoogland & E. H. Sargent, A Charge-Orbital Balance Picture of Doping in Colloidal Quantum Dot Solids. *ACS Nano*, **6,** 8448–55 (2012).

[91] A. Loiudice, A. Rizzo, G. Grancini, M. Biasiucci, M. R. Belviso, M. Corricelli, M. L. Curri, M. Striccoli, A. Agostiano, P. D. Cozzoli, A. Petrozza, G.

Lanzani & G. Gigli, Fabrication of Flexible All-Inorganic Nanocrystal Solar Cells by Room-Temperature Processing. *Energy & Environmental Science*, **6,** 1565–1572 (2013).

[92] H. Wang, T. Kubo, J. Nakazaki & H. Segawa, PbS Colloidal Quantum dot/ZnO-Based Bulk-Heterojunction Solar Cells with High Stability under Continuous Light Soaking. *Physica Status Solidi - Rapid Research Letters*, **8,** 961–965 (2014).

[93] W. K. Bae, J. Joo, L. A. Padilha, J. Won, D. C. Lee, Q. Lin, W. Koh, H. Luo, V. I. Klimov & J. M. Pietryga, Highly Effective Surface Passivation of PbSe Quantum Dots through Reaction with Molecular Chlorine. *Journal of the American Chemical Society*, **134,** 20160–8 (2012).

[94] J. Zhang, J. Gao, C. P. Church, E. M. Miller, J. M. Luther, V. I. Klimov & M. C. Beard, PbSe Quantum Dot Solar Cells with More than 6% Efficiency Fabricated in Ambient Atmosphere. *Nano Letters*, **14,** 6010–5 (2014).

[95] J. Zhang, J. Gao, E. M. Miller, J. M. Luther & M. C. Beard, Diffusion-Controlled Synthesis of PbS and PbSe Quantum Dots with in Situ Halide Passivation for Quantum Dot Solar Cells. *ACS Nano*, **8,** 614–22 (2014).

[96] J. Y. Woo, J.-H. Ko, J. H. Song, K. Kim, H. Choi, Y.-H. Kim, D. C. Lee & S. Jeong, Ultrastable PbSe Nanocrystal Quantum Dots via in Situ Formation of Atomically Thin Halide Adlayers on PbSe(100). *Journal of the American Chemical Society*, **136,** 8883–6 (2014).

[97] H. Wang, T. Kubo, J. Nakazaki, T. Kinoshita & H. Segawa, PbS-Quantum-Dot-Based Heterojunction Solar Cells Utilizing ZnO Nanowires for High External Quantum Efficiency in the Near-Infrared Region. *The Journal of Physical Chemistry Letters*, **4,** 2455–2460 (2013).

[98] M. A. Green, K. Emery, Y. Hishikawa, W. Warta & E. D. Dunlop, Solar Cell Efficiency Tables (version 44). *Progress in Photovoltaics*, **22,** 701–710 (2014).

[99] P. Guyot-Sionnest, Electrical Transport in Colloidal Quantum Dot Films. *The Journal of Physical Chemistry Letters*, **3,** 1169–1175 (2012).

[100] S. De Wolf, J. Holovsky, S.-J. Moon, P. Löper, B. Niesen, M. Ledinsky, F.-J. Haug, J.-H. Yum & C. Ballif, Organometallic Halide Perovskites: Sharp Optical Absorption Edge and Its Relation to Photovoltaic Performance. *The*

Journal of Physical Chemistry Letters, **5,** 1035–1039 (2014).

[101] P. T. Erslev, H. Chen, J. Gao, M. C. Beard, A. J. Frank, J. van de Lagemaat, J. C. Johnson & J. M. Luther, Sharp Exponential Band Tails in Highly Disordered Lead Sulfide Quantum Dot Arrays. *Physical Review B*, **86,** 155313 (2012).

[102] D. Zhitomirsky, I. J. Kramer, A. J. Labelle, A. Fischer, R. Debnath, J. Pan, O. M. Bakr & E. H. Sargent, Colloidal Quantum Dot Photovoltaics: The Effect of Polydispersity. *Nano Letters*, **12,** 1007–12 (2012).

[103] K. W. Kemp, A. J. Labelle, S. M. Thon, A. H. Ip, I. J. Kramer, S. Hoogland & E. H. Sargent, Interface Recombination in Depleted Heterojunction Photovoltaics Based on Colloidal Quantum Dots. *Advanced Energy Materials*, **3,** 917–922 (2013).

[104] V. Nadenau, U. Rau, A. Jasenek & H. W. Schock, Electronic Properties of CuGaSe2-Based Heterojunction Solar Cells. Part I. Transport Analysis. *Journal of Applied Physics*, **87,** 584–593 (2000).

[105] H. Liu, J. Tang, I. J. Kramer, R. Debnath, G. I. Koleilat, X. Wang, A. Fisher, R. Li, L. Brzozowski, L. Levina & E. H. Sargent, Electron Acceptor Materials Engineering in Colloidal Quantum Dot Solar Cells. *Advanced Materials*, **23,** 3832–7 (2011).

[106] B. Ehrler, K. P. Musselman, M. L. Böhm, F. S. F. Morgenstern, Y. Vaynzof, B. J. Walker, J. L. Macmanus-Driscoll & N. C. Greenham, Preventing Interfacial Recombination in Colloidal Quantum Dot Solar Cells by Doping the Metal Oxide. *ACS Nano*, **7,** 4210–20 (2013).

[107] R. L. Z. Hoye, B. Ehrler, M. L. Böhm, D. Muñoz-Rojas, R. M. Altamimi, A. Y. Alyamani, Y. Vaynzof, A. Sadhanala, G. Ercolano, N. C. Greenham, R. H. Friend, J. L. MacManus-Driscoll & K. P. Musselman, Improved Open-Circuit Voltage in ZnO-PbSe Quantum Dot Solar Cells by Understanding and Reducing Losses Arising from the ZnO Conduction Band Tail. *Advanced Energy Materials*, **4,** 1301544 (2014).

[108] A. Franciosi & C. G. Van de Walle, Heterojunction Band Offset Engineering. *Surface Science Reports*, **25,** 1–140 (1996).

[109] D. Bozyigit, W. M. M. Lin, N. Yazdani, O. Yarema & V. Wood, A Quantitative Model for Charge Carrier Transport, Trapping and

Recombination in Nanocrystal-Based Solar Cells. *Nature Communications*, **6,** 6180 (2015).

[110] A. K. Rath, F. Pelayo Garcia De Arquer, A. Stavrinadis, T. Lasanta, M. Bernechea, S. L. Diedenhofen & G. Konstantatos, Remote Trap Passivation in Colloidal Quantum Dot Bulk Nano-Heterojunctions and Its Effect in Solution-Processed Solar Cells. *Advanced Materials*, **26,** 4741–4747 (2014).

[111] W. Yoon, J. E. Boercker, M. P. Lumb, D. Placencia, E. E. Foos & J. G. Tischler, Enhanced Open-Circuit Voltage of PbS Nanocrystal Quantum Dot Solar Cells. *Scientific Reports*, **3,** 2225 (2013).

[112] D. D. Wanger, R. E. Correa, E. a Dauler & M. G. Bawendi, The Dominant Role of Exciton Quenching in PbS Quantum-Dot-Based Photovoltaic Devices. *Nano Letters*, **13,** 5907–5912 (2013).

[113] D. Zhitomirsky, O. Voznyy, L. Levina, S. Hoogland, K. W. Kemp, A. H. Ip, S. M. Thon & E. H. Sargent, Engineering Colloidal Quantum Dot Solids within and beyond the Mobility-Invariant Regime. *Nature Communications*, **5,** 3803 (2014).

[114] I. J. Kramer, D. Zhitomirsky, J. D. Bass, P. M. Rice, T. Topuria, L. Krupp, S. M. Thon, A. H. Ip, R. Debnath, H.-C. Kim & E. H. Sargent, Ordered Nanopillar Structured Electrodes for Depleted Bulk Heterojunction Colloidal Quantum Dot Solar Cells. *Advanced Materials*, **24,** 2315–2319 (2012).

[115] S. J. Oh, N. E. Berry, J.-H. Choi, E. A. Gaulding, T. Paik, S.-H. Hong, C. B. Murray & C. R. Kagan, Stoichiometric Control of Lead Chalcogenide Nanocrystal Solids to Enhance Their Electronic and Optoelectronic Device Performance. *ACS Nano*, **7,** 2413–21 (2013).

[116] D. N. Dirin, S. Dreyfuss, M. I. Bodnarchuk, G. Nedelcu, P. Papagiorgis, G. Itskos & M. V Kovalenko, Lead Halide Perovskites and Other Metal Halide Complexes as Inorganic Capping Ligands for Colloidal Nanocrystals. *Journal of the American Chemical Society*, **136,** 6550–3 (2014).

[117] H. Zhang, J. Jang, W. Liu & D. V Talapin, Colloidal Nanocrystals with Inorganic Halide, Pseudohalide, and Halometallate Ligands. *ACS Nano*, **8,** 7359–69 (2014).

[118] D. Bozyigit & V. Wood, Electrical Characterization of Nanocrystal Solids. *Journal of Materials Chemistry C*, **2,** 3172–84 (2014).

[119] S. J. Oh, Z. Wang, N. E. Berry, J. Choi, T. Zhao, E. A. Gaulding, T. Paik, Y. Lai, C. B. Murray & C. R. Kagan, Engineering Charge Injection and Charge Transport for High Performance PbSe Nanocrystal Thin Film Devices and Circuits. *Nano Letters*, **14,** 6210–16 (2014).

[120] E. Zimmermann, P. Ehrenreich, T. Pfadler, J. A. Dorman, J. Weickert & L. Schmidt-Mende, Erroneous Efficiency Reports Harm Organic Solar Cell Research. *Nature Photonics*, **8,** 669–672 (2014).

[121] J. Gao, S. Jeong, F. Lin, P. T. Erslev, O. E. Semonin, J. M. Luther & M. C. Beard, Improvement in Carrier Transport Properties by Mild Thermal Annealing of PbS Quantum Dot Solar Cells. *Applied Physics Letters*, **102,** 043506 (2013).

[122] R. W. Crisp, D. M. Kroupa, A. R. Marshall, E. M. Miller, J. Zhang, M. C. Beard & J. M. Luther, Metal Halide Solid-State Surface Treatment for High Efficiency PbS and PbSe QD Solar Cells. *Scientific Reports*, **5,** 9945 (2015).

[123] A. R. Marshall, M. R. Young, A. J. Nozik, M. C. Beard & J. M. Luther, Exploration of Metal Chloride Uptake for Improved Performance Characteristics of PbSe Quantum Dot Solar Cells. *The Journal of Physical Chemistry Letters*, **6,** 2892–2899 (2015).

[124] D.-K. Ko, A. Maurano, S. K. Suh, D. Kim, G. W. Hwang, J. C. Grossman, V. Bulović & M. G. Bawendi, Photovoltaic Performance of PbS Quantum Dots Treated with Metal Salts. *ACS Nano*, **10,** 3382–3388 (2016).

[125] J. You, C.-C. Chen, Z. Hong, K. Yoshimura, K. Ohya, R. Xu, S. Ye, J. Gao, G. Li & Y. Yang, 10.2% Power Conversion Efficiency Polymer Tandem Solar Cells Consisting of Two Identical Sub-Cells. *Advanced Materials*, **25,** 3973–3978 (2013).